

---

RELATIVISTIC OUTFLOWS FROM  
ACTIVE GALACTIC NUCLEI (AGN)  
AND THEIR CONNECTION TO  
ACCRETION DISKS

---

*A thesis*

*Submitted in partial fulfillment of the requirements*

*Of the degree of*

*Doctor of Philosophy*

By

**Shende Mayur Bhaskar**

20142030



**INDIAN INSTITUTE OF SCIENCE EDUCATION AND  
RESEARCH (IISER) PUNE**

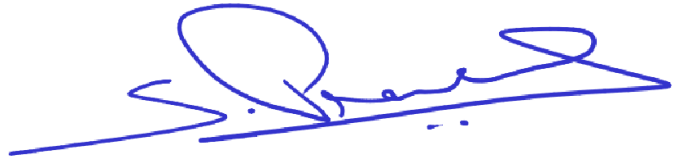
*where tomorrow's science begins today*



# Certificate

Certified that the work incorporated in the thesis entitled '*Relativistic Outflows from Active Galactic Nuclei (AGN) and their connection to Accretion Disks*', submitted by *Shende Mayur Bhaskar* was carried out by the candidate, under my supervision. The work presented here or any part of it has not been included in any other thesis submitted previously for the award of any degree or diploma from any other University or institution.

*Date* Sept 27, 2022



**Prof. Prasad Subramanian**



# Declaration

I declare that this written submission represents my ideas in my own words and where others' ideas have been included, I have adequately cited and referenced the original sources. I also declare that I have adhered to all principles of academic honesty and integrity and have not misrepresented or fabricated or falsified any idea/data/fact/source in my submission. I understand that violation of the above will be cause for disciplinary action by the Institute and can also evoke penal action from the sources which have thus not been properly cited or from whom proper permission has not been taken when needed.

*Date* Sept 27, 2022



**Shende Mayur Bhaskar**

Roll No - 20142030



**To Aai, Pappa & Anju**





# Acknowledgements

As this beautiful journey of PhD is coming to an end, I would like to express my gratitude to all those people who were integral part of this journey and helped me shape the kind of person I am today, both academically and personally.

First of all, I would like to express my heartfelt gratitude towards my PhD advisor, Prof. Prasad Subramanian, for his constant support and encouragement throughout my PhD. This thesis wouldn't have been possible without his valuable guidance and insights. I am thankful to our numerous discussions about science, and also about other things in life. Apart from being a very good physicist, he is also an incredible human being. Under his guidance, I could work with freedom and without pressure. He always supported me whenever I was struggling with work, or in personal life, and kept motivating me. I can't thank him enough for the role he played during this journey.

I am thankful to Dr. T. S. Mahesh, Dr. Sourabh Dube, and Dr. Arun Thalapillil (the members of my Research Advisory Committee) for their valuable suggestions which helped me improve my research significantly.

I will always be thankful to IISER Pune for providing me PhD fellowship during my regular tenure and also during the testing times of the pandemic. I am thankful for the excellent research facilities and infrastructure provided by IISER. I thank Tushar and Sayalee from the academic staff, as well as Prabhakar and Dhanashree from the Physics department staff for their continuous efforts which made our lives easier and we could work efficiently. I also thank IISER administration, library, security and housekeeping staff for their services. A special thanks to IISER for providing high quality sports facilities which helped me relieve stress to keep work-life balance. I will cherish those cricket and badminton matches forever.

I have had a chance to share many memories with some amazing members in our astrophysics group. I thank Nishtha and Tomin with whom I shared my office for a significant amount of my time during PhD. It was a fun journey with you guys. I thank Nishtha for teaching me some aspects of solar physics during our collaboration for my first paper. I thank Tomin for always keeping the office atmosphere joyful. I thank Debesh for the discussions related to academia and art.

Now comes the important part of this adventure. I have had a privilege of having

---

some great friends during this journey. Acknowledging them will take some time, but they are worth it. I will start by thanking Saurabh for his incredible support throughout my PhD. Saurabh, you are like an elder brother to me who always takes care of me. Our friendship has seen some ups and downs, but in the last two to three years, it has flourished beautifully. I will miss those late night discussions on every aspect of life. The thing I admire the most about you is, after all the hardships you have gone through in your life, you have faced them bravely and carried yourself joyfully. I am writing this acknowledgement about you sitting at your home seeing you packing for your postdoc journey starting from tomorrow. All the best for your future endeavours, brother!

I am thankful to Deepak Kumar and Yashaswi for the fun friendship we have. Being neighbours and having similar kinds of likes and dislikes when it comes to do fun activities, has led to amazing bonding between us. I still find it amusing the way we greet each other by saying “Ka karro hai?”, and then continue the conversation by pulling each other’s legs. I will miss those fun discussions we used to have, standing in front of our hostel rooms, and also the pranks we used to pull on each other.

I am thankful to Shalini for her absolute involvement when it comes to friendship. It took me some time to understand her nature, but now we are good friends. Shalini, thank you for preparing delicious food and then serving me by scolding every time. I will always cherish the bakaiti we used to do and numerous meals we used to have listening to Qawwalis of Nusrat sahab.

I am thankful to Saurabh’s family for their support. Because of them, I always felt that I have a family here in Pune. I am thankful to Uncle for his support and love and treating me like his own son. I thank Alka di and Richa for the amazing memories.

I am thankful to Priyanka for her support. I have learnt a lot from her as a person.

Now what do I tell you about Deepak, whom I lovingly call by the name Chhamiya. He is like a younger brother to me although he considers himself my elder brother, because he is full of nakhre. We became very good friends in our days of course work itself. Now we have become more like brothers. Deepak, thank you for taking care of me and being a steady support throughout this journey, especially in difficult times.

I am thankful to Tejal Agggaaaaarrrrwaaaallll, my chess partner, my badminton parner, and a really nice friend. Tejal, teaming up against the random opponents in online chess matches was hell of a fun time I spent with you. I guess I annoyed you the most, but still you used to bear with me; thank you very much for that.

I am thankful to Yashwant, a techie in our group for his amazing company.

---

Describing the real-life situations with memes, especially from the movie Hera Pheri, used to be a lot of fun with you, Yashwant. I am thankful to Sumit for those wonderful badminton matches we have played and our random singing sessions. I still laugh very hard thinking about the farewell gift you gave me, a key holder engraved with the image of Sardar Khan screaming “Chaabhi kahan hai?”. I am thankful to Sayali for our friendship. She is the most disciplined and intelligent person in our batch.

I am thankful to Ankita for the beautiful friendship we have developed over the past one and half years. You are gem of a person. Thank you for being so patient and understanding. Be it our long walks in NCL discussing about life and philosophy, be it the enormous amount of time we spent on the cricket ground, be it the time we spent playing with Happy, Rosie, and Shiny, or be it our group picnics to Pawna and Matheran, I will cherish those awesome memories.

I am thankful to Sudhir Sir for our interaction in Physics lab courses, and the time we spent on the badminton court. I am thankful to Mohit, Prashant, Kriti, Nilam, and Puneeta for their amazing company and fun time together.

One thing that was common with most of them was that on many occasions, they were the victims of my mischievous behaviour and pranks. I am thankful to all of them for bearing it and still wanting to be a part of my life. It was an incredible journey with such amazing people.

I am thankful to Sagar, my best friend, and a brother from another mother, for being the pillar of constant support throughout my life from the school days. I am thankful to Pranav for being there with me through my thicks and thins. I am also thankful to his family for their support and love.

I am thankful to my favourite school teachers, Bhalekar madam, Shende Sir, Uike madam and Manik madam for their love and blessings. I am thankful to Mahajan Sir from VIT Pune for always encouraging me to pursue physics, which played a huge role in me switching from engineering to physics.

Finally, I thank my parents and my sister Anjali for their unconditional love and support, and always believing in my abilities.



# Abstract

Active galactic nuclei (AGN) are remarkable astrophysical objects characterized by enormous luminosities and large-scale collimated, relativistic outflows. Miniature versions in our galaxy are called galactic microquasars. The general consensus is that AGN and microquasars are powered by the accretion of matter onto the black hole they harbor at their centers. We attempt to interpret observations of such sources that reveal significant dips in the X-ray intensity, followed by ejections of superluminal blobs at radio frequencies. Since X-rays originate from the inner, hot accretion disk and radio emission from the relativistic jet, these observations suggest a “disk-jet connection”, which we explore in this thesis.

We address the issue of episodic blob ejection from the inner, hot accretion disk/corona by envisaging the plasmoids as pre-existing current carrying magnetic flux ropes that were initially anchored in the accretion disk-corona. The plasmoids are ejected outwards via MHD instability mechanism called the toroidal instability (TI). The TI, which was originally explored in the context of laboratory tokamak plasmas, has been very successful in explaining coronal mass ejections (CMEs) from the Sun. Our detailed model predictions compare favorably with a representative set of multi-epoch observations of radio emitting knots from the radio galaxy 3C 120 (Shende, Subramanian, and Sachdeva, 2019).

On the other hand, the dips in X-ray intensity can be attributed to the rapid collapse of the hot, inner parts of the accretion disk, which can occur over the radial infall time-scale of the inner disk. However, estimates of this time-scale are hindered by a lack of knowledge of the operative viscosity in the collisionless plasma comprising the inner disk. We address this issue by prescribing the microphysical viscosity in hot accretion disks, instead of parametrizing it in terms of Shakura-Sunyaev  $\alpha$  parameter. The viscosity is characterized using published estimates of diffusion coefficients of cosmic ray protons in turbulent magnetic fields. The estimates of Shakura-Sunyaev  $\alpha$  parameter arising from our viscosity prescription have a range 0.02 to 0.08. We build simplified disk models and estimate the inner disk collapse timescales for AGN 3C 120 and 3C 111, and the galactic microquasar GRS 1915+105. Our inner disk collapse time-scale estimates are in good agreement with those of the observed X-ray dips (Shende, Chauhan, and Subramanian, 2021). We

---

find that the collapse time-scale is most sensitive to the outer radius of the hot accretion disk.

We build upon the work of [Becker, Subramanian, and Kazanas \(2001\)](#) to investigate the origin of steady relativistic winds from advection-dominated hot accretion disks. We match the fluid description of self-similar inflow-outflow solutions of advection-dominated disks with the particle distribution function of protons due to second-order Fermi acceleration in the accretion disk. In this way, a concrete disk-wind connection is established, and the results show how the high energy tail of the proton distribution function is ejected outwards as a relativistic wind.

# Publications

1. **Mayur B. Shende, Prasad Subramanian, Nishtha Sachdeva:** Episodic jets from black hole accretion disks, *The Astrophysical Journal*, Volume 877, Issue 2, article id. 130, 7 pp., June 2019, DOI: [10.3847/1538-4357/ab1cb6](https://doi.org/10.3847/1538-4357/ab1cb6).
2. **Mayur B. Shende, Prashali Chauhan, Prasad Subramanian:** X-ray dips in AGNs and microquasars – collapse time-scales of inner accretion disc, *Monthly Notices of the Royal Astronomical Society*, Volume 501, Issue 3, pp.3741-3749, March 2021, DOI: [10.1093/mnras/staa3838](https://doi.org/10.1093/mnras/staa3838).

---



# Contents

<b>1</b>	<b>Introduction</b>	<b>1</b>
1.1	Active Galactic Nuclei (AGN)	1
1.1.1	Blazars	3
1.2	Relativistic AGN Jets	4
1.2.1	Jet launching mechanisms and their connection to accretion disks	4
1.2.2	Jet composition	6
1.3	Multi-wavelength Observations of 3C 120 and 3C 111	7
1.4	Launching of Episodic Jets	7
1.5	Viscous Infalling Timescales of Inner Accretion Disks	8
1.6	Particle-dominated Relativistic Winds	9
<b>2</b>	<b>Episodic Jets From Black Hole Accretion Disks</b>	<b>11</b>
2.1	Introduction	11
2.1.1	Relativistic jets	11
2.1.2	Discrete blobs	12
2.2	The Torus Instability Model	13
2.3	Results and Comparison With Observations	18
2.3.1	Velocity and acceleration profiles of a blob	18
2.3.2	Comparison with multi-epoch observations of 3C 120	19
2.3.3	Mass loss rate due to blob ejection	23
2.4	Summary and Conclusions	27
<b>3</b>	<b>X-ray Dips in AGNs And Microquasars – Collapse Time-scales of Inner Accretion Disk</b>	<b>29</b>
3.1	Introduction	29
3.2	Hybrid Viscosity in Hot Accretion Disks	30
3.2.1	Hybrid Viscosity using $D_{\perp}$ from Candia & Roulet	32
3.2.2	Solutions for disk model	33
3.2.3	Model Self-Consistency Conditions	35
3.3	Inner Disk Collapse Timescale and Connection With X-ray Timescales	36

---

3.4	Results . . . . .	37
3.4.1	Model parameters . . . . .	37
3.4.2	Sensitivity of $t_{\text{infall}}$ to model parameters . . . . .	38
3.5	Summary and Conclusions . . . . .	39
<b>4</b>	<b>Relativistic Particle-Dominated Winds From Advection-Dominated Accretion Flows</b>	<b>51</b>
4.1	Introduction . . . . .	51
4.1.1	Advection-dominated accretion flows and outflows . . . . .	51
4.1.2	Relativistic outflows in the framework of particle acceleration mechanisms in the hot accretion flow . . . . .	52
4.2	Model for relativistic outflows . . . . .	54
4.2.1	Second-order Fermi acceleration in accretion flows . . . . .	54
4.2.2	Particle distribution in the hot, inner accretion flow . . . . .	54
4.2.3	RADIOS model – the fluid description of inflow-outflow . . . . .	58
4.2.4	Making a connection between fluid description and particle description . . . . .	61
4.3	Results . . . . .	64
4.4	Discussion and conclusions . . . . .	65
<b>5</b>	<b>Summary and Future Work</b>	<b>75</b>
5.1	Summary . . . . .	75
5.2	Future Work . . . . .	76
5.2.1	Confinement of energetic electrons in a blob, and effect of blobs on large-scale jet structure . . . . .	76
5.2.2	Energy dissipation in winds, and alternate acceleration mechanisms . . . . .	77
5.2.3	Time-dependent disk model, and quasi-periodic oscillations (QPOs) . . . . .	78
<b>A</b>	<b>Two-Temperature Accretion Disk, Comptonized Model</b>	<b>79</b>
	<b>Bibliography</b>	<b>80</b>

# List of Figures

2.1	Plasmoid as a flux rope . . . . .	14
2.2	Velocity and acceleration profiles of a blob (upper panel: as functions of distance from the black hole, lower panel: as functions of time) for $M = 5.5 \times 10^7 M_\odot$ , $R_0/b_0 = 10$ , $R_0 = 5 R_g$ , $n = 4$ , $p = 0$ and $\beta_0 = 0.001$	19
2.3	Velocity profiles of a blob showing the asymptotic velocity attained by a blob $\beta_{\text{asympt}} = 0.985$ . . . . .	20
2.4	Acceleration profiles of a blob with different linestyles given in the inset corresponding to the parameter varied . . . . .	21
2.5	Height-time profile of a representative plasmoid for different values of $V_{\text{Ah}}$ compared with observations of blob E8 . . . . .	23
3.1	Representative accretion disk models for (a) 3C 120 and (b) GRS 1915+105. This figure shows results for $10\alpha_{\text{hyb}}$ , $H/R$ , $10^{-12}T_i$ , $10^{-10}T_e$ and $10^{-10}N_i$ , with $\dot{M}/\dot{M}_E = 0.3$ , $\rho = 0.5$ and $\sigma^2 = 30$ . . . . .	42
3.2	Representative accretion disk models for (a) 3C 120 and (b) GRS 1915+105. This figure shows results for $10^{-3}\lambda_{ii}/H$ , $10\lambda/H$ and $10\lambda/R$ , with $\dot{M}/\dot{M}_E = 0.3$ , $\rho = 0.5$ and $\sigma^2 = 30$ . . . . .	43
3.3	This figure shows how the quantities $10\alpha_{\text{hyb}}$ , $10^{-1}H/R$ , $10^{-12}T_i$ , $10^{-10}T_e$ and $10^{-17}N_i$ (evaluated at $R = 15R_g$ ) vary with the black hole spin parameter $a_*$ . The black hole mass is taken to be representative of GRS 1915+105, the accretion rate is $\dot{M}/\dot{M}_E = 0.2$ and $\rho = 0.5$ , $\sigma^2 = 30$ . . . . .	44
3.4	Histograms of the X-ray dip durations observed in (a) 3C 120, and (b) 3C 111 . . . . .	45
3.5	(a) Parameter space corresponding to X-ray dip of 5 days in 3C 120, (b) Parameter space corresponding to X-ray dip of 120 days in 3C 120	46
3.6	(a) Parameter space corresponding to X-ray dip of 146 days in 3C 111, (b) Parameter space corresponding to X-ray dip of 402 days in 3C 111 . . . . .	47
3.7	(a) Parameter space corresponding to X-ray dip of 1 s in GRS 1915+105, (b) Parameter space corresponding to X-ray dip of 6 s in GRS 1915+105	48

3.8	(a) Parameter space corresponding to X-ray dip in the range 45–50 days in 3C 120, (b) Parameter space corresponding to X-ray dip in the range 290–330 days in 3C 111 . . . . .	49
3.9	A depiction of how $t_{\text{infall}}$ varies in response to changes in $\rho$ , $\sigma^2$ , and $R_{\text{out}}$ . . . . .	50
4.1	Schematic representation of proton distribution function in a hot, advective disk . . . . .	53
4.2	The $(\Omega_0 - \epsilon)$ parameter space of RADIOS (BSK01) (shaded closed area between three curves) . . . . .	66
4.3	$\zeta_c$ as a function of radius ( $r = R/R_g$ ) in the equatorial plane . . . . .	68
4.4	Schematic representation of proton distribution function in a hot, advective disk . . . . .	68
4.5	Profiles of (a) wind Bernoulli parameter $b(r)$ (in units of $c^2$ ), and (b) asymptotic Lorentz factor ( $\Gamma_\infty$ ), as functions of cylindrical radius . . . . .	69
4.6	Profiles of (a) number density, and (b) energy density of proton population escaping into the wind as a function of cylindrical radius . . . . .	70
4.7	(a) Profile of wind mass loss rate $d\dot{m}/dR$ in units of $4\pi m_p v_{\text{rms}} R_g D_c N_0$ , and (b) Superimposing the plots of $\Gamma_\infty$ (fig. 4.5b), and $d\dot{m}/dR$ (with same units as that of fig. 4.7a). The color codes of both solid, and dashed lines are shown in the box . . . . .	71
4.8	Profiles of (a) $\zeta_c$ , (b) wind Bernoulli parameter $b(r)$ (in units of $c^2$ ), (c) asymptotic Lorentz factor ( $\Gamma_\infty$ ) for the wind, (d) number density of escaping proton population, (e) energy density of escaping proton population, (f) wind mass loss rate $d\dot{m}/dR$ , as functions of radius ( $r = R/R_g$ ) in the equatorial plane. These are plotted with $\Omega_0 = 0.5$ , and for different values of $\epsilon$ . . . . .	72
4.9	Profiles of (a) $\zeta_c$ , (b) wind Bernoulli parameter $b(r)$ (in units of $c^2$ ), (c) asymptotic Lorentz factor ( $\Gamma_\infty$ ) for the wind, (d) number density of escaping proton population, (e) energy density of escaping proton population, (f) wind mass loss rate $d\dot{m}/dR$ , as functions of radius ( $r = R/R_g$ ) in the equatorial plane. These are plotted with $\epsilon = 0.1$ , and for different values of $\Omega_0$ . . . . .	73

# List of Tables

2.1	An analysis of how the asymptotic $\beta_{app}$ for blob E8 changes with model parameters . . . . .	24
3.1	Sensitivity analysis of parameters: fiducial model for 3C 120 . . . . .	39



# Chapter 1

## Introduction

Active galactic nuclei (AGN) are fascinating astrophysical objects, emitting enormous amounts of radiative energy at wavelengths ranging from radio waves all the way up to X-rays and gamma rays, together with powerful relativistic outflows collimated over large distances. These sources have been a subject of investigation from the past 50 years (both by way of observations, and theoretical exploration), and still fascinates the astrophysics community. It is now widely accepted that the energy output is a result of the accretion of matter onto a supermassive black hole at the center of the nucleus. It is believed that every galaxy harbors a supermassive black hole ( $\sim 10^6 - 10^{10} M_{\odot}$ ) at its center. It attracts surrounding matter (if it happens to be present in black hole's vicinity) and causes to fall onto it (accrete) in the form of a disk, called an accretion disk, by losing its angular momentum and spiralling inwards.

This thesis deals with the possible connection between the accretion disk and the emanating jet in AGN, and some galactic black hole sources (galactic microquasars). Before going into details of the “disk-jet connection”, we give here a brief review of the general characteristics of AGN, and AGN jets. We draw upon reviews by [Blandford et al. \(1990\)](#), [Peterson \(1997\)](#), [Netzer \(2015\)](#), [Padovani et al. \(2017\)](#), and Chapter 7 of [Frank, King, and Raine \(2002\)](#).

### 1.1 Active Galactic Nuclei (AGN)

Active galactic nuclei (AGN) can be defined from the observational point of view as apparently stellar sources, but with non-thermal energy spectra, and in some cases, significant redshifts. While we have a reasonably complete picture of stellar-mass objects, this is not the case with AGN. Some aspects of AGN are fairly well understood and some (including the energetics of the central engine) are not. AGN can be differentiated from the nucleus of a normal galaxy using the limit set by [Netzer \(2015\)](#) on the luminosity of AGN:  $L_{\text{AGN}}/L_{\text{Edd}} > 10^{-5}$ , where  $L_{\text{AGN}}$  is the bolometric

luminosity, and  $L_{\text{Edd}}$  is the Eddington luminosity ( $L_{\text{Edd}} = 4\pi GMcm_p/\sigma_T$ , where  $M$  is the mass of a central black hole, and  $c$ ,  $m_p$ , and  $\sigma_T$  are velocity of light, proton mass, and Thomson scattering cross section, respectively) given by  $L_{\text{Edd}} = 1.2 \times 10^{38} M/M_{\odot} \text{ erg s}^{-1}$ , where  $M_{\odot}$  is the solar mass.

AGN spectra are typically observed over a wide range of frequencies ranging from  $\lesssim 100$  MHz radio frequencies to  $\gtrsim 10^{22}$  Hz gamma-ray frequencies. This also involves a wide range of lengthscales ranging from the variable X-ray emission ( $\lesssim 10^{12}$  cm) corresponding to inner regions of an accretion flow, to giant double radio sources ( $\gtrsim 10^{25}$  cm) owing to the interaction of (kiloparsec to megaparsec scale) relativistic AGN jets with the extragalactic medium. Another interesting property of AGN is their prodigious luminous output, ranging from  $\sim 10^{33}$  erg  $\text{s}^{-1}$  (which is the radio luminosity of our galactic nucleus) up to  $\sim 10^{48}$  erg  $\text{s}^{-1}$  (UV power of most powerful quasars), making them more powerful non-explosive sources in the universe, which can therefore be detected at high cosmological redshifts. Also, the rapid variability (few hours to few days) in emission leads to the inference that the emitting regions are very small in most bands, implying high energy densities.

Broadly speaking, the following components are typically present in most AGN (Netzer, 2015; Padovani et al., 2017):

- Supermassive black hole ( $10^{-7}$ – $10^{-3}$  pc) at the center
- Accretion disk (subparsec scale) around the black hole, which is responsible for continuum emission
- High density (electron density  $n_e \gtrsim 10^8 \text{ cm}^{-3}$ ), dust free gas cloud at Keplerian velocities ( $\sim 0.01$ – $1$  pc), emitting broad emission lines (broad-line region–BLR)
- The central torus ( $\sim 1$ – $10$  pc), obscures the emission from the accretion disk, and the corona
- Low density ( $n_e \approx 10^3 - 10^6 \text{ cm}^{-3}$ ), low velocity gas outside the torus (hundreds to thousands of parsecs), emitting narrow emission lines (narrow-line region–NLR)
- Central jet ( $\sim 10^{-7} - 10^6$  pc)

Since AGN are observed at all spectral bands, the various wavelength regimes provide different windows on AGN physics. The infrared (IR) band is mostly sensitive to the obscuring dusty torus, whereas the optical/UV emission is thought to emanate from the accretion disk. The origin of the X-ray continuum emission is believed to be the inner, hot regions of the accretion disk/corona, while the radio and gamma-ray observations are due to the non-thermal emission from the jet and the lobes.



Such a rich phenomenology of AGN has led to the complex and confusing taxonomy of AGN, often called the AGN “zoo”. The classification of AGN depends only partially on the intrinsic differences between AGN, and are due to changes in only a small number of parameters, as well as the method by which each class of AGN is selected. We consider here the broad classification based on some of the main characteristics such as continuum emission, line spectra, polarization, and variability. AGN are broadly classified into Seyfert galaxies, quasars, and BL Lacs, based on these characteristics. Seyferts show non-stellar continuum, and strong emission lines in their optical spectra. They are further subclassified into Seyfert type 1 and type 2 based on the existence of broad emission lines, and narrow emission lines in their nuclei, respectively. Quasars were discovered during the first radio surveys of the sky in the late 1950s. They are star-like objects identified with radio sources at large redshifts, have time-variable continuum flux, large UV flux, and broad emission lines. There is another class of strong radio sources in which the underlying galactic type is discernible, and are called radio galaxies. BL Lacs show weak lines, if any, but manifest the other quasar properties (like the characteristic continua). They also show rapid and large-amplitude flux variability, and significant radio and optical polarization. Some quasars also exhibit these properties, and are known as optically violent variables (OVVs). There are also sources which show the overlap of these properties. A particular class of objects called *Blazars*, which are highly polarized quasars with strong emission lines and rapid variability (basically showing the properties of both BL Lacs, and OVVs), are of particular importance to us. We refer to the reviews given by [Hovatta and Lindfors \(2019\)](#), and [Costamante \(2020\)](#) to explain the properties of blazars.

### 1.1.1 Blazars

About 10% of the observed AGN harbor relativistic jets emitting over a broad spectrum. Blazars are the subset of these jetted AGN whose jets are pointing very close to our line of sight, making the jet emission highly beamed and Doppler boosted, which results in bright and variable emission at all wavebands from radio to gamma-rays. The observed jet shows apparent superluminal motion (features of the jet appear to move faster than the speed of light across the plane of the sky) with speeds up to 40–50 $c$ . Gamma-ray transparency arguments applied to this gives lower limit on the bulk Lorentz factor for the jet, requiring  $\Gamma \approx 3 - 50$ . One peculiar characteristic of all the blazars is that their spectral energy distribution (SED) show two broad humps, peaking at low and high energy (figure 2 of [Hovatta and Lindfors, 2019](#), and figure 1 of [Costamante, 2020](#)). The first bump is generally attributed to the synchrotron emission from the population of relativistic electrons from the jet,

whereas the second bump is attributed to the inverse Compton (IC) scattering of seed photons by those high energy electrons. Emission from the jet is so bright that it masks the emission from the disk.

## 1.2 Relativistic AGN Jets

The study of highly collimated, relativistic AGN jets have a long history, since the discovery of an optical jet in the galaxy M87 (Curtis, 1918). As mentioned in § 1.1.1, large bulk Lorentz factors are implied by the observations of superluminal motion in blazars. These jets deposit huge amounts of kinetic energy on the extragalactic medium, which leads to the formation of giant radio lobes. Mechanisms responsible for the formation of these jets and their collimation over large distances (ranging from few parsecs to megaparsec scales) are still poorly understood, and remains an area of active research. It is now believed that these jets draw their power from the accretion process happening very close to the central black hole. The large asymptotic Lorentz factors of the jet observed far from the central engine are probably associated with the steep gradient in the gravitational potential in the vicinity of a black hole, from where the jet is supposed to be launched, making them powerful probes of strong-field gravity. This suggests the presence of extreme physical conditions at the base of the outflow. Although there is an overall consensus that the AGN jets are produced from the accretion disk in the black hole's surroundings, there are few studies which make explicit connections between the jet and the underlying accretion disk.

### 1.2.1 Jet launching mechanisms and their connection to accretion disks

The seminal work of Blandford and Znajek (1977) envisaged a scenario where energy and angular momentum is extracted electromagnetically from the spin of a black hole (Poynting flux dominated jet). In the Blandford-Znajek process, the large-scale poloidal magnetic field is assumed to be threaded by the black hole, and because of the frame dragging, the poloidal fields develop a toroidal component, which carries away black hole rotational energy. Tchekhovskoy et al. (2010) further investigate this mechanism using GRMHD simulations of black holes surrounded by thin accretion disks and threaded by magnetic flux.

The GRMHD simulations of Tchekhovskoy et al. (2011), and McKinney et al. (2012) propose the existence of magnetically arrested disks (MAD) as a possible launching mechanism for the jets. Accretion disk can accumulate large magnetic flux on black hole, until it becomes so strong that it obstructs the infall of gas, and

forms a MAD. MADs produce powerful jets very efficiently by extracting black hole spin energy. On the other hand, the treatment given by [Mondal and Mukhopadhyay \(2018\)](#) propose the mass loading of the jet from MAD.

Relativistic jets can also be produced by the magnetocentrifugal acceleration mechanism ([Blandford and Payne, 1982](#); [Rieger and Mannheim, 2000](#); [Lyutikov, 2009](#)). In this scenario, the rotational energy of the accretion disk is transferred to the overlying tenuous corona via magnetic stresses, and the gas is accelerated to relativistic speeds and collimated by the toroidal fields at large distances. In these treatments, the poloidal magnetic field is required to be inclined at a sufficiently small angle from the disk midplane, for the acceleration mechanism to be effective. Furthermore, there are stability issues with the magnetic confinement of the outflows ([Begelman, 1998](#)).

The radiation arising from the inner compact corona can also be responsible for the acceleration of jets. [Vyas et al. \(2015\)](#), [Vyas and Chattopadhyay \(2018\)](#), and [Joshi et al. \(2022\)](#) give the treatment of such radiatively driven jets and obtain semi-analytical solutions for steady state, radiatively driven outflows.

The pressure of the hot gas in the disk can lead to the formation of relativistic outflows via hydrodynamical acceleration in the inner regions of the disk ([Contopoulos and Kazanas, 1995](#); [Toma and Takahara, 2012](#)). In situ shocks and turbulence in the disk provide required heating of the gas, and the decay of relativistic neutrons throughout the jet can add to the power output of the outflow. In this scenario, if the thickness of the accretion disk (essentially the size of the neutron production region) is greater than the neutron flight path, then relativistic outflows are possible.

Advection-dominated accretion flows (ADAF) occur when the gas is unable to cool efficiently ([Ichimaru, 1977](#); [Narayan and Yi, 1994, 1995a,b](#)). In such flows, the gas becomes gravitationally unbound if the Bernoulli parameter becomes positive, and allows the existence of outflows. Relativistic treatment of self-similar inflow-outflow solutions of such flows was given by [Becker, Subramanian, and Kazanas \(2001\)](#), where they show the existence of relativistic winds originating from the inner parts of the accretion disk. These models lack the connection of the outflows with the underlying accretion disk since acceleration mechanisms are not taken into account.

[Subramanian, Becker, and Kazanas \(1999\)](#) proposed a mechanism which establishes a possible connection between relativistic outflow and the disk, where the outflows are powered by the second-order Fermi-acceleration mechanism governed by the shearing magnetic fields in the accretion disk coroneae. They show the formation of a nonthermal proton distribution in the corona, which leads to the formation of a pressure-driven wind. Such a wind passes through the critical (sonic) point and subsequently transforms into a relativistic jet at large distances from the black hole.

We have so far discussed a wide range of models for jet launching, ranging from Poynting flux-dominated jets to ones which address mass loading of such jets. These models address the origin of steady jets and winds. In addition to the steady, continuous background, some of the jets show discrete blobby features moving at relativistic speeds, e.g., the jet associated with the radio galaxy 3C 120 (Marscher et al., 2002; Chatterjee et al., 2009; Casadio et al., 2015a), and 3C 111 (Chatterjee et al., 2011). Some theoretical treatments consider these plasmoids as the shocks propagating down the jet, while some appeal to instabilities in steady-state accretion flow. We treat them as discrete packets of plasma that are ejected from the inner parts of an accretion disk. We explain the eruption of such blobs from the accretion disk corona by envisaging them as current carrying magnetic flux ropes which are subjected to the toroidal instability (TI). We then compare our model with the multi-epoch radio observations of the blobs in 3C 120. Detailed treatment of this model is given in Chapter 2.

We also work on the matter dominated steady relativistic winds from advection-dominated hot accretion flows. We do so by employing the second-order Fermi acceleration mechanism to hot protons in the flow, and deriving the proton distribution function and connecting it to the fluid description model of relativistic outflows from ADAF. In chapter 4, we show how the high energy non-thermal tail of the proton distribution function forms a relativistic wind.

### 1.2.2 Jet composition

Leptonic models have been successful in explaining the X-ray and soft gamma-ray ( $\lesssim 10$  MeV) components of typical AGN spectra, but they fail to explain the high-energy GeV and TeV emission observed from blazars. So, there arises a requirement of the presence of hadrons in the jet to explain the gamma-ray flaring observations at TeV energies (Sahu et al., 2019; Hoerbe et al., 2020; Gutiérrez et al., 2021). Hadronic models for a jet are becoming popular to explain the high-energy emission from blazars, and various mechanisms have been proposed to channel the required energy from protons to gamma-rays. GeV and TeV emission are explained convincingly by these models, involving either proton-induced cascades (Mannheim, 1993), or collisions between the high-energy jet protons and target protons located in the broad-line emission region (Dar and Laor, 1997). Since hadrons do not suffer from the severe radiative losses as that of electrons, it becomes one of the reasons for the applicability of the hadronic models to explain the GeV and TeV emission. Furthermore, GeV energies emerge as natural scales in hadronic processes such as the strong proton-proton interaction. Hence, we also deal with hadrons in our models of relativistic jets (both episodic and continuous).

### 1.3 Multi-wavelength Observations of 3C 120 and 3C 111

Radio galaxies 3C 120 and 3C 111 show some interesting observational features. While these sources present FR I and FR II morphologies respectively, they also show blazar-like behavior at radio frequencies, with their jets showing multiple superluminal blobs ejected at regular intervals from the central source. Their multi-wavelength observations show significant dips in the X-ray luminosity followed by ejections of superluminal radio components from the VLBI core (Chatterjee et al., 2009, 2011). Since the X-rays are thought to be emanating from the inner parts of an accretion disk, and radio waves from the jet, these observations imply that there is a specific connection between the events happening in the jet and the underlying accretion disk. This lends support to a scenario where some part of the coronal plasma is ejected as a plasmoid (leading to an X-ray dip) and is subsequently imaged at radio wavelengths, and some fraction of the corona gets swallowed by the central black hole. In Chapters 2 and 3, we try to explain these observations theoretically by establishing the accretion disk-jet connection in black hole sources.

### 1.4 Launching of Episodic Jets

A detailed investigation of the eruption mechanism of episodic blobs from the inner, hot accretion disk/corona is presented in Chapter 2. We explain the launching of such blobs by drawing analogies with the triggering of coronal mass ejections (CMEs) from the solar corona. Our Sun has a very dynamic atmosphere with complex magnetic field topology in the tenuous corona. It presents a situation where continuous, steady-state outflow (solar wind) is punctuated by occasional ejections of plasmoids called coronal mass ejections (CMEs). CMEs have been studied extensively both by ways of observations, and theory (which address the initiation and acceleration mechanisms of CMEs). CMEs are generally modeled as pre-existing current carrying magnetic flux-ropes which are prone to instabilities. In Chapter 2, we explore the torus instability (TI) model as a means of possible eruption of plasmoids from the accretion disk-coronae.

We treat these blobs (as mentioned in § 1.3) as pre-existing current carrying magnetic flux ropes that were initially anchored in the accretion disk-corona. The forces acting on the blob are 1) the Lorentz self-force or hoop force which tends to expand it outwards, away from the black hole 2) the Lorentz force due to the external poloidal field which tries to hold the blob down and 3) the gravitational attraction due to the black hole. If the Lorentz force due to the external poloidal field decreases sufficiently rapidly with distance from disk midplane, the flux rope is

subject to the MHD instability, called the “toroidal instability (TI)”, which causes it to erupt outwards. We solve the equation of motion for a blob and compare the time evolution of the ejected plasmoids resulting from our model with the multi-epoch radio observations of 3C 120. We also do the sensitivity analysis of the model predictions to changes in the model parameters, by way of outlining a viable parameter space. Further, we calculate the mass loss rate due to blob ejections from the accretion disk-corona, based on the assumption that the highly relativistic electrons are responsible for the observed radio emission (in the form of synchrotron radiation) from the blob, together with the observational estimates of the X-ray dip timescales. The findings of this work are published in [Shende, Subramanian, and Sachdeva \(2019\)](#).

## 1.5 Viscous Infalling Timescales of Inner Accretion Disks

The temporal behaviour of X-rays (dips mentioned in § 1.3) is thought to arise from the rapid collapse of the hot, inner parts of accretion disks. The collapse can occur over the radial infall time-scale of the inner accretion disk. The infall timescale is crucially governed by the operative viscosity, which has been commonly parametrized via the Shakura-Sunyaev  $\alpha$  viscosity parameter. Most researchers treat  $\alpha$  as a fitting parameter without worrying about the operative microphysical viscosity mechanism in the disk. Other than the constraint  $0 < \alpha < 1$ , not much is known about it. In Chapter 3, we investigate this issue and formulate a prescription for microphysical viscosity in the hot, inner regions of accretion disks. In addition to turbulent magnetic fields, we consider the presence of large scale toroidal fields in the hot accretion flow. The hot plasma in this region renders the protons collisionless (the mean free path for proton-proton collisions exceeds the disk height). But they can collide with the magnetic scattering centers (or “kinks”) in the turbulent magnetic fields. We use estimates for the diffusion coefficient from the literature dealing with detailed simulations of cosmic ray protons diffusing across a large-scale magnetic field in the presence of turbulence. We extract the effective mean free path from the diffusion coefficient, and compute the operative viscosity in the hot accretion disks, which we term the “hybrid” viscosity (since it is neither due to proton-proton collisions nor due to magnetic field stresses, but due to protons bouncing off magnetic scattering centres). We construct simplified disk models using this viscosity prescription and estimate disk collapse time scales for AGN 3C 120 and 3C 111, and a galactic microquasar GRS 1915+105. We find out the viable parameter space based on the X-ray variability of the mentioned sources. We also analyze the sensitivity of the infall

timescale ( $t_{\text{infall}}$ ) to the changes in model parameters. The findings of this work are published in [Shende, Chauhan, and Subramanian \(2021\)](#). The combined work of Chapters 2, and 3 outlines a plausible scenario for episodes of (inner) disc collapse accompanied by blob ejection.

## 1.6 Particle-dominated Relativistic Winds

In addition to studying episodic mass ejections, we have also worked on details of the origin of (matter dominated) steady winds from advection-dominated hot accretion disks. In Chapter 4, we build upon previous published work of [Becker, Subramanian, and Kazanas \(2001\)](#) which give the relativistic treatment of self-similar inflow-outflow solutions for advection-dominated accretion. While these solutions employ fluid equations to demonstrate the plausibility of (steady) relativistic winds, there have not been many attempts to link it to particle acceleration mechanisms in the hot, inner disk which presumably causes such outflows to form. In this work, we try to tie these two descriptions together by connecting the fluid description of self-similar inflow-outflow solutions of advection-dominated disks, and particle description of second-order Fermi acceleration mechanism governed by the shearing magnetic field in the disk. We have established a concrete disk-wind connection using this, and the results show how the high energy tail of the proton distribution function is ejected in the form of a relativistic wind.





# Chapter 2

## Episodic Jets From Black Hole Accretion Disks

### 2.1 Introduction

#### 2.1.1 Relativistic jets

Early observational evidence of a jet emanating from the central regions of any galaxy dates as far back as [Curtis \(1918\)](#), when the first optical jet from the elliptical galaxy M87 (in the virgo cluster) was discovered. Later on, the jet from the galaxy Cygnus A was observed at radio frequencies ([Hargrave and Ryle, 1974](#)). These observations paved the way for studying such interesting astrophysical phenomena in other sources in the universe as well. Since then, these highly collimated, relativistic outflows from active galaxies harboring black holes continue to engage our attention. Sources in our galaxy have also been shown to harbor miniature versions of such relativistic jets ([Mirabel and Rodríguez, 1994](#); [Fender et al., 1999](#); [Fender and Belloni, 2004](#)). To understand the physics of the underlying astrophysical events leading to these remarkable observations, many theoretical models have been proposed that address the issues such as the initial formation and acceleration of such relativistic jets and the manner in which they remain collimated at large distances. Many of these models address the origin of steady jets and winds, ranging from Poynting flux-dominated jets (e.g., [Blandford and Znajek, 1977](#); [Lovelace et al., 1987](#)) to ones which address the mass loading of such jets (e.g., [Blandford and Payne, 1982](#); [Ustyugova et al., 1999](#)). While most of such steady state jet models appeal to electrons as their primary constituents, some of them (e.g., [Contopoulos and Kazanas, 1995](#); [Subramanian, Becker, and Kazanas, 1999](#); [Le and Becker, 2004, 2005](#)) address the origin of hadrons in these jets.

### 2.1.2 Discrete blobs

In addition to a seemingly continuous background, several of these jets exhibit discrete blob-like structures moving at relativistic speeds, e.g., the jet associated with the radio galaxy 3C 120 (Marscher et al., 2002; Chatterjee et al., 2009; Casadio et al., 2015a,b), and blobs in GRS 1915+105 (Mirabel and Rodríguez, 1994; Fender et al., 1999; Fender and Belloni, 2004) and SS433 (Margon et al., 1979a,b), and also in the gravitational wave source, GW170817 (Punsly, 2019). Some theoretical treatment of these blobs appeal to concentrations of electrons accelerated by shocks travelling along the jet, while some think of them as discrete packets of plasma that are ejected from the inner regions of the accretion disk/corona. We adopt the latter scenario. Some models addressing the origin of such episodic emission appeal to instabilities or similar interruptions to steady-state accretion (e.g., non-steady shock scenario in sub-Keplerian accretion flow of magnetic TCAF model given by Chakrabarti et al., 2002; episodic ejection triggered by the time-dependent mean-field dynamo in the disk Stepanovs et al., 2014; formation of magnetic barriers in magnetically arrested disk (MAD) Mondal and Mukhopadhyay, 2018; escape of toroidal flux tubes due to magnetic buoyancy in the TCAF model Garain et al., 2020). Giannios et al. (2009) argue that spontaneous reconnection episodes in a Poynting flux dominated jet can produce small-scale jets (equivalently, small blobs of plasma) and Mizuta et al. (2018) employ GRMHD simulations to suggest that the episodic variations in the accretion rate can produce intense Alfvénic pulses.

On the other hand, the atmosphere of our Sun is very dynamic with complex magnetic configuration in the tenuous corona, and presents an instance of a steady state outflow (the solar wind) punctuated by occasional ejections of blobs (called coronal mass ejections; CMEs). CMEs from the solar corona have been extensively studied, both by way of observational data analysis (Gosling et al., 1974; Hundhausen et al., 1984; Bosman et al., 2012; Gopalswamy, 2013), and by way of models addressing their initiation mechanism (Lin and Forbes, 2000; Klimchuk, 2001; Török and Kliem, 2004; Zhang and Low, 2005; Kliem and Török, 2006; Isenberg and Forbes, 2007; Liu et al., 2016b; Cheng et al., 2017). Yuan et al. (2009) have adopted the solar CME initiation model of Lin and Forbes (2000) to explain the evolution and catastrophic ejection of a pre-existing flux rope plasmoid embedded in the corona of an accretion disk. The ejection process they appeal to is driven primarily by reconnection in the current sheet beneath the erupting plasmoid. In this paper, we explore the torus instability (TI) model (Kliem and Török, 2006) as a means of launching plasmoids and compare our results with observations of the source 3C 120 (Marscher et al., 2002; Chatterjee et al., 2009; Casadio et al., 2015a,b).

## 2.2 The Torus Instability Model

Before we get into the details of the TI model in the context of black hole accretion disk coronae, it is important to point out that the origin and evolution of magnetic fields in the accretion disks has been studied extensively and is still a subject of considerable investigation. The need of magnetically structured corona to explain the X-ray observations in black hole sources was proposed as far back as [Galeev et al. \(1979\)](#), where they study the amplification of magnetic fields by convective motions and differential rotation within a hot accretion disk. They show that the ineffectiveness of magnetic reconnection in limiting the field amplification leads to the emergence of small-scale, extremely hot coronal loops, which are believed to be responsible for the hard X-ray emission. [Uzdensky and Goodman \(2008\)](#) investigate this further by giving a statistical theory of a force-free magnetic field in the corona, where the field is represented by the assembly of closed magnetic loops with footpoints tied to the disk. They construct the kinetic equation that governs the evolution of these loops, which leads to the conditions under which the corona contributes to the outward angular momentum transport. The dynamics of magnetic loop configurations in the accretion disk coronae was also studied by [Romanova et al. \(1998\)](#) by way of 2D MHD simulations. They found that the loops open faster in the inner parts of the disk, and is followed by magnetically driven outflow from the disk.

On the other hand, [Contopoulos and Kazanas \(1998\)](#) propose a “cosmic battery” mechanism in which they show the origin and growth of poloidal fields generated by the strong azimuthal currents as a result of Poynting-Robertson drag effect in an optically thin advection dominated accretion flow. [Contopoulos et al. \(2015\)](#) and [Contopoulos et al. \(2018\)](#) further investigate this mechanism.

These studies are the ample evidence to support the idea that the accretion disk corona is magnetized. The corona can also be thought of as a bloated post-shock region of the two-component accretion flow (TCAF) model given by [Chakrabarti and Titarchuk \(1995\)](#).

Let us now delve into the mechanism of launching of plasmoids from the accretion disk coronae using the TI model. We envisage the plasmoid as a curved, flux rope structure carrying a toroidal current embedded in the accretion disk corona. A representative cartoon for this is shown in Figure (2.1). Studies on the laboratory tokamak plasmas show that the Lorentz self-forces (also referred to as magnetic hoop forces) acting on such a structure cause them to expand outward. The TI is suppressed by employing external poloidal fields in fusion devices. A similar kind of situation happens in the solar corona, where the flux rope is nominally held in place by overlying (ambient) magnetic fields. The flux rope is unstable against

expansion if the overlying fields decrease sufficiently rapidly with height, setting up its eruption outwards (Kliem and Török, 2006; Török and Kliem, 2007; Zuccarello et al., 2015; Sachdeva et al., 2017). A different mechanism of flux rope eruption, called the “magnetic catastrophe” was proposed by Lin and Forbes (2000), which study the effect of magnetic reconnection on the CME process. They model the CME as a two-dimensional flux rope, which is expelled by means of a catastrophic loss of MHD equilibrium, triggered by the reconnection in the current sheet beneath the flux rope. Interestingly, the equivalence between the TI model and the magnetic catastrophe model has been shown by Kliem et al. (2014); Démoulin and Aulanier (2010).

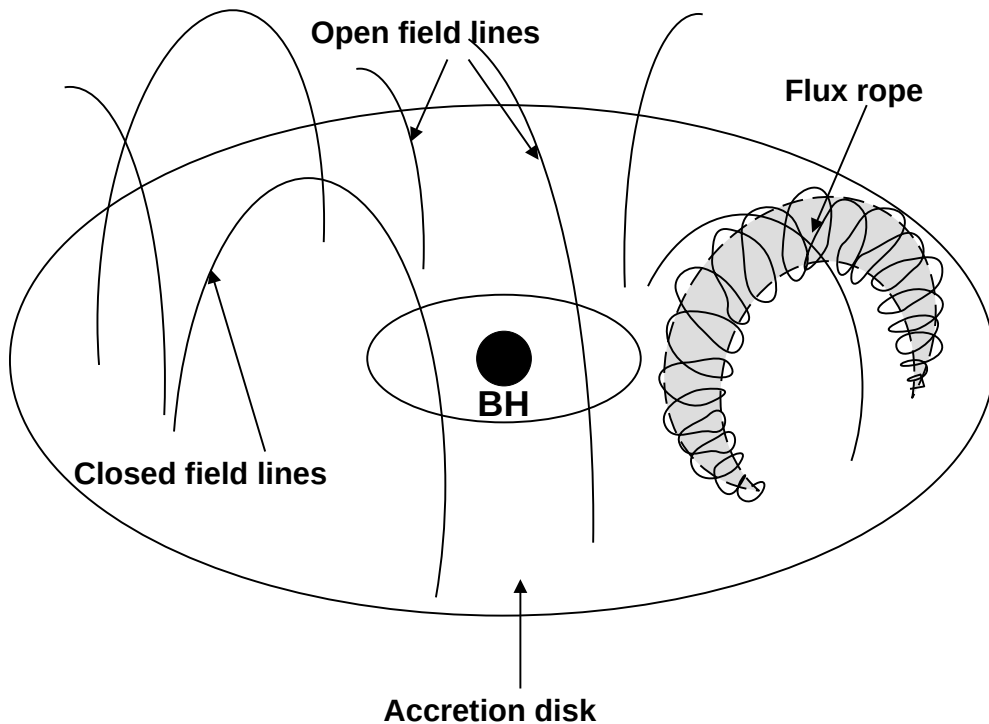


Figure 2.1: Plasmoid as a flux rope

For our situation of plasmoids as depicted in Figure (2.1), we adapt the TI model of Kliem and Török (2006) and prescribe the equation of motion for the flux rope plasmoid as

$$\Gamma \rho_m \frac{d^2 R}{dt^2} = \frac{I^2}{4\pi^2 b^2 R^2} \left( L + \frac{\mu_0 R}{2} \right) - \frac{I B_{\text{ext}}(R)}{\pi b^2} - \frac{\rho_m G M}{(R - 2R_g)^2} . \quad (2.1)$$

The quantity  $\Gamma \equiv (1 - v^2/c^2)^{-1/2}$  is the bulk Lorentz factor of the flux rope, with  $v$  being the velocity of the flux rope,  $\rho_m$  is the mass density inside it.  $R$  and  $b$  are the major and minor flux rope radii respectively. Strictly speaking, the flux rope major radius ( $R$ ) is equal to  $\sqrt{z^2 + r^2}$ , where  $r$  is the distance from the

central object along the equatorial midplane of the accretion disk (essentially the radius in cylindrical coordinates) and  $z$  is the height above the equatorial midplane. However, for practical purposes, we regard  $R$  to be the height of the plasmoid above the equatorial midplane - an approximation that gets better with increasing height from the central object. The total toroidal current is denoted by  $I$  and the overlying poloidal magnetic field is denoted by  $B_{\text{ext}}$ . We have prescribed the form of  $B_{\text{ext}}$  in Eq. (2.3) as a power law in  $R$ , with index  $n$ . The flux rope is assumed to be slender ( $R \gg b$ ), with an inductance given by  $L = \mu_0 R [\ln(8R/b) - 2 + l_i/2]$  (Landau et al., 1984). For concreteness, we consider the current density in the flux rope to be uniform, for which the internal inductance per unit length is  $l_i = 1/2$ . The quantity  $R_g \equiv GM/c^2$  is the gravitational radius with  $M$  being the mass of the black hole.

The first term on the right hand side of Eq. (2.1) describes the hoop force (Lorentz self-force) on the curved flux rope which causes it to expand outwards (Miyamoto, 1980; Bateman, 1978). The second term represents the competing Lorentz force arising from the current carried by the flux rope interacting with the external magnetic field  $B_{\text{ext}}$ , which tends to hold it down. If the second term decreases fast enough with  $R$ , the flux rope is subject to the torus instability, which causes it to erupt (Kliem and Török, 2006; Bateman, 1978). The third term on the right hand side of Eq. (2.1) represents the gravitational attraction of the black hole approximated by the pseudo-Newtonian potential appropriate to a Schwarzschild black hole (Paczynski and Wiita, 1980).

We do not include the terms arising from the gas pressure in our analysis. Inclusion of gas pressure effects inside the plasmoid would have involved an additional term proportional to  $(\bar{P} - P_a)/B_{pa}^2$  inside the parantheses of the first term on the right hand side of Eq. (2.1) (e.g., Miyamoto, 1980; Chen, 1996). Here,  $\bar{P}$  is the average gas pressure inside the plasmoid,  $P_a$  is the ambient pressure outside the plasmoid and  $B_{pa}$  denotes the poloidal magnetic field of the plasmoid evaluated at its outer boundary. There is substantial literature suggesting that the ambient corona is magnetic pressure dominant, i.e., it comprises a low- $\beta$  plasma (e.g., Liu et al., 2016a; Różańska et al., 2015 and also MRI simulations that address the vertical structure of the disk, such as Miller and Stone, 2000). We will show in § 2.3.3 below that the interior of the plasmoid is also a low- $\beta$  environment, as long as the proton temperature at the launching point is below  $\approx 10^{11}$  K. Since both the plasmoid and the ambient environment are magnetically dominated, our neglect of thermal pressure terms in Eq. (2.1) is justified. We also note that our treatment does not address any possible departures from axisymmetry in the plasmoid trajectory. We will have occasion to comment on this later, in § 2.3.2.

The total magnetic flux enclosed by the flux rope is

$$\Psi = \Psi_I + \Psi_{\text{ext}} = LI - 2\pi \int_0^R B_{\text{ext}}(r)rdr, \quad (2.2)$$

where  $\Psi_I = LI$  denotes the flux contained due to the magnetic fields inside the flux rope, and the flux due to external poloidal field enclosed by the flux rope is denoted by  $\Psi_{\text{ext}}$ . Following the prescription for  $B_{\text{ext}}$  given by Kliem and Török (2006), we assume that the expansion of flux rope doesn't perturb the external field and that it decreases with  $R$  as

$$B_{\text{ext}}(R) = \hat{B}R^{-n}, \quad n > 0. \quad (2.3)$$

Ideal MHD requires that the total flux be conserved during the evolution of a flux rope, which yields the following expression for the total current  $I$  inside a flux rope as a function  $R$  in terms of the current  $I_0$ , and the inductance  $L_0$  at the pre-eruption equilibrium position ( $R_0$ ):

$$I(R) = \frac{L_0 I_0}{L} + \frac{2\pi R_0^2 B_{\text{eq}}}{L(2-n)} \left[ \left( \frac{R}{R_0} \right)^{2-n} - 1 \right] \quad (2.4)$$

where  $B_{\text{eq}} = B_{\text{ext}}(R_0)$ , i.e., the value of external poloidal field at pre-eruption equilibrium position.

By making use of  $L = a\mu_0 R$ , where  $a$  is represented by the expression

$$a = \ln\left(\frac{8R}{b}\right) - 2 + \frac{l_i}{2}, \quad (2.5)$$

Eq. (2.4) can be reduced to

$$I(R) = \frac{a_0 R_0 I_0}{aR} \left\{ 1 + \frac{2\pi}{a_0 \mu_0 I_0} \frac{R_0 B_{\text{eq}}}{2-n} \left[ \left( \frac{R}{R_0} \right)^{2-n} - 1 \right] \right\}, \quad (2.6)$$

where  $a_0$  is the value of  $a$  at the pre-eruption equilibrium position  $R_0$ .

The aspect ratio ( $R/b$ ) of the flux rope is assumed to evolve as

$$\frac{R}{b} = \frac{R_0}{b_0} \rho^p \quad (2.7)$$

where  $\rho = R/R_0$  and  $R_0/b_0$  is the aspect ratio at the equilibrium position of the plasmoid. For concreteness, we assume the self-similar expansion ( $p = 0$ ), which means that the aspect ratio of the plasmoid ( $R/b$ ) remains constant as it evolves. The size  $d = 2b$  of the plasmoid can be written as

$$d = 2b = 2b_0 \rho^{1-p}, \quad (2.8)$$

where  $b_0$  denotes the flux rope minor radius at the pre-eruption equilibrium position. The pre-eruption equilibrium position of the plasmoid ( $R_0$ ) is determined by equating the right hand side of Eq (2.1) to zero.

Now the expression for  $I_0$  in Eq. (2.6) can be determined by equating the right hand side of Eq. (2.1) to zero, and given as

$$I_0 = \frac{2\pi R_0 B_{\text{eq}} A}{\mu_0 (a_0 + 1/2)}, \quad (2.9)$$

where

$$A = 1 + \sqrt{1 + \frac{\mu_0 c^2 b_0^2 \rho_{m0} (a_0 + 1/2)}{R_0 R_g B_{\text{eq}}^2 (R_{0*} - 2)^2}}. \quad (2.10)$$

Here,  $R_{0*} = R_0/R_g$ , i.e., the equilibrium position in units of  $R_g$ .

Using Eq. (2.9), Eq. (2.6) can be reduced further to give

$$I(R) = \frac{a_0 R_0 I_0}{aR} \left\{ 1 + \frac{a_0 + 1/2}{a_0} \frac{1}{A(2-n)} \left[ \left( \frac{R}{R_0} \right)^{2-n} - 1 \right] \right\} \quad (2.11)$$

Inserting Eq. (2.11) in Eq. (2.1), and making use of mass conservation ( $\Gamma_0 \rho_{m0} b_0^2 R_0 = \Gamma \rho_m b^2 R$ ,  $\Gamma_0 \approx 1$  since the launching speed is non-relativistic) yields the non-dimensionalized equation of motion for a plasmoid as

$$\frac{d^2 \rho}{d\tau^2} = \frac{a_0^2 (a_0 + 1/2)}{4a^2 (a_0 + 1/2)} A^2 Q^2 \rho^{-2} - \frac{a_0}{2a} A Q \rho^{-n} - \frac{T^2 c^2 R_g}{\Gamma R_0^3} \frac{1}{\left(\rho - \frac{2}{R_{0*}}\right)^2} \quad (2.12)$$

where  $\rho = R/R_0$  and  $\tau = t/T$ , with

$$T = \left( \frac{a_0 + 1/2}{4} \frac{b_0^2}{B_{\text{eq}}^2 / \mu_0 \rho_{m0}} \right)^{1/2} = \frac{(a_0 + 1/2)^{1/2} b_0}{2 V_{\text{Ah}}} \quad (2.13)$$

being the ‘‘hybrid’’ Alfvén crossing time of the minor radius, and  $V_{\text{Ah}} \equiv B_{\text{eq}} / \sqrt{\mu_0 \rho_{m0}}$  the ‘‘hybrid’’ Alfvén velocity. Non dimensional velocity and acceleration in terms of their dimensional counterparts are

$$\rho'(\tau) = \frac{d\rho}{d\tau} = \frac{T}{R_0} \frac{dR}{dt}, \quad \rho''(\tau) = \frac{d^2 \rho}{d\tau^2} = \frac{T^2}{R_0} \frac{d^2 R}{dt^2} \quad (2.14)$$

respectively. The quantity  $Q$  appearing in the first two terms of the right hand side of the Eq. (2.12) is expressed as

$$Q = 1 + \frac{(a_0 + 1/2) (\rho^{2-n} - 1)}{a_0 A(2-n)}. \quad (2.15)$$

The bulk Lorentz factor of the plasmoid ( $\Gamma$ ) can be expressed in terms of pa-

parameters  $V_{A_h}$  and  $R_0/b_0$  as

$$\Gamma = \left[ 1 - \left( \frac{R_0}{b_0} \right)^2 \frac{4V_{A_h}^2}{c^2(a_0 + 1/2)} \left( \frac{d\rho}{d\tau} \right)^2 \right]^{-\frac{1}{2}} \quad (2.16)$$

In non-relativistic limit ( $v \ll c$ , or equivalently,  $\Gamma = 1$ ) and ignoring gravity, Eq. (2.12) reduces to the equation of motion quoted in [Kliem and Török \(2006\)](#).

So, we solve the equation of motion Eq. (2.12) with the initial conditions and parameters specified in § 2.3.1.

## 2.3 Results and Comparison With Observations

### 2.3.1 Velocity and acceleration profiles of a blob

Our aim is to solve the equation of motion (Eq. 2.12, which is the non-dimensionalized version of Eq. 2.1) with suitable initial conditions and compare the results with multi-epoch observations of superluminal radio knots from 3C 120. The parameters required to solve this equation are  $M$ ,  $n$ ,  $R_0$ ,  $R_0/b_0$ ,  $p$ ,  $V_{A_h}$  and  $\beta_0$ .

We take the conditions at (pre-eruption) equilibrium position as the initial conditions to solve the equation of motion. We notice, at equilibrium position,  $R = R_0$ , and the launching velocity is  $v = v_0$ . Hence, the non-dimensionalized position and velocity of the flux rope at the (pre-eruption) equilibrium position are:

$$\begin{aligned} \rho(0) &= 1 \\ \rho'(0) &= \frac{v_0 T}{R_0} = \beta_0 \frac{cT}{R_0} \end{aligned} \quad (2.17)$$

where we have made use of the fact that  $\rho = R/R_0$ , and  $\rho'(\tau)$  is defined in Eq. (2.14). Also  $\beta_0$  is defined as  $\beta_0 \equiv v_0/c$ . A small perturbation from the equilibrium position causes the outward eruption of the flux rope, and we say the plasmoid is launched from the disk.

Before showing detailed comparisons with observations, we depict typical velocity and acceleration profiles of a representative blob in the figure (2.2). The parameters used for these results are  $p = 0$  (self-similar expansion),  $M = 5.5 \times 10^7 M_\odot$  (representative of 3C 120 - [Peterson et al., 2004](#)),  $R_0/b_0 = 10$ ,  $R_0 = 5 R_g$ ,  $n = 4$  and  $\beta_0 = 0.001$ . The different linestyles use different values of Hybrid Alfvén velocities ( $V_{A_h}$ ). We have also examined the velocity and acceleration profiles by varying the other parameters. The results for acceleration profiles are shown in the figure (2.4). We note that increasing  $V_{A_h}$ ,  $R_0/b_0$  and  $\beta_0$  and decreasing  $R_0$  results in lower values for the distance (and time) at which the blob acceleration reaches its peak. We conclude from this exercise that the acceleration profile peaks within 2 - 3 hours after



launch, and the blob reaches its asymptotic speed soon thereafter. The “core” of the radio jet of 3C 120 as defined by Chatterjee et al. (2009) to be the closest instance of a blob being imaged, is estimated to be  $\approx 0.22$  pc from the central black hole. Our results as depicted in figures (2.2), (2.3) and (2.4) imply that the multi-epoch radio observations can track the blobs’ motion only well after they have attained their asymptotic speed. From the figure (2.3), it can be noticed that the typical asymptotic speeds of  $\beta_{\text{asympt}} \approx 0.985$  are attained by a blob for the parameters given the figure.

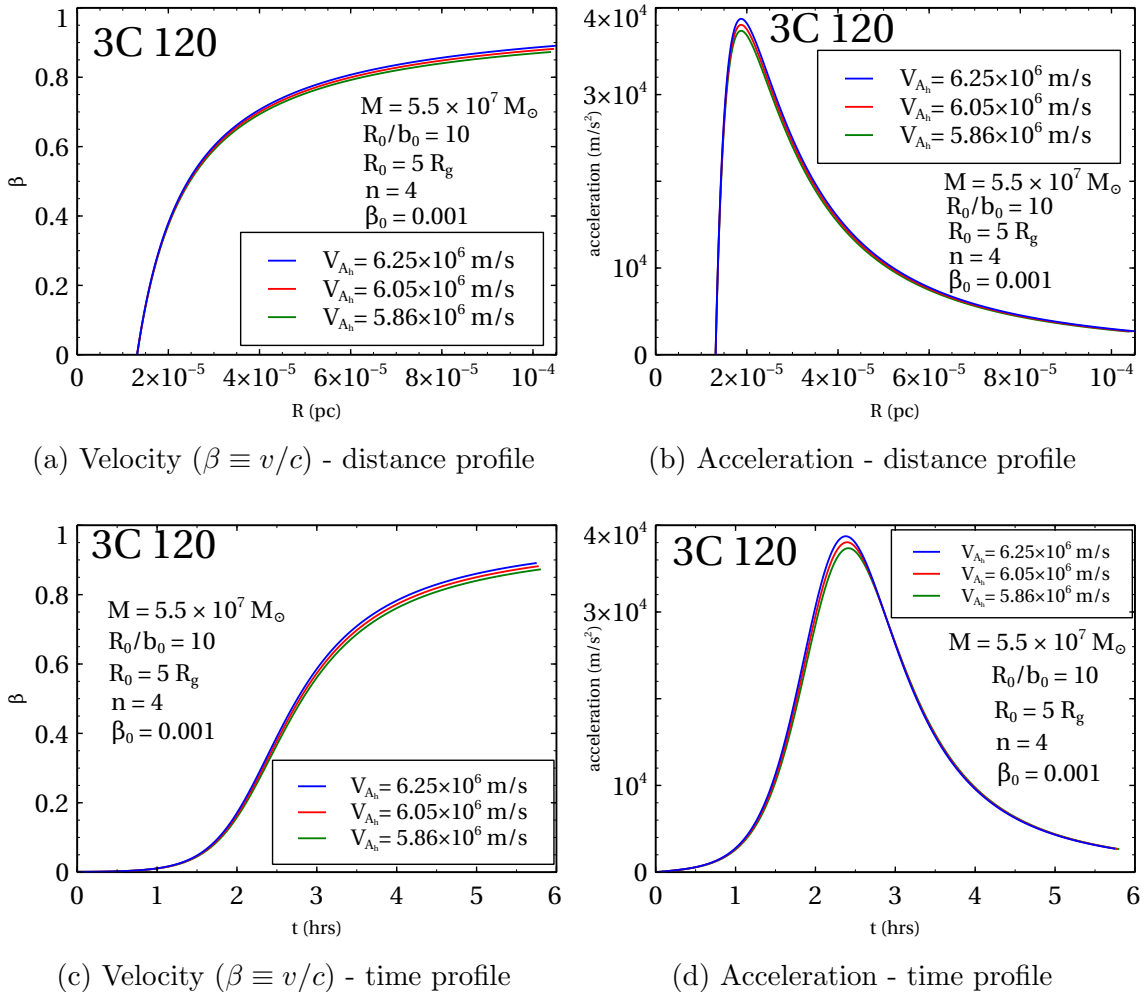


Figure 2.2: Velocity and acceleration profiles of a blob (upper panel: as functions of distance from the black hole, lower panel: as functions of time) for  $M = 5.5 \times 10^7 M_{\odot}$ ,  $R_0/b_0 = 10$ ,  $R_0 = 5 R_g$ ,  $n = 4$ ,  $p = 0$  and  $\beta_0 = 0.001$

### 2.3.2 Comparison with multi-epoch observations of 3C 120

We compare our model predictions with the radio observations of the superluminal knots (blobs) from the nearby ( $z = 0.033$ ) radio galaxy 3C 120 (Marscher et al., 2002; Chatterjee et al., 2009; Casadio et al., 2015a,b). While this source presents an

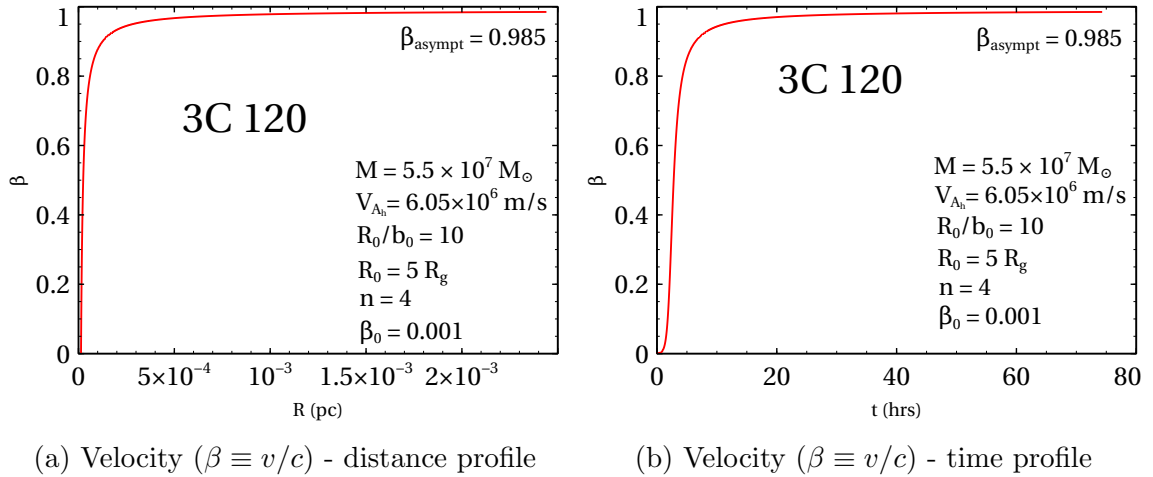


Figure 2.3: Velocity profiles of a blob showing the asymptotic velocity attained by a blob  $\beta_{\text{asympt}} = 0.985$

FRI morphology, it also has a blazar-like radio jet with multiple superluminal blobs being ejected at regular intervals from the central source (Casadio et al., 2015a,b). These multi-epoch observations at 15 and 43 GHz provide an elaborate picture of blob position as a function of time, and they are emitted at an angle  $\sim 20^\circ$  to the line of sight (as suggested by Gómez et al., 2000).

In their extensive multi-frequency monitoring of the radio galaxy 3C 120, Chatterjee et al. (2009) show that significant dips in the X-ray luminosity are followed by ejections of bright superluminal knots in the VLBA images. The time delay between the start of the X-ray dip and the time of blob ejection from the core is  $\approx 66 \pm 51$  days. Since the X-ray emission is believed to originate in the accretion disk corona, these observations suggest a scenario where the coronal plasma is occasionally “emptied”, and some fraction of the emptied plasma gets ejected outwards as a blob (much like a solar CME), which is later detected at radio frequencies, and the remaining fraction gets swallowed by the central black hole. While Marscher et al. (2002) were the first to suggest a connection between X-ray dips and blob ejections in 3C 120 based on their multi-frequency observations, Naik et al. (2001) report the detection of a series of X-ray dips associated with the appearance of a huge radio flare in the galactic microquasar GRS 1915+105. Nandi et al. (2001) also appeal to evacuation of the inner disk, for which they postulate the “magnetic rubber band effect” in trying to explain X-ray dips in GRS 1915+105. In 3C 120, the “radio core” of the jet (the first observed instance of a blob) is at a distance of  $\approx 0.22$  pc from the central object. As the blob travels away from the central object, the imaging is done at successive epochs. For the sake of concreteness, we concentrate on observations of blob E8 from Casadio et al. (2015a,b) at 15 GHz.

The apparent velocity of a blob ( $\beta_{\text{app}}$ ) as projected onto the plane of the sky is

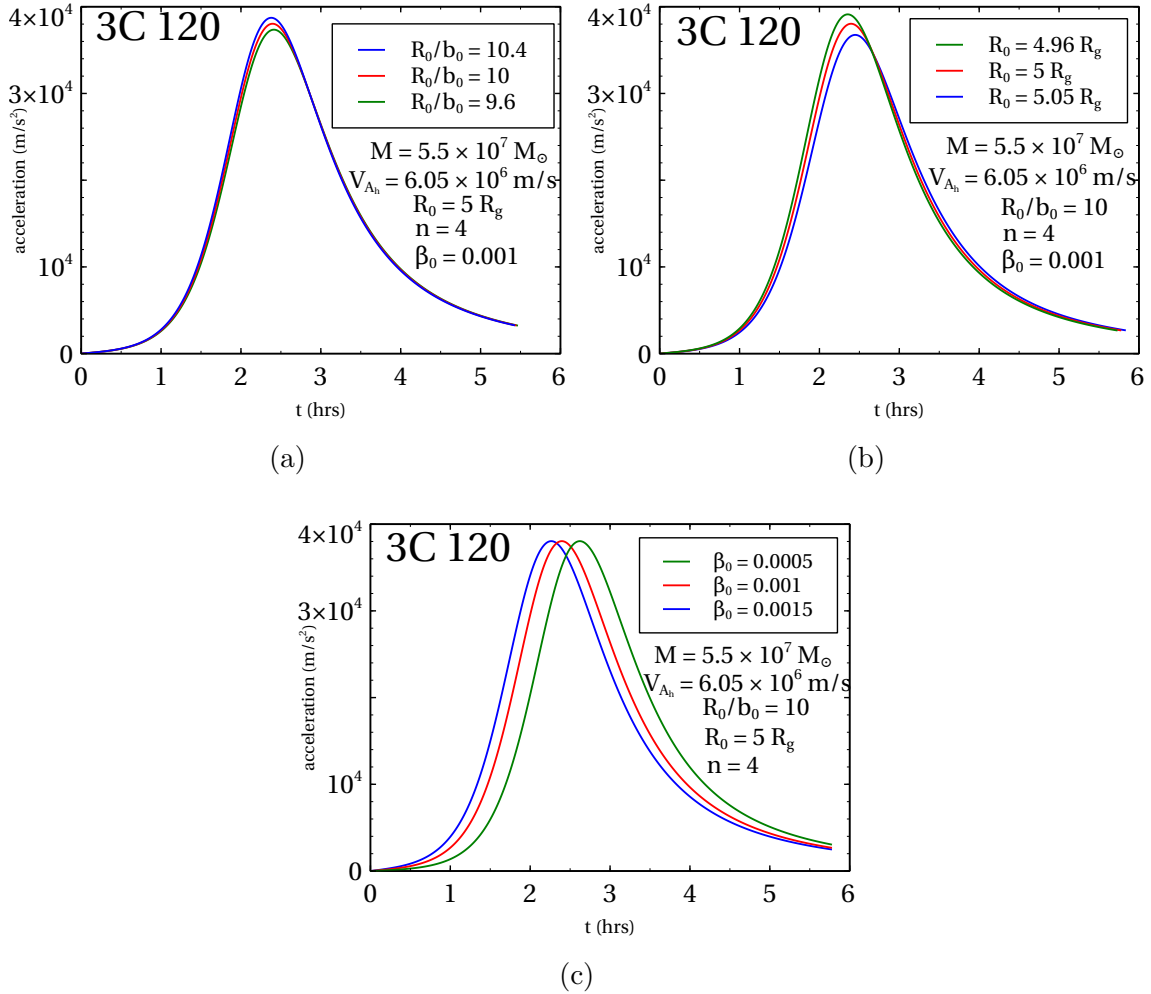


Figure 2.4: Acceleration profiles of a blob with different linestyles given in the inset corresponding to the parameter varied

related to its “true” velocity ( $\beta$ ) by

$$\beta_{\text{app}} = \frac{\beta \sin \theta}{1 - \beta \cos \theta}, \quad (2.18)$$

where  $\theta$  denotes the angle subtended by the blob’s trajectory with the line of sight. For observations of 3C 120,  $\theta$  is estimated to be  $\sim 20^\circ$  (Gómez et al., 2000).

The best fit model to multi-epoch observations of the blob E8 is obtained by parameter values  $R_0/b_0 = 10$ ,  $R_0 = 5 R_g$ ,  $n = 4$ ,  $V_{A_h} = 6.05 \times 10^6 \text{ m/s}$  and  $\beta_0 = 0.001$  which translates into launching Alfvénic Mach number  $\mathcal{M}_{A_h} \equiv v_0/V_{A_h} = 0.05$ . The mass of a black hole is taken to be  $M = 5.5 \times 10^7 M_{\odot}$  (Peterson et al., 2004). We note that the (pre-eruption) equilibrium position  $R_0 = 5 R_g$  can correspond to a position that is on the equatorial accretion disk midplane and 5 gravitational radii from the black hole, or to one that is slightly closer to the black hole and slightly above the disk midplane.

In order for the instability to be operative in the classical TI framework, the

overlying (ambient) magnetic field ( $B_{\text{ext}}$ ) must decrease sufficiently rapidly with height than a certain critical field (for which the power law exponent is  $n_{\text{crit}}$ ), i.e.,  $n > n_{\text{crit}} = 1.5$  in Eq. (2.3) (Kliem and Török, 2006). It is a reasonable expectation that the large-scale ambient magnetic field in the accretion disk corona should decay faster than that of a large-scale dipole (for which  $n = 3$ ). Brandenburg et al. (1995) in their 3D simulation model of dynamo-generated turbulence in the disk, relying on the magnetorotational instability (MRI), predict the generation of toroidal magnetic field of quadrupolar nature with respect to the disk midplane. On the other hand, a more intricate scenario is suggested in the recent GRMHD simulations (McKinney et al., 2012), where the large-scale magnetic fields develop depending on the initially assumed magnetic field configuration. Some initial toroidal magnetic field configurations seem to generate patches of dipolar field. Keeping these investigations in mind, we adopt  $n = 4$  for our best fit fiducial model. The best fit fiducial model (depicted by the red line) together with the data for blob E8 are shown in figure 2.5. The blue and green curves show deviations from the best fit, which have values for  $V_{A_h}$  differing by +2.14 and -3.31% (respectively) from that used for the best fit. The rest of the parameters are held fixed. The red line in figure 2.5, which represents the best fit to the trajectory of blob E8, seems to deviate somewhat from the observed positions at late times. To address this discrepancy, we think that the plasmoid could possibly have non-axisymmetric motion (or wobble), which cannot be captured by the plane-of-sky observations; some of the deviation could be attributed to this. Furthermore, our model cannot account for non-axisymmetric motion. The time taken for a blob corresponding to the best fit model to travel the distance of 0.22 pc from the launching point is  $\approx 53$  days. By comparison, the mean delay between the X-ray dip and the flaring of the radio core (which is interpreted as the time taken by the blob to travel the 0.22 pc between the black hole and the radio core) is  $66 \pm 51$  days (Chatterjee et al., 2009). So, our model prediction for the mentioned timescale falls within the range of observed timescales. The asymptotic superluminal velocity of the best fit model blob is  $4.83c$ , while the observed value is  $4.86c \pm 0.07c$  (Casadio et al., 2015a,b).

It is evident from our study that our best fit model is in good agreement with the observations of blob E8 (figure 2.5). But it is worth checking the sensitivity of the model predictions in response to changes in the parameters. We vary each parameter (while holding the rest of them fixed) to check how it affects the model prediction of the asymptotic blob velocity  $\beta_{\text{app}}$ . Table 2.1 presents the results of such a sensitivity study, and give an idea of the acceptable parameter space. We find that  $\beta_{\text{app}}$  is most sensitive to the hybrid Alfvén velocity  $V_{A_h}$ , equilibrium position  $R_0$  and the initial aspect ratio  $R_0/b_0$ . It is only moderately sensitive to  $n$ , and quite insensitive to the launching velocity  $\beta_0$ . We note that the second term in Eq (2.16) cannot exceed

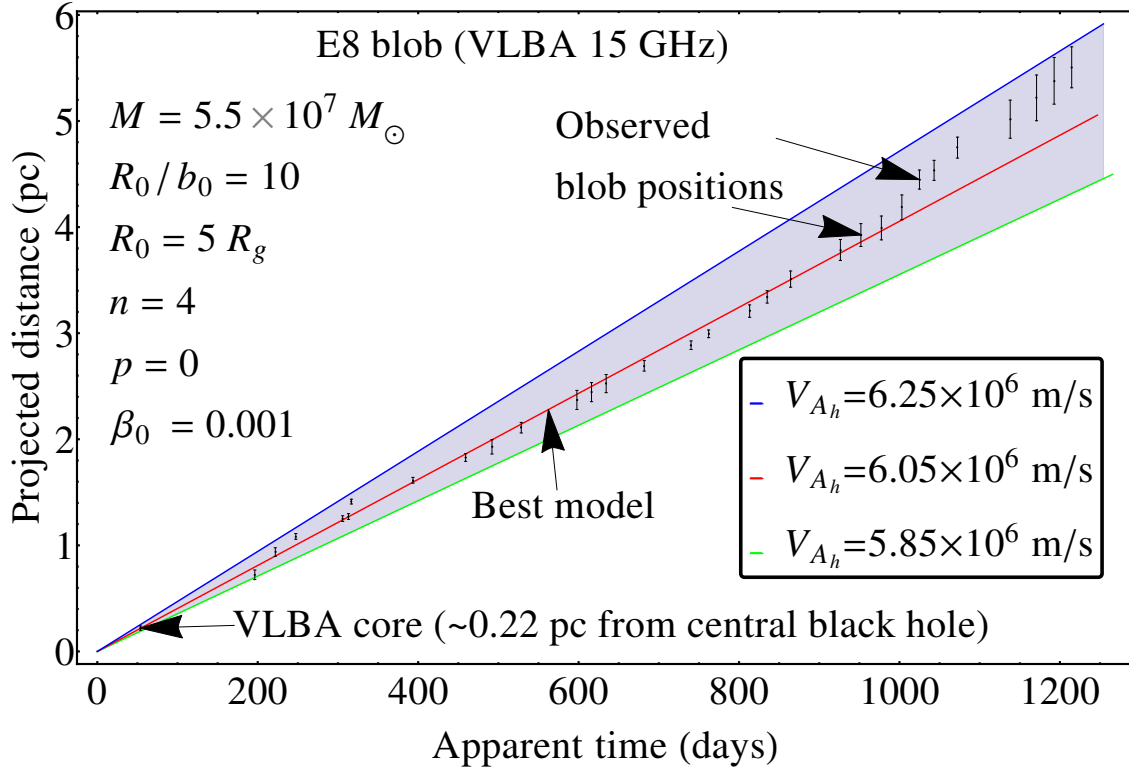


Figure 2.5: Height-time profile of a representative plasmoid for different values of  $V_{A_h}$  compared with observations of blob E8

unity; this translates into upper limits on the allowed values for  $V_{A_h}$  and  $R_0/b_0$ .

Similar analysis for the blob D11, which was observed at 43 GHz (Casadio et al., 2015a,b) was also carried out. We find that the sensitivity of  $\beta_{app}$  to the changes in the parameters of best fit model for blob D11 is similar to that for E8.

### 2.3.3 Mass loss rate due to blob ejection

It is possible from our model to determine the mass of an ejected blob and we can go on to further calculate the rate of mass loss in the blob launching process, based on the X-ray and radio observations of the radio galaxy 3C 120 (Chatterjee et al., 2009; Casadio et al., 2015a,b). First, we will focus on the radio observations to calculate the mass of a blob. A commonly understood explanation of the observed radio frequency from the blob is the synchrotron emission from the highly relativistic electrons gyrating in magnetic fields. There is a general assumption that these highly energetic electrons are confined within the blob by tangled magnetic fields. Our model has a definite prediction for the manner in which the plasmoid magnetic field varies with distance from the central object. The magnetic field carried by the blob can be extracted from the first term on the RHS of Eq. (2.1):

Table 2.1: An analysis of how the asymptotic  $\beta_{app}$  for blob E8 changes with model parameters

Parameter	Best fit	% change around best fit	% change in $\beta_{app}$
$V_{A_h}$	6050 km/s	-3.31 +2.14	-12.63 +16.15
$\beta_0$	0.001	-99 +900	-0.02 +0.1
$n$	4	-10 +10	+1.41 -0.93
$R_0$	$5 R_g$	-0.8 +1	+16.94 -15.16
$R_0/b_0$	10	-4 +4	-12.25 +16.15

$$B_{\text{blob}} = \frac{I}{4\pi R^2} \left( L + \frac{\mu_0 R}{2} \right), \quad (2.19)$$

which, using Eqs. (2.5, 2.9, 2.11), can be further reduced to

$$B_{\text{blob}} = \frac{a_0(a + 1/2)}{2a(a_0 + 1/2)} V_{A_h} \sqrt{\mu_0 n_0 (f m_p + m_e)} A Q \rho^{-2} \quad (2.20)$$

where we have used the expression for  $B_{\text{eq}} = V_{A_h} \sqrt{\mu_0 \rho_{m0}} = V_{A_h} \sqrt{\mu_0 n_0 (f m_p + m_e)}$ ,  $n_0$  being the number density of electrons at the (pre-eruption) equilibrium position of the plasmoid,  $f$  is the ratio of protons to electrons in the blob,  $m_p$  and  $m_e$  are the masses of a proton and electron respectively and  $A$  and  $Q$  are given by Eqs. (2.10) and (2.15) respectively.

Assuming that the tangled magnetic field that confines the relativistic electrons is represented by the magnetic field of a plasmoid leads us to estimate the mass of a blob  $M_{\text{blob}}$ . For simplicity, we assume that the observed radio emission from the blob is at the ‘‘critical’’ synchrotron frequency ( $\nu_c$ ) and that the pitch angle is  $90^\circ$ :

$$\nu_c = \frac{3}{4\pi} \frac{\gamma_c^2 e B_{\text{blob}}}{m_e}, \quad (2.21)$$

where  $\gamma_c$  is the random Lorentz factor of the radio emitting electrons (which is different from the quantity  $\Gamma$  which denotes the bulk Lorentz factor of the blob).

The condition that the energetic electrons be confined inside the blob by the magnetic field, demands that their Larmor radius ( $r_L$ ) must be a fraction (denoted by the confinement parameter  $\alpha \leq 1$ ) of the comoving size ( $d$ ) of the blob. In other words,

$$r_L = \frac{\gamma_c m_e c}{e B_{\text{blob}}} = \alpha d, \quad (2.22)$$

where  $d$  is comoving size of a blob given by Eq. (2.8). Using Eqs. (2.20)–(2.22), the condition  $\alpha \leq 1$  can be written as:

$$\alpha = \chi Q^{-3/2} \left( \frac{a}{a + 1/2} \right)^{3/2} \rho_{\text{ref}}^{2+p} n_0^{-3/4} \leq 1 \quad (2.23)$$

where

$$\chi = \frac{c}{b_0} \left( \frac{m_e}{e} \right)^{3/2} \left( \frac{\pi \nu_c}{3} \right)^{1/2} \left[ \frac{2(a_0 + 1/2)}{a_0} \right]^{3/2} (AV_{\text{Ah}})^{-3/2} [\mu_0(f m_p + m_e)]^{-3/4} \quad (2.24)$$

and  $\rho_{\text{ref}}$  represents the distance from the central object (in units of  $R_0$ ) where the condition  $\alpha \leq 1$  is imposed. Equivalently, the condition  $\alpha \leq 1$  defines the following minimum value for  $n_0$ , the number density of electrons at the pre-eruption equilibrium position of the flux rope:

$$n_0 \geq \chi^{4/3} \left( \frac{a}{a + 1/2} \right)^2 Q^{-2} \rho_{\text{ref}}^{\frac{4(2+p)}{3}} \quad (2.25)$$

It is evident from the Eq. (2.20) that the plasmoid magnetic field decreases with increasing distance from the central object. Accordingly, the value for the confinement parameter  $\alpha$  is expected to increase with distance. If, therefore,  $\alpha = 1$  at the farthest observed position of a given blob, the radio emitting electrons are guaranteed to remain confined within it all the way from the pre-eruption equilibrium position until this point.

The plasma- $\beta$  inside the blob/plasmoid is defined as

$$\beta_{\text{blob}} = \frac{\bar{P}}{B_{\text{blob}}^2 / 2\mu_0} \quad (2.26)$$

where  $\bar{P}$  is the average gas pressure inside the blob. For a magnetically dominated blob,  $\beta_{\text{blob}} < 1$  which translates into the following restriction on proton temperature:

$$T_p < \frac{2 v_{\text{Ablob}}^2 m_p}{k_B} \quad (2.27)$$

where  $k_B$  is the Boltzmann constant and  $v_{\text{Ablob}} = B_{\text{blob}} / \sqrt{\mu_0 m_p n}$  is the Alfvén velocity inside the blob. The quantity  $n$  is the number density of protons which varies with the distance from the central black hole ( $n = n_0$  at the launching point). We have also assumed here that  $T_p \gg T_e$  ( $T_e$  being the electron temperature) and that  $f = 1$  (i.e., there are equal numbers of electrons and protons). For the best fit model for blob E8, Eq. (2.27) predicts that the proton temperature  $T_p \lesssim 10^{11}\text{K}$  in order for the plasma- $\beta$  inside the blob ( $\beta_{\text{blob}}$ ) to be less than unity. This is a very reasonable condition, and we therefore conclude that the plasmoid/blob is a low  $\beta$

(i.e., magnetically dominated) plasma at launch.

For the representative blob E8 (observed at 15 GHz), the farthest observed position is  $\approx 5.5$  pc (Casadio et al., 2015a,b). Setting  $\alpha = 1$  at a projected distance  $R = 6$  pc from the central object (we use 6 pc instead of 5.5 pc for concreteness) yields  $n_0 = 4.88 \times 10^{15} \text{ m}^{-3}$ . The mass of the blob at the pre-eruption equilibrium position is related to  $n_0$  via

$$M_{\text{blob}} = 2\pi^2 b_0^2 R_0 n_0 (f m_p + m_e). \quad (2.28)$$

Shifting our attention to the X-ray observations of the radio galaxy 3C 120, we note that the duration of X-ray dips (5 to 120 days) quoted in Chatterjee et al. (2009) represent the timescales over which the blobs are ejected from the accretion disk-corona system. This allows us to estimate the blob mass ejection rate ( $\dot{M}_{\text{blob}}$ ) by way of dividing the value of mass of a blob (Eq. 2.28) by the mentioned X-ray dip timescales. A useful quantity to compare the blob mass ejection rate with is the Eddington accretion rate  $\dot{M}_{\text{E}} \equiv L_{\text{E}}/c^2$ , where  $L_{\text{E}} \equiv 4\pi G M c m_p / \sigma_{\text{T}}$  is the Eddington luminosity and  $\sigma_{\text{T}}$  is the Thomson electron scattering cross section. Using  $\nu_c = 15$  GHz,  $f = 1$  (equal numbers of electrons and protons), aspect ratio  $R/b = 10$ ,  $p = 0$  (self-similar expansion) and  $V_{\text{A}_h} = 6050$  km/s (which corresponds to the “best fit” model for this blob; table 2.1), we find that  $\dot{M}_{\text{blob}}/\dot{M}_{\text{E}}$  ranges from  $\approx 10^{-6}$  (for an X-ray dip duration of 120 days) to  $\approx 10^{-5}$  (for an X-ray dip duration of 5 days). This leads us to conclude that the rate at which the blobs carry away mass from the accretion disk corona is quite small in comparison to the Eddington accretion rate. We also note that an external magnetic field ( $B_{\text{ext}}$ ) of 194 G at the pre-eruption equilibrium position ( $R_0$ ) is implied by the requirement of  $\alpha = 1$  at 6 pc for our best-fit model. On the other hand, magnetic fields as high as tens of kG near the central object are often invoked (e.g. Schwartz, 2019) in order to satisfy observational constraints. Requiring that  $B_{\text{ext}}$  at  $R_0$  is larger by a factor of 100 translates to demanding  $\alpha = 0.001$  at a distance of 6 pc from the central object. This in turn increases  $n_0$  (Eq. 2.25), the mass of the blob (Eq. 2.28) and  $\dot{M}_{\text{blob}}$  by a factor of  $10^4$ , and  $10^{-1} \gtrsim \dot{M}_{\text{blob}}/\dot{M}_{\text{E}} \gtrsim 10^{-2}$ . The low values of  $\dot{M}_{\text{blob}}$  implies that most of the mass involved in the X-ray dips is probably swallowed by the black hole, and only a small fraction is channeled into the outward directed plasmoids. This is broadly consistent with the expectations of similar scenarios in the galactic black hole source GRS 1915+105 (Naik et al., 2001; Nandi et al., 2001).



## 2.4 Summary and Conclusions

There is ample evidence establishing the observational link between the episodic blobs in AGN and microquasar jets, and the accretion disk coronae surrounding the central black holes in these objects (Fender et al., 1999; Belloni, 2001; Fender and Belloni, 2004; Marscher et al., 2002; Chatterjee et al., 2009; Casadio et al., 2015a,b). We consider the blob/plasmoid to be a curved, current carrying magnetic flux rope that is anchored in the accretion disk corona prior to eruption. This is a complementary approach to that of Uzdensky and Goodman (2008) who give a statistical theory of a force-free magnetic field in the corona and Giannios et al. (2009) who propose ‘jets-in-a-jet’ model to explain the TeV variability in some blazars. They consider the plasmoids to be spontaneously formed as a result of reconnection in the steady (Poynting flux dominated) jet. In our depiction of the episodic jet launching model, the plasmoid is subject to two kinds of Lorentz forces - one is the so-called “hoop force” (also called the Lorentz self-force), which arises in any curved flux tube carrying an axial current. Owing to the difference in magnetic pressures at the bottom and top of the bent flux tube (Mouschovias and Poland, 1978), this hoop force tends to push it outwards, away from the central object. The other kind of Lorentz force arises due the interaction of the plasmoid current and the overlying poloidal field; this force tries to “hold down” the flux rope plasmoid, and prevent it from erupting. If the magnitude of the overlying (ambient) magnetic field decreases sufficiently rapidly with height, then it gives rise to the MHD instability called the “toroidal instability” (TI) and we get the outward eruption of the flux rope plasmoid like a whiplash. This approach has been applied quite effectively to explain the eruption of coronal mass ejections (CMEs) from the solar corona, and has held up to detailed comparison with observations (Sachdeva et al., 2017; Gou et al., 2018).

In this work, the role of the TI in launching plasmoids from the accretion disk corona has been investigated, and comparisons are made between our model predictions with multi-epoch radio wavelength imaging observations of 3C 120 (Chatterjee et al., 2009; Casadio et al., 2015a,b). This system exhibits dips in the X-ray luminosity followed by the ejection of plasmoids. Since the X-ray emission is thought to originate in the corona, this lends support to a picture where parts of the coronal plasma are ejected in plasmoids (leading to X-ray dips) and is subsequently imaged at radio wavelengths, and some fraction of the corona gets swallowed by the central black hole. We demonstrate that our model predictions for the time evolution of the ejected plasmoids agree well with the observed trajectories of the radio blobs in the 3C 120 system. We also analyze the sensitivity of the model predictions to changes in the model parameters, by way of outlining a viable parameter space. It is commonly assumed that the highly relativistic electrons responsible for radio emis-

sion from the blobs are confined within it by tangled magnetic fields. We use this, together with other model assumptions and observational estimates of the X-ray dip timescales to determine the mass loss rate due to plasmoid ejection. We find that this rate is typically a very small fraction of the Eddington accretion rate for 3C 120. This is roughly similar to solar coronal mass ejections, which carry away a negligible fraction of the total mass contained in the solar corona. In summary, we have shown that the torus instability of flux rope plasmoids rooted in the accretion disk corona offers a convincing explanation for the observed episodic ejection of blobs from AGN and microquasars.

# Chapter 3

## X-ray Dips in AGNs And Microquasars – Collapse Time-scales of Inner Accretion Disk

### 3.1 Introduction

It is now a general consensus that the AGNs and microquasars are powered primarily by the accretion of matter onto the black hole sitting at their center. The gravitational potential energy of the spiralling infalling gas in an accretion disk is released in the form of radiation. Although the radiation is emitted over a wide range of wavelengths, the one aspect that attracts attention is the often complex behavior of X-ray intensity from such sources. These X-rays are commonly believed to be emanating from the hot inner parts of the accretion disk surrounding the central black hole, and as a consequence, the dynamics of the hot inner disk decides the temporal behavior of X-rays emitted by it.

From its discovery ([Castro-Tirado et al., 1992](#)), the galactic microquasar GRS 1915+105 has been studied extensively because of its remarkably rich diverse observations across the entire electromagnetic spectrum, more so in the X-rays. Its complicated X-ray behavior is generally described by the rapid removal and gradual replenishment of the inner accretion disk (e.g., [Belloni et al. 1997](#)). Further studies of this source ([Yadav et al., 1999](#); [Naik et al., 2001](#); [Vadawale et al., 2001, 2003](#)) explain the X-ray temporal variability on the basis of the dynamics of the sub-Keplerian, post-shock halo of a two-component advective flow around the central black hole (e.g., the TCAF model of [Chakrabarti and Titarchuk, 1995](#)). On the other hand, observations showing dips in the X-ray luminosities have been re-

ported from the AGN sources 3C 120 and 3C 111 (Marscher et al., 2002; Marscher and Jorstad, 2006; Chatterjee et al., 2009, 2011). Interestingly, these X-ray dips are followed by the ejection of bright superluminal knots from the core of the jet at radio frequencies. These two phenomena are thought to be related to each other. Shende, Subramanian, and Sachdeva (2019) showed that such episodic plasma ejections could be launched in a manner similar to solar coronal mass ejections, with time of the ejection from the inner hot disk coinciding with the onset of X-ray dip. Such ejections have also been reported from GRS 1915+105 by Naik et al. (2001), and Vadawale et al. (2001, 2003).

In this work, we try to explain some aspects of the X-ray temporal variability in these sources, based on the interpretation of the infall/collapse timescales of the hot, inner accretion disk in such sources. For GRS 1915+105, this would correspond to the fast rise timescales of a few seconds in the outburst state, which has been attributed to the infall timescale of the sub-Keplerian, post shock halo of the TCAF (the quantity  $t_{\text{vis}}^{\text{h}}$  in Yadav et al. 1999). We show that this infall timescale corresponds to the viscous timescale in the hot inner disk. We want to point out that this is different from the slow viscous timescale of the outer, cold thin disk that is held responsible for the regeneration of the entire inner disk in Belloni et al. (1997). For the extragalactic sources 3C 120 and 3C 111, we seek to interpret the X-ray dip timescales. The highlight of this work is that we give the prescription for the microphysical viscosity mechanism operative in hot inner disk (instead of adopting values for the Shakura-Sunyaev  $\alpha$  parameter) to estimate the viscous timescale associated with it. Two-temperature, hot accretion disks are considered, where the electron temperatures are  $\approx 10^9$  K (which are believed to be responsible for the emission of X-rays due to Comptonization) and the proton temperatures are in excess of  $10^{11}$  K. The hot protons in the two-temperature plasma are effectively collisionless, since the mean free path for the proton-proton collisions exceeds the disk height. An analogous astrophysical situation is that of the cosmic rays diffusing in turbulent magnetic fields, in presence of large scale, ordered magnetic fields. The collisionless protons in the hot inner disk are much like collisionless cosmic ray protons. We use published cosmic ray diffusion coefficients in turbulent magnetic fields based on the simulations done by Candia and Roulet (2004), and Snodin et al. (2016) to estimate the effective viscosity in hot accretion disks and construct simplified disk models using it. The infall timescale is calculated using these disk models.

## 3.2 Hybrid Viscosity in Hot Accretion Disks

Viscosity in accretion disks is central to understanding the amount of angular momentum transport generated in the disk, leading to the observed luminosities in

black hole sources. Most of the observations referred in the previous section are interpreted by invoking a hot inner accretion disk/corona which is responsible for Comptonized X-rays. In this work, we aim to identify the collapse timescale of the inner accretion disk with the viscous infall timescale in this region. The pioneering work of [Shakura and Sunyaev \(1973\)](#) laid the foundation for many accretion disk models wherein viscosity in the accretion disks is parametrized in terms of the dimensionless  $\alpha$  parameter. The viscous stresses in the disk are parametrized as  $\alpha P$ , where  $P$  is the gas pressure in the disk ([Shapiro, Lightman, and Eardley, 1976](#); [Eilek and Kafatos, 1983](#); [Kafatos, 1988](#); [Subramanian, Becker, and Kafatos, 1996](#); [Belloni et al., 1997](#)). The observable properties of accretion disks were seen to be pretty insensitive functions of  $\alpha$ . As a result, the values of  $\alpha$  are not very well constrained, and this reflects the lack of our knowledge concerning the microphysical nature of viscosity. This issue is more striking in the hot inner parts of the accretion disk, where the plasma is so hot that the disk is puffed up and the plasma is collisionless, i.e., the mean free path of hot protons typically exceeds macroscopic lengths such as the disk height. Since the proton-proton collisions are very rare, their contribution to the operative viscosity in the disk is negligible. On the other hand, [Subramanian, Becker, and Kafatos \(1996\)](#) (SBK96 from now on) proposed the “hybrid viscosity” model for hot inner accretion disks, where they showed that protons can scatter off the magnetic irregularities (also called the magnetic scattering centers) arising due to magnetic turbulence. These proton-magnetic scattering centre collisions are essentially wave-particle interactions between the protons and the turbulent wave spectrum which gives rise to a “hybrid” kind of viscosity, that is neither due to particle collisions alone nor due to Reynolds stresses from the magnetic field (alone). It is to be noted that the hybrid viscosity is also influenced by the degree to which the magnetic field is tangled. SBK96 represent this by introducing the dimensionless lengthscale  $\xi = \lambda_{\text{coh}}/H$ , where  $\lambda_{\text{coh}}$  is the average distance between the magnetic scattering centers and  $H$  is the half-thickness of the disk. But their work was limited to considering only a single lengthscale (i.e., single value of  $\xi$  at a time) in the magnetic irregularity spectrum. Furthermore, it did not take into account the likely presence of a large scale, ordered toroidal magnetic field embedded in the accretion disk - a feature suggested by simulations of the magnetorotational instability ([Balbus and Hawley, 1991](#); [Hawley and Balbus, 1991](#); [Balbus and Hawley, 1998](#); [Quataert et al., 2002](#); [Sharma et al., 2003](#)) which is thought to be responsible for the generation of magnetic turbulence. On the other hand, the propagation and scattering of cosmic rays in the presence of turbulent magnetic irregularities have been studied for long ([Parker, 1965](#); [Jokipii, 1966](#); [Giacalone and Jokipii, 1999](#)). This scenario is similar to that of the hot inner regions of the accretion disk, in that the energetic cosmic ray protons traveling in the interplanetary and interstellar medium

are collisionless, and are scattered off from the magnetic irregularities present in the medium due to magnetic turbulence. We can make use of the diffusion coefficients derived in these studies to calculate the relevant mean free path of protons (and subsequently, the viscosity coefficient) in hot accretion disks. Estimates of the diffusion tensor were obtained in some simulation studies for cosmic ray transport in turbulent magnetic fields (Casse et al., 2002; Candia and Roulet, 2004; Snodin et al., 2016).

In this work, we compute the hybrid viscosity in the accretion disks arising due to the hot protons diffusing through tangled magnetic fields, by way of utilizing the analytical fits to diffusion coefficients provided by Candia and Roulet (2004) and Snodin et al. (2016). By assuming the presence of a large-scale ordered magnetic field in addition to a small-scale turbulent field, they give expressions for all the components of the diffusion tensor for cosmic rays propagating through the interstellar medium. This includes the diffusion coefficient for transport parallel to the large scale field ( $D_{\parallel}$ ) and perpendicular to it ( $D_{\perp}$ ). We use these diffusion coefficients to formulate the mean free path of hot protons and compute the viscosity relevant to our situation. As mentioned earlier, the evidence for a large scale toroidal magnetic field embedded in magnetized accretion disks has been reported in various studies (e.g., Matsumoto and Tajima, 1995). So, we take into account the presence of large scale toroidal ( $\hat{\phi}$  directed) field in the hot accretion disk, in addition to the turbulent magnetic field. Since the angular momentum is transported outwards via the viscous stresses in the disk, and leads to radially inward accretion, our main focus is on the  $r - \phi$  component of the viscosity tensor (Shakura and Sunyaev, 1973; Frank, King, and Raine, 2002). Therefore, to achieve the radially outward transport of angular momentum in the disk, the quantity of interest for us is the mean free path derived from the proton diffusion coefficient perpendicular to  $\hat{\phi}$  direction (since the radial direction is  $\perp \hat{\phi}$ ) to compute the effective viscosity.

### 3.2.1 Hybrid Viscosity using $D_{\perp}$ from Candia & Roulet

Of the analytical fits given by Candia and Roulet (2004) for the entire diffusion tensor for cosmic ray propagation and scattering, we use the expression for the perpendicular diffusion coefficient  $D_{\perp}$  in what follows, in order to obtain the outward angular momentum transport in the hot accretion disk as mentioned earlier.  $D_{\perp}$  represents the diffusion coefficient perpendicular to the large scale field, which, in our case, is in the  $\hat{\phi}$  direction. A preliminary account of this treatment was given in Subramanian et al. (2005).

From Eqs. (18) and (19) of Candia and Roulet (2004), we get the expression for

$D_{\perp}$  as

$$D_{\perp} = v_{\text{rms}} H D_c \quad \text{cm}^2 \text{s}^{-1} \quad (3.1)$$

Here, the representative macroscopic scale length is denoted by the disk height  $H$ , and the proton rms speed  $v_{\text{rms}} \equiv \sqrt{3k_{\text{B}}T_i/m_{\text{p}}}$  (where  $k_{\text{B}}$ ,  $T_i$  and  $m_{\text{p}}$  denote Boltzmann's constant, proton temperature and proton mass respectively) is used as a representative speed. Hot ( $\sim 10^{12}\text{K}$ ) protons we consider have energies of the order of 86 MeV, and are therefore non-relativistic. The quantity  $D_c$  is given by

$$D_c = N_{\perp} (\sigma^2)^{a_{\perp}} \frac{N_{\parallel}}{\sigma^2} \left[ \left( \frac{\rho}{\rho_{\parallel}} \right)^{2(1-\gamma)} + \left( \frac{\rho}{\rho_{\parallel}} \right)^2 \right]^{1/2} \quad (3.2)$$

$$\times \begin{cases} \rho & 0 < \rho \leq 0.2 \\ 0.04/\rho & 0.2 < \rho < 1 \end{cases}$$

where  $\sigma^2 \equiv \langle B_r^2 \rangle / \langle B_0^2 \rangle$  is a measure of the turbulence level and defined by the ratio of energy density in the small scale turbulent magnetic fields ( $B_r^2$ ) to that in the large-scale field ( $B_0^2$ ). The quantity  $\rho \equiv r_L/H$  represents magnetic rigidity and is defined as the ratio of the Larmor radius of a proton ( $r_L$ ) to a macroscopic scale length (which we take to be the disk height  $H$ ). The parameters  $a_{\perp}$ ,  $N_{\perp}$ ,  $N_{\parallel}$ ,  $\rho_{\parallel}$ , and  $\gamma$  are specific to different kinds of turbulence, and are defined in Table 1 of [Candia and Roulet \(2004\)](#).

The coefficient of dynamic viscosity is usually defined as

$$\eta \text{ (g cm}^{-1}\text{s}^{-1}\text{)} = Nm v \lambda, \quad (3.3)$$

where  $N$  and  $m$  are the number density and mass of the relevant particles,  $v$  is the relevant velocity (in our case, the thermal rms velocity  $v_{\text{rms}}$ ) and  $\lambda$  is the relevant mean free path ([Spitzer, 1962](#); [Mihalas and Mihalas, 1984](#)). On the other hand, the diffusion coefficient  $D$  is usually defined as

$$D \text{ (cm}^2 \text{ s}^{-1}\text{)} = v \lambda, \quad (3.4)$$

where  $v$  is the relevant velocity and  $\lambda$  is the relevant mean free path. Combining Eqs. (3.3) and (3.4), we get  $\eta = NmD$ . The coefficient of dynamic viscosity relevant for our situation is therefore

$$\eta_{\text{hyb}} = N_i m_{\text{p}} D_{\perp}, \quad (3.5)$$

### 3.2.2 Solutions for disk model

As mentioned earlier, since X-rays are thought to emanate from the hot inner regions of an accretion disk, our focus is on the two-temperature accretion disk model

originally proposed by Shapiro, Lightman, and Eardley (1976), then later used by Eilek and Kafatos (1983), and SBK96. The basic disk structure equations for the same are given in Appendix A. These equations are obtained by approximating the relevant differential equations by scaling relations, e.g.,  $\partial/\partial R \rightarrow 1/R$ ,  $\partial/\partial z \rightarrow 1/H$ . Using Eq. (3.1) and Eq. (A.7), Eq. (3.5) can be written as

$$\eta_{\text{hyb}} = 2.52 \tau_{\text{es}} v_{\text{rms}} D_c \quad (3.6)$$

Using the hybrid viscosity prescription of Eq. (3.6) in Eq. (A.1), and making use of the Eqs. (A.5), (A.8), and (A.10), and assuming  $T_i \gg T_e$ , we get the following expression for the Shakura-Sunyaev viscosity parameter  $\alpha_{\text{hyb}}$ :

$$\alpha_{\text{hyb}} = 2.63 f_1^{-1/2} D_c \quad (3.7)$$

Using Eqs. (A.4), (A.7), (A.8)–(A.10) and Eq. (3.7) for  $\alpha_{\text{hyb}}$ , we get the following implicit equation for the electron scattering optical depth  $\tau_{\text{es}}$ :

$$\begin{aligned} \tau_{\text{es}}^3 (1 + \tau_{\text{es}})^{3/2} &= 272.5 (\ln \Lambda)^{-1} \left( \frac{\dot{M}}{\dot{M}_E} \right)^{1/2} f_1^{-1/2} f_2^{-1/2} f_3 y^{3/2} \alpha_{\text{hyb}}^{1/2} R_*^{-3/4} \\ &= 442 (\ln \Lambda)^{-1} \left( \frac{\dot{M}}{\dot{M}_E} \right)^{1/2} f_1^{-3/4} f_2^{-1/2} f_3 y^{3/2} D_c^{1/2} R_*^{-3/4} \end{aligned} \quad (3.8)$$

The expressions for  $\alpha_{\text{hyb}}$  (Eq. 3.7) and  $\tau_{\text{es}}$  (Eq. 3.8), along with Eqs. (A.1)–(A.10) yield the following self-consistent solutions for the disk model:

$$T_i = 4.1 \times 10^{12} \left( \frac{\dot{M}}{\dot{M}_E} \right) f_1^{1/2} f_2 \tau_{\text{es}}^{-1} D_c^{-1} R_*^{-3/2} \quad (3.9)$$

$$T_e = 1.48 \times 10^9 y \tau_{\text{es}}^{-1} [g(\tau_{\text{es}})]^{-1} \quad (3.10)$$

$$N_i = 1.65 \times 10^{11} \left( \frac{\dot{M}}{\dot{M}_E} \right)^{-1/2} M_8^{-1} f_1^{1/4} f_2^{-1/2} D_c^{1/2} \tau_{\text{es}}^{3/2} R_*^{-3/4} \quad (3.11)$$

$$\frac{H}{R} = 0.62 \left( \frac{\dot{M}}{\dot{M}_E} \right)^{1/2} f_1^{-1/4} f_2^{1/2} \tau_{\text{es}}^{-1/2} D_c^{-1/2} R_*^{-1/4} \quad (3.12)$$

In these equations, the quantity  $R_*$  represents the disk radius in units of the gravitational radius ( $R_g = GM/c^2$ ,  $R_* = R/R_g$ ),  $M_8$  represents the black hole's mass in units of  $10^8$  solar masses,  $\dot{M}/\dot{M}_E$  represents the accretion rate in units of Eddington rate ( $\dot{M}_E \equiv L_E/c^2$ , where  $L_E \equiv 4\pi GMm_p c/\sigma_T$  is the Eddington luminosity and  $\sigma_T$  is the Thomson electron scattering cross section),  $T_i$  is the proton temperature and  $T_e$  is the electron temperature (in Kelvin),  $N_i$  is the number density



of protons in units of  $\text{cm}^{-3}$ ,  $y$  is the Compton  $y$ -parameter, and  $g(\tau_{\text{es}}) \equiv 1 + \tau_{\text{es}}$ .

### 3.2.3 Model Self-Consistency Conditions

We first lay down the following self-consistency conditions which need to be satisfied by each of the disk models we consider, prior to evaluating the viscous timescales:

1.  $H/R \lesssim 1$  : the slim disk condition, which is implicit in the equation of vertical hydrostatic equilibrium (Eq. A.2).
2.  $T_i \gg T_e$  : the two-temperature condition.
3.  $\lambda_{ii}/H \gg 1$  and  $\lambda/H, \lambda/R < 1$  : the mean free path  $\lambda_{ii}$  for proton-proton collisions is much larger than the disk height (i.e., the protons are collisionless), but the effective mean free path  $\lambda$  (arising out of proton-turbulent wave spectrum interaction) is smaller than  $H$ .

Representative accretion disk models for 3C 120, and GRS 1915+105 are shown in figures (3.1a), and (3.1b), respectively. The parameters used to solve for disk equations (3.7, 3.9–3.12) are  $a_* = 0$  (Schwarzschild black hole),  $y = 1$ ,  $\ln \Lambda = 15$ ,  $\rho = 0.5$  and  $\sigma^2 = 30$ . The accretion rate is taken to be  $\dot{M}/\dot{M}_E = 0.3$  for 3C 120 (Chatterjee et al., 2009), and 0.2 for GRS 1915+105 (Zdziarski et al., 2016). The black hole mass is taken to be  $M_8 = 0.55$  for 3C 120 (Peterson et al., 2004), and  $M_8 = 1.24 \times 10^{-7}$  for GRS 1915+105 (Reid et al., 2014). The black solid lines show  $10\alpha_{\text{hyb}}$ , while the magenta dashed lines represent  $H/R$ . The green dotted lines show the proton temperatures in units of  $10^{12}K$ , while the electron temperatures in units of  $10^{10}K$  are represented by blue dashed-dot lines. The proton number densities are depicted by red dashed-dot-dot lines, in units of  $10^{10} \text{cm}^{-3}$  for 3C 120, and in units of  $10^{17} \text{cm}^{-3}$  for GRS 1915+105. Figure (3.2) depicts the self-consistency constraints discussed in § 3.2.3. The green solid lines show  $10^{-3}\lambda_{ii}/H$ , while the dashed blue lines represent  $10\lambda/H$ . The quantity  $10\lambda/R$  is shown by the red dotted lines. This shows that the mean free path for collisions between the protons exceeds the disk height, rendering the plasma collisionless, and two-temperature (as evident from the figure (3.1) with proton temperatures  $T_i \approx 10^{11}$  K and electron temperatures  $T_e \approx 10^9$  K) for 3C 120 as well as GRS 1915+105. It can be noted that none of the quantities depend upon the black hole mass, except for the proton number density ( $N_i$ ).

Although our fiducial models assume a non-rotating black hole, some studies (e.g., Blum et al., 2009; Miller et al., 2013) suggest that the source GRS 1915+105 is thought to harbor a rotating black hole at its center. Hence it is worth examining the variation of disk solutions for this source with the black hole spin parameter

$a_*$ . This is depicted in the figure (3.3), where the quantities  $\alpha_{\text{hyb}}$ ,  $H/R$ , the proton and electron temperatures, and the density are plotted as a function of the black hole spin  $a_*$ . These quantities are evaluated at a radius of  $15 R_g$ . The linestyles are identical to those used in Figure (3.1b). We note that  $H/R$  and  $\alpha_{\text{hyb}}$  are very insensitive to  $a_*$ . When  $a_*$  is increased from 0 to 0.98, the proton temperature increases by a factor  $\approx 2$ , while the electron temperature decreases by  $\approx 20\%$ . We will investigate the dependence of the infall timescale on  $a_*$  later on in this chapter.

### 3.3 Inner Disk Collapse Timescale and Connection With X-ray Timescales

As mentioned earlier, our aim in this work is to compute the hybrid viscosity operative in the hot inner accretion disk, and to compare the viscous timescales arising out of our viscosity prescription with the observed X-ray timescales (X-ray dip timescale in sources 3C 120 and 3C 111, and rise times in the X-ray bursts of GRS 1915+105). Having prescribed the viscosity in Eqs. (3.6), and (3.7), we can now calculate the radial infall timescale in the hot accretion disk as

$$t_{\text{infall}} \equiv \frac{R}{v_R} = \frac{R^2}{\nu}, \quad (3.13)$$

where  $v_R$  is the radial infall velocity (which depends upon the operative viscosity),  $\nu$  ( $\text{cm}^2\text{s}^{-1}$ )  $\equiv \eta/Nm = \alpha c_s H$  is the kinematic viscosity and  $c_s$  is the sound speed. Using the disk model of § 3.2.2, the expression for the infall timescale becomes

$$t_{\text{infall}} = 492.5 \left( \frac{\dot{M}}{\dot{M}_E} \right)^{-1} M_8 f_1^{1/2} f_2^{-1} \tau_{\text{es}} R_*^2 \quad (3.14)$$

It is to be noted that Eq (3.14) represents the infall timescale in the hot inner accretion disk and not in the cold, outer disk. It is evident from Eq. (3.14) that the timescale increases with radius. In comparing with the observed X-ray timescales, we use the infall timescale evaluated at the outer edge ( $R_{\text{out}}$ ) of the hot, inner disk, and assume that this is the timescale over which the inner disk collapses.

The number distributions of observed X-ray dip timescales in 3C 120 (Chatterjee et al., 2009), and 3C 111 (Chatterjee et al., 2011) are shown in figures (3.4a), and (3.4b), respectively. We note that the dip durations in 3C 120 range from 5–120 days, with most of them in the range 5–75 days. Similarly, X-ray dip timescales for 3C 111 range from 73–402 days. On the other hand, the galactic microquasar GRS 1915+105 showed some episodes of X-ray bursts as reported by Belloni et al. (1997), and Yadav et al. (1999), with rise times ranging from 1–6 seconds. These

observations show the hard X-ray spectrum in the quiescent (i.e., low intensity) states, whereas during the burst (i.e., high intensity) states, it becomes soft. Since hard X-rays are generally understood to be emerging from the hot, inner disk, these observations suggest that the inner accretion disk collapses over the rise time of the burst. [Yadav et al. \(1999\)](#) also presents a similar idea, in that they compare the rise timescale with the viscous timescale of the Comptonized, sub-Keplerian halo ( $t_{\text{vis}}^{\text{h}}$ ). Our motivation in calculating the infall timescale of the hot inner disk (Eq. 3.14) is similar, with one crucial difference - instead of assuming a value for the Shakura-Sunyaev  $\alpha$  parameter, it is self-consistently calculated using the viscosity mechanism outlined in § 3.2.1.

Our aim in this work is to compute the infall timescale given by Eq. (3.14) and compare it with the observed X-ray dip timescales in 3C 120 and 3C 111 and the fast rise timescales in the X-ray bursting state for GRS 1915+105. In all our calculations, we have assumed a non-rotating black hole; this determines the relativistic correction functions  $f_1$ ,  $f_2$  and  $f_3$  used in the disk structure equations. We have taken the value of Compton  $y$  parameter to be unity and  $\ln \Lambda = 15$ . The black hole mass for 3C 120 is taken to be  $M_8 = 0.55$  ([Peterson et al., 2004](#)),  $M_8 = 1.8$  for 3C 111 ([Chatterjee et al., 2011](#)), and  $M_8 = 1.24 \times 10^{-7}$  for GRS 1915+105 ([Reid et al., 2014](#)). The parameters  $a_{\perp}$ ,  $N_{\perp}$ ,  $N_{\parallel}$ ,  $\rho_{\parallel}$ , and  $\gamma$  appeared in Eq. (3.2) correspond to the turbulence under consideration, and their values are given in Table 1 of [Candia and Roulet \(2004\)](#) for different kinds of turbulence. For the sake of concreteness, we use the values corresponding to Kolmogorov turbulence. We also used the other turbulence models (i.e. Kraichnan and Bykov–Toptygin) and found that our results are quite insensitive to the specific turbulence model used. The accretion rates are taken to be  $\dot{M}/\dot{M}_E = 0.3$  for 3C 120 ([Chatterjee et al., 2009](#)),  $\dot{M}/\dot{M}_E = 0.02 \pm 0.01$  for 3C 111 ([Chatterjee et al., 2011](#)), and  $\dot{M}/\dot{M}_E = 0.2$  for GRS 1915+105 ([Zdziarski et al., 2016](#)). Then we are left with the free parameters  $\rho$  and  $\sigma^2$ , which characterize the turbulence (§ 3.2.1) and  $R_{\text{out}}$ , which gives the extent of the hot, inner accretion disk. We will determine the parameter space (spanned by  $\rho$ ,  $\sigma^2$  and  $R_{\text{out}}$ ) that yield  $t_{\text{infall}}$  that match the observed ones.

## 3.4 Results

### 3.4.1 Model parameters

Having discussed the disk models in § 3.2.3, our main objective is to identify the combinations of free parameters that yield models with infall timescales that match the observed X-ray dip timescales. We run a grid of models with various combinations of the free parameters; the turbulence level ( $\sigma^2$ ), the rigidity ( $\rho$ ) and the

outer radius of the corona ( $R_{\text{out}}$ ). Each of the models is required to satisfy the self-consistency conditions listed in § 3.2.3.

As mentioned earlier, the X-ray dip timescales for 3C 120 range from 5 to 120 days. Figure (3.5a) depicts the combination of parameters that yield  $t_{\text{infall}} = 5$  days while figure (3.5b) shows the parameter combinations for  $t_{\text{infall}} = 120$  days. Combining together, these plots reveal that the range of X-ray dip timescales for 3C 120 can be attained with our model for  $0.2 \lesssim \rho < 1$ ,  $1 \lesssim \sigma^2 \lesssim 30$  (which corresponds to  $0.04 < \alpha_{\text{hyb}} < 0.07$ ) and  $14R_g \lesssim R_{\text{out}} \lesssim 175R_g$ . The range of parameters that yield  $t_{\text{infall}}$  ranging from 146 to 402 days for 3C 111 is shown in figure (3.6). It reveals that  $146 < t_{\text{infall}} < 402$  days can be attained for 3C 111 with  $0.2 \lesssim \rho < 1$ ,  $1 \lesssim \sigma^2 \lesssim 40$  (which corresponds to  $0.02 < \alpha_{\text{hyb}} < 0.08$ ) and  $13R_g \lesssim R_{\text{out}} \lesssim 38R_g$ . Figure (3.7) is a similar plot which depicts the range of parameters that result in values of  $t_{\text{infall}}$  ranging from 1 to 6 seconds for the galactic microquasar GRS 1915+105. We see that the parameter range  $0.2 \lesssim \rho < 1$ ,  $1 \lesssim \sigma^2 \lesssim 25$  (which corresponds to  $0.03 < \alpha_{\text{hyb}} < 0.07$ ) and  $75R_g \lesssim R_{\text{out}} \lesssim 250R_g$  is acceptable in this case.

Figure (3.8) explores the parameter space with  $R_{\text{out}}$  held constant. We find that the infall timescale  $t_{\text{infall}}$  decreases with increasing  $\rho$ , while it increases with increasing  $\sigma^2$ . For 3C 120, we find that  $t_{\text{infall}} \approx 39\text{--}54$  days with  $R_{\text{out}}$  held constant at  $90 R_g$ . Similarly for 3C 111, the range for  $t_{\text{infall}}$  with  $R_{\text{out}} = 30 R_g$  is  $\approx 263\text{--}378$  days.

### 3.4.2 Sensitivity of $t_{\text{infall}}$ to model parameters

It is clear from the figures (3.5)–(3.8) that the observed X-ray timescales for each source studied here can be explained with a reasonable parameter range in our model. The next obvious question to examine is to check how sensitive our results are to the parameters used, i.e., how much change do the results undergo if we change the parameters. To reiterate, the magnetic rigidity is represented by the quantity  $\rho \equiv r_L/H$ , and is a measure of how “tightly tied” the protons are to the mean magnetic field, and quantifies the extent to which the protons are magnetized. A low value for  $\rho$  would indicate that the protons are strongly magnetized, while a high value (the upper limit being 1) would indicate the opposite. The quantity  $\sigma^2 \equiv \langle B_r^2 \rangle / \langle B_0^2 \rangle$  is the ratio of the energy density of the turbulent magnetic fluctuations to that of the ordered magnetic field, and can be regarded as a measure of the strength of the turbulence. The quantity  $R_{\text{out}}$  denotes the outer radius of the hot, inner accretion disk. In order to examine the sensitivity of the result for  $t_{\text{infall}}$ , we vary the parameters one at a time (while holding the rest of them fixed). The results of such a sensitivity analysis for 3C 120 are shown in table (3.1) and figure

Table 3.1: Sensitivity analysis of parameters: fiducial model for 3C 120

Parameter	% change in reference	% change in $t_{\text{infall}}$
$\rho$ ( $\rho_{\text{ref}} = 0.5, \sigma^2 = 10,$ $R_{\text{out}} = 90 R_g$ )	+10 -10	-0.1 +0.1
$\sigma^2$ ( $\sigma_{\text{ref}}^2 = 10, \rho = 0.5,$ $R_{\text{out}} = 90 R_g$ )	+10 -10	+0.5 -0.5
$R_{\text{out}}$ ( $R_{\text{out,ref}} = 90 R_g,$ $\rho = 0.5, \sigma^2 = 10$ )	+10 -10	+15 -15

(3.9). These results are applicable to the other two sources as well. The reference values of parameters for this study are:  $\rho_{\text{ref}} = 0.5$ ,  $\sigma_{\text{ref}}^2 = 10$ ,  $R_{\text{out,ref}} = 90 R_g$ . It is evident from figure (3.9) that  $t_{\text{infall}}$  is a monotonically decreasing function of  $\rho$ , while it increases monotonically with  $\sigma^2$  and  $R_{\text{out}}$ . In each row of table (3.1), the parameter shown in red is varied while the rest are held fixed. This table shows that the values for  $t_{\text{infall}}$  are least sensitive to variations in  $\rho$  and most sensitive to variations in  $R_{\text{out}}$ . Varying  $R_{\text{out}}$  by  $\pm 10\%$  results in a  $\approx \pm 15\%$  variation in  $t_{\text{infall}}$ . By contrast, varying  $\rho$  by  $\pm 10\%$  results in only a  $\mp 0.1\%$  change in  $t_{\text{infall}}$ , and a change of  $\pm 10\%$  in  $\sigma^2$  yields a  $\pm 0.5\%$  change in  $t_{\text{infall}}$ . As mentioned earlier, our fiducial model for GRS 1915+105 assumes a non-rotating black hole, while there is some evidence that it harbors a rotating black hole. In our fiducial model for GRS 1915+105, we find that increasing the black hole spin parameter  $a_*$  from 0 to 0.98 necessitates a 12% increase in  $R_{\text{out}}$  in order to yield an infall timescale  $t_{\text{infall}} = 1$  second. Conversely, if  $R_{\text{out}}$  is kept fixed at  $75 R_g$ , increasing  $a_*$  from 0 to 0.98 results in a 17% decrease in  $t_{\text{infall}}$ .

### 3.5 Summary and Conclusions

To recapitulate, X-ray dips in AGN systems such as 3C 120 and 3C 111, and the rise time of the bursts in X-ray intensity in galactic microquasar GRS 1915+105 are thought to arise from the collapse of the inner accretion disk, which occurs over the radial infall timescale (Eq. 3.14). X-ray dip timescales for 3C 120 are in the range 5–120 days with most dips happening over 5–75 days. The dip timescales for 3C 111 are in the range 73–402 days. In the galactic microquasar GRS 1915+105, the rise time of X-ray bursts (which can be thought of as the dip timescale for hard X-ray intensity) is  $\approx 1$ –6 seconds. The radial infall timescale of the hot inner accretion disk is crucially governed by the operative viscosity, which is commonly parametrized via

the Shakura-Sunyaev  $\alpha$  parameter ( $\nu = \alpha c_s H$ ). Authors have been treating  $\alpha$  as a fitting parameter without worrying about the microphysical viscosity mechanism operative in the disk. Hence, except for the constraint  $0 < \alpha < 1$ , not much is known about it. In this work, we have addressed this issue by formulating the prescription for viscosity operative in the hot, inner regions of the accretion disks, based on the microphysical mechanisms. The plasma in these regions is so hot that the protons are collisionless; they rarely collide with each other, but they can be scattered via interactions with scattering centers (or kinks) in turbulent magnetic fields. There is considerable literature in which estimates of the diffusion coefficient has been derived from detailed simulations of cosmic ray protons diffusing across a large-scale magnetic field in the presence of turbulence. The mean free path extracted from this diffusion coefficient is used to compute the operative viscosity, which we term the “hybrid” viscosity (since it is neither due to proton-proton collisions nor due to magnetic field stresses, but due to protons bouncing off magnetic scattering centres). This approach is similar to that used to construct a cosmic ray viscosity by [Earl, Jokipii, and Morfill \(1988\)](#). Computing the hybrid viscosity enables us to construct accretion disk models (which incorporate a physically motivated viscosity) and calculate the collapse timescale for the inner disk.

Our results have three free parameters: the ratio of energy density in the turbulent magnetic field to that in the large-scale magnetic field (the turbulence level  $\sigma^2$ ), the ratio of the proton Larmor radius to the disk height (the magnetic rigidity  $\rho$ ) and the outer radius of the hot, inner accretion disk–corona  $R_{\text{out}}$ . Different combinations of these parameters yield radial infall timescales (Eq. 3.14) that can match the ones observed for 3C 120, 3C 111, and GRS 1915+105. The space spanned by these parameters is depicted in figures (3.5)–(3.7), and gives a comprehensive idea of the scope of our model. Different points in these figures represent different accretion disk models such as the one shown in figure (3.1). We go on further and check the sensitivity of our results to the change in parameters. We find that the infall timescale  $t_{\text{infall}}$  is not very sensitive to variations in the parameters  $\rho$  and  $\sigma^2$ . It is very insensitive to  $\rho$  (a 10% change in  $\rho$  results in only a 0.1% change in  $t_{\text{infall}}$ ) and quite insensitive to  $\sigma^2$  as well (a 10% change in  $\sigma^2$  results in a 0.5% change in  $t_{\text{infall}}$ ). By contrast, a 10% change in the outer radius of the hot inner disk ( $R_{\text{out}}$ ) results in a 15% change in  $t_{\text{infall}}$  - our results are thus most sensitive to  $R_{\text{out}}$ . To summarize,

- The inner accretion disk collapses over the radial infall timescale, which is governed by the operative viscosity. Instead of treating the Shakura-Sunyaev  $\alpha$  parameter to be just a fitting parameter, we have outlined a prescription for the viscosity operative in the hot, inner part of black hole accretion disks and constructed simplified disk models using this prescription. The disk infall

timescales ( $t_{\text{infall}}$ ) obtained with this model are in good agreement with X-ray observations of 3C 120, 3C 111 and GRS 1915+105. Combining this work with the model given by [Shende, Subramanian, and Sachdeva \(2019\)](#) for the launching of episodic blobs from the inner accretion disks, our work here outlines a plausible scenario for episodes of (inner) disk collapse accompanied by blob ejection, which was observed in the above mentioned sources.

- We have found that our results for  $t_{\text{infall}}$  are fairly insensitive to the parameters  $\sigma^2$  and  $\rho$  that are used to compute the coefficient of hybrid viscosity. The values of the Shakura-Sunyaev  $\alpha$  parameter arising from our viscosity prescription range from 0.02 to 0.08.
- The model predictions for the inner disk infall timescale are most sensitive to the disk outer radius  $R_{\text{out}}$ , with larger  $R_{\text{out}}$  yielding larger values for  $t_{\text{infall}}$ . For 3C 120, we find that our models require  $14 \lesssim R_{\text{out}} \lesssim 175 R_g$  to match the observational results for X-ray dip timescales of 5–120 days. For 3C 111, we require  $13 \lesssim R_{\text{out}} \lesssim 38 R_g$  for dip timescales of 73–402 days and for GRS 1915+105 we require  $75 \lesssim R_{\text{out}} \lesssim 250 R_g$  for dip timescales of 1–6 seconds.
- These values of  $R_{\text{out}}$  might seem somewhat large in comparison with the values of  $\approx 20 R_g$  quoted by [Reis and Miller \(2013\)](#) for the size of hot, X-ray emitting coronae. For GRS 1915+105, for instance, we find that  $75 \lesssim R_{\text{out}} \lesssim 250 R_g$ . However, the accretion rates used in [Reis and Miller \(2013\)](#) are around 0.01 times the Eddington value. On the other hand, we use  $\dot{M}/\dot{M}_E = 0.2$  for GRS 1915+102, following [Zdziarski et al. \(2016\)](#). If we were to use  $\dot{M}/\dot{M}_E = 0.02$ , our model requires  $12 \lesssim R_{\text{out}} \lesssim 22 R_g$  for dip timescale of 1 second. We also note that the size of the hot, post-shock region in GRS 1915+102 has been estimated to be 90–132  $R_g$  ([Nandi et al., 2001](#)).

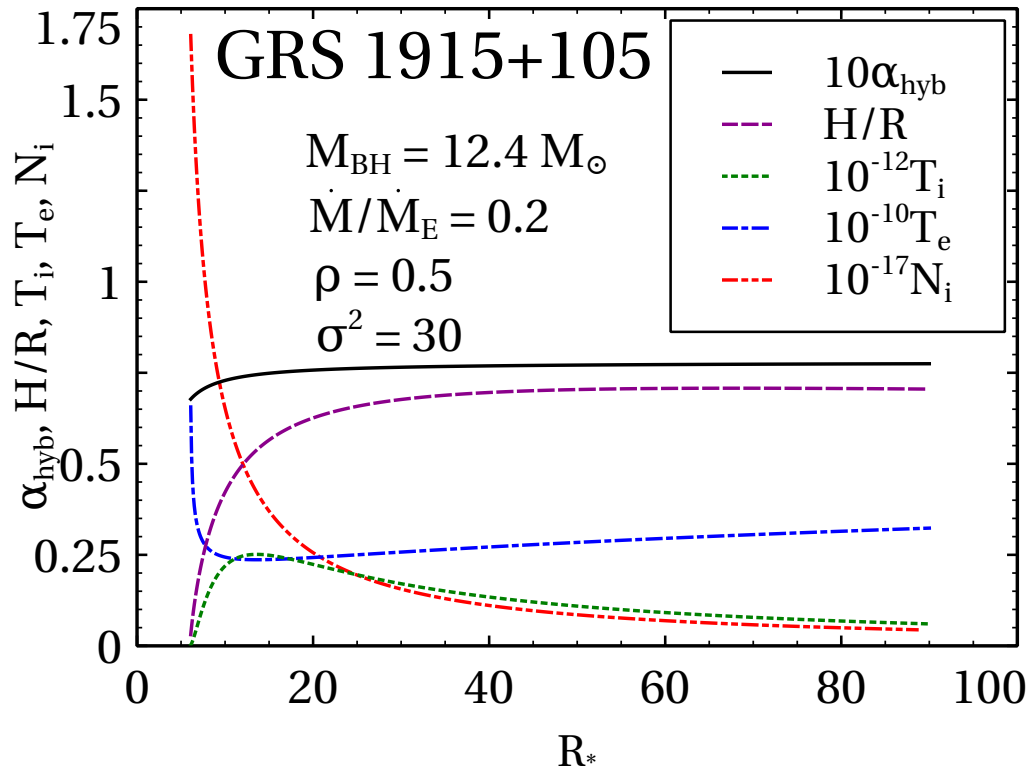
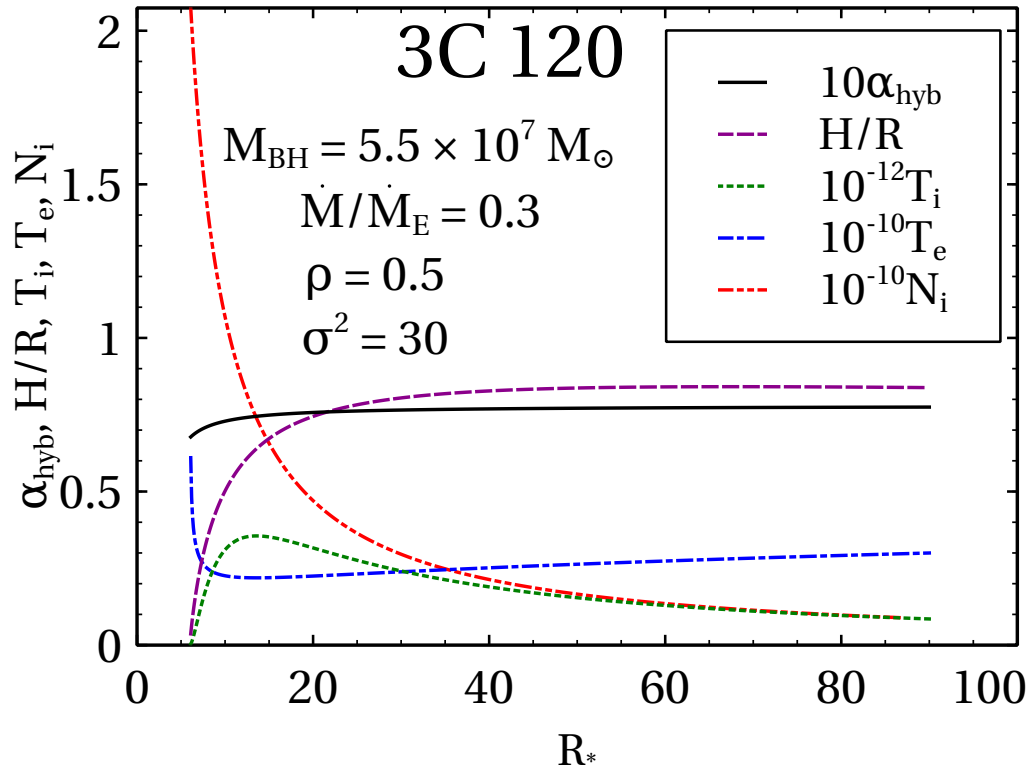


Figure 3.1: Representative accretion disk models for (a) 3C 120 and (b) GRS 1915+105. This figure shows results for  $10\alpha_{\text{hyb}}$ ,  $H/R$ ,  $10^{-12}T_i$ ,  $10^{-10}T_e$  and  $10^{-10}N_i$ , with  $\dot{M}/\dot{M}_E = 0.3$ ,  $\rho = 0.5$  and  $\sigma^2 = 30$ .



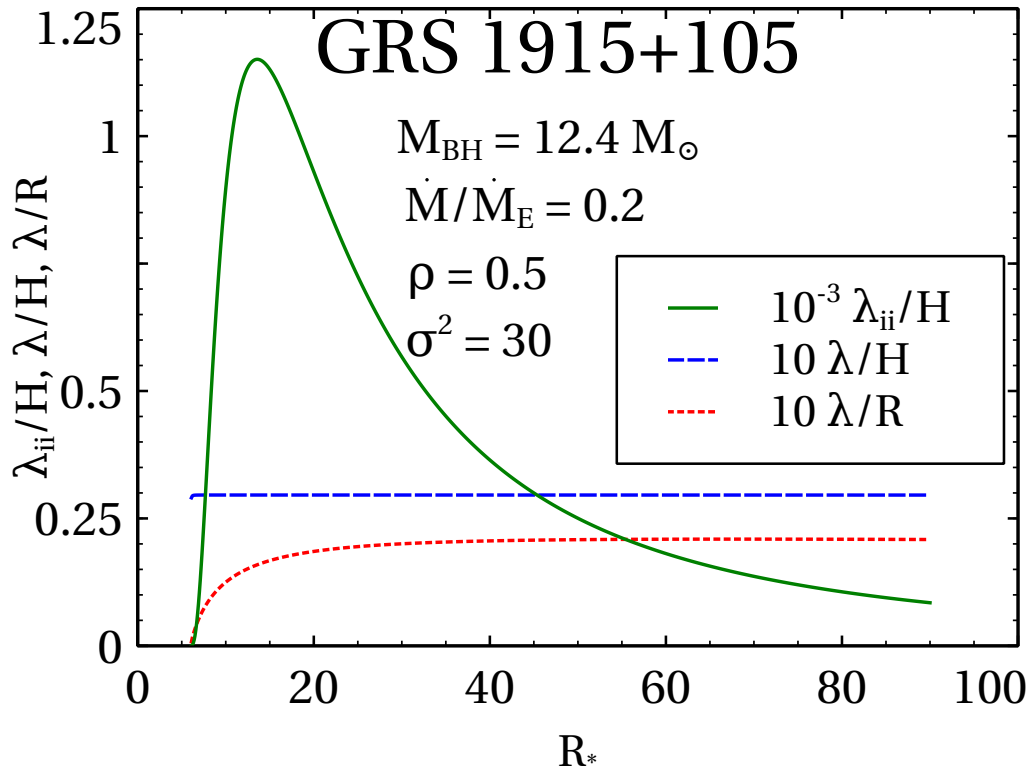
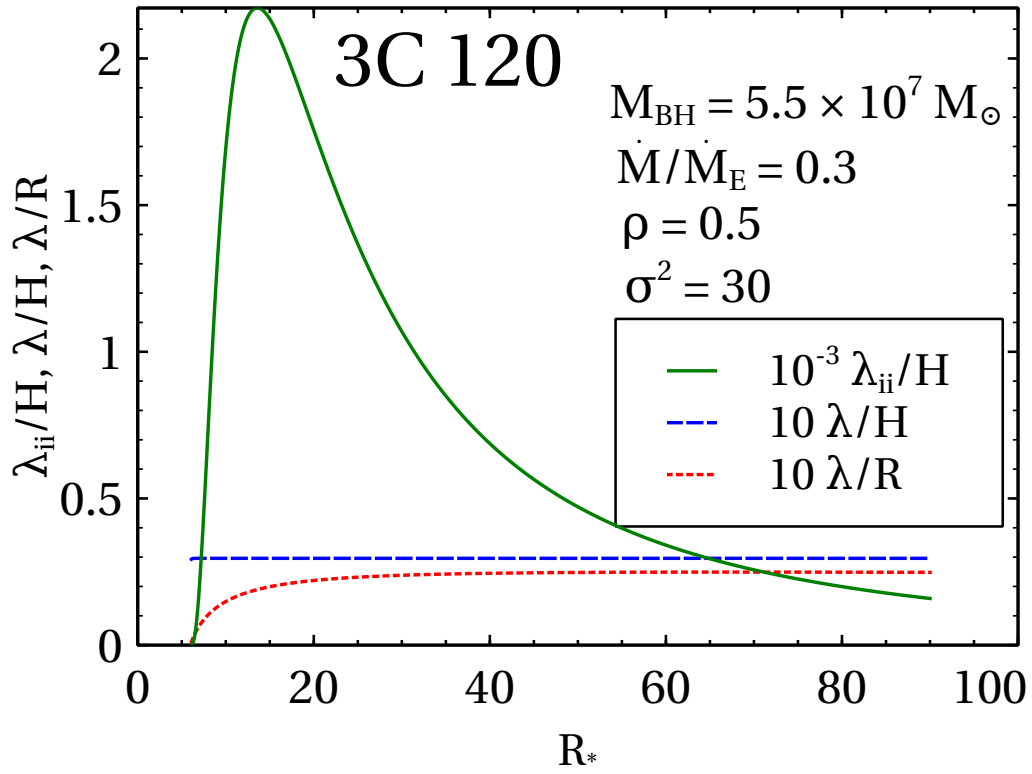


Figure 3.2: Representative accretion disk models for (a) 3C 120 and (b) GRS 1915+105. This figure shows results for  $10^{-3}\lambda_{ii}/H$ ,  $10\lambda/H$  and  $10\lambda/R$ , with  $\dot{M}/\dot{M}_E = 0.3$ ,  $\rho = 0.5$  and  $\sigma^2 = 30$ .

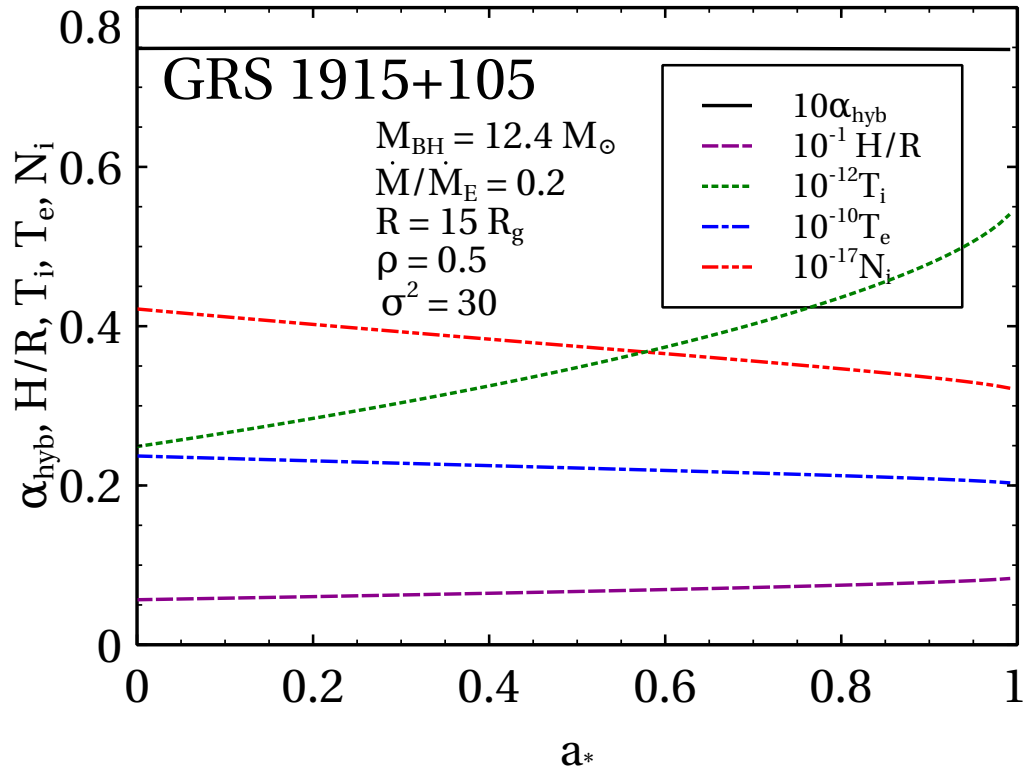
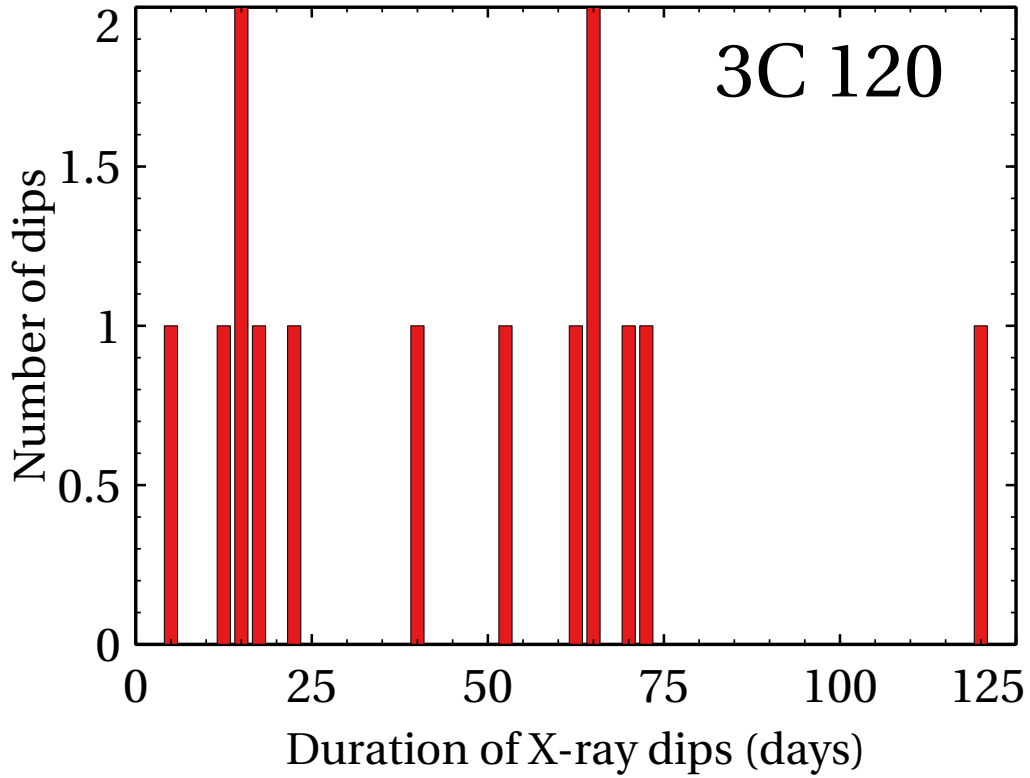
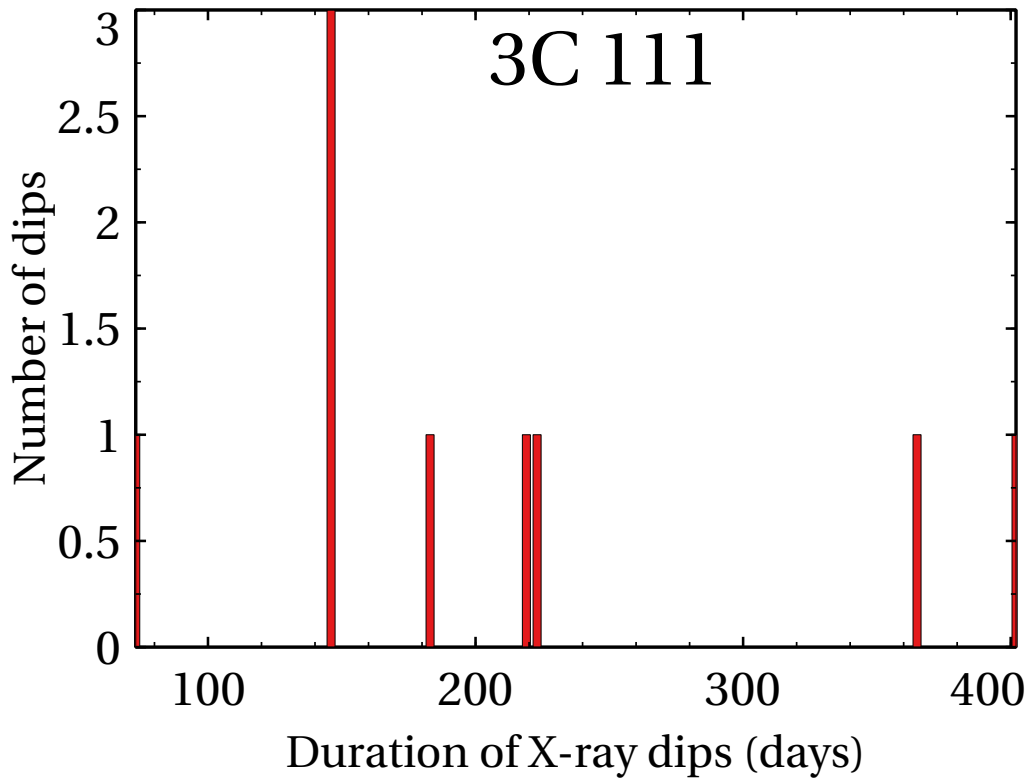


Figure 3.3: This figure shows how the quantities  $10\alpha_{\text{hyb}}$ ,  $10^{-1}H/R$ ,  $10^{-12}T_i$ ,  $10^{-10}T_e$  and  $10^{-17}N_i$  (evaluated at  $R = 15R_g$ ) vary with the black hole spin parameter  $a_*$ . The black hole mass is taken to be representative of GRS 1915+105, the accretion rate is  $\dot{M}/\dot{M}_E = 0.2$  and  $\rho = 0.5$ ,  $\sigma^2 = 30$ .

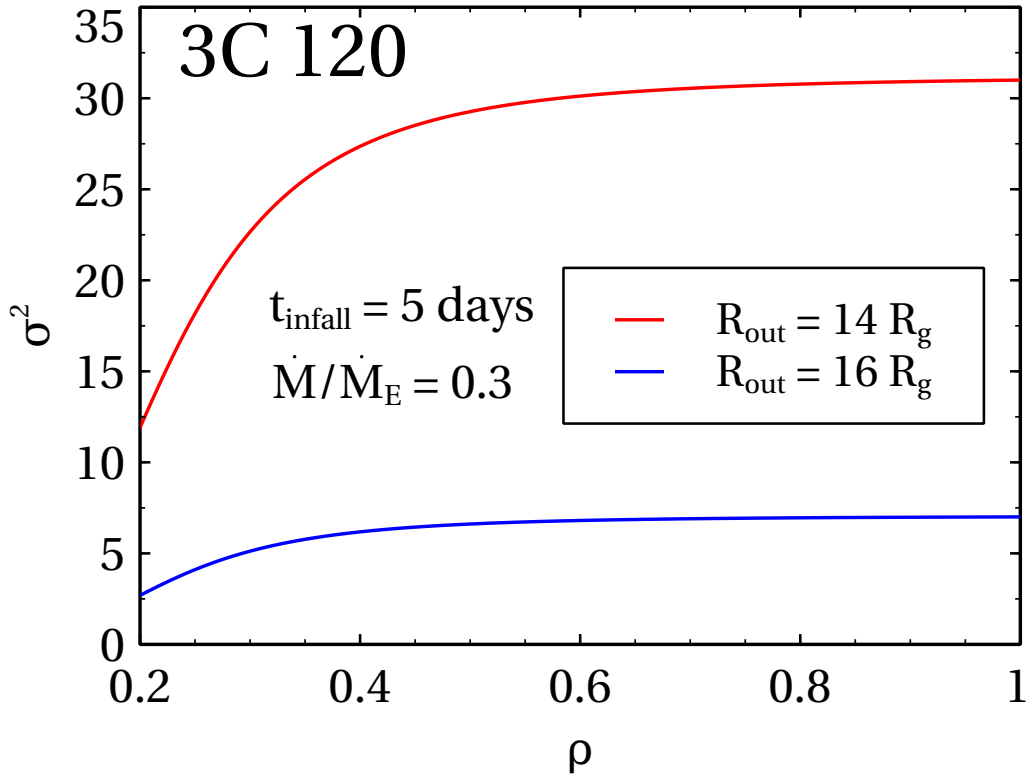


(a)

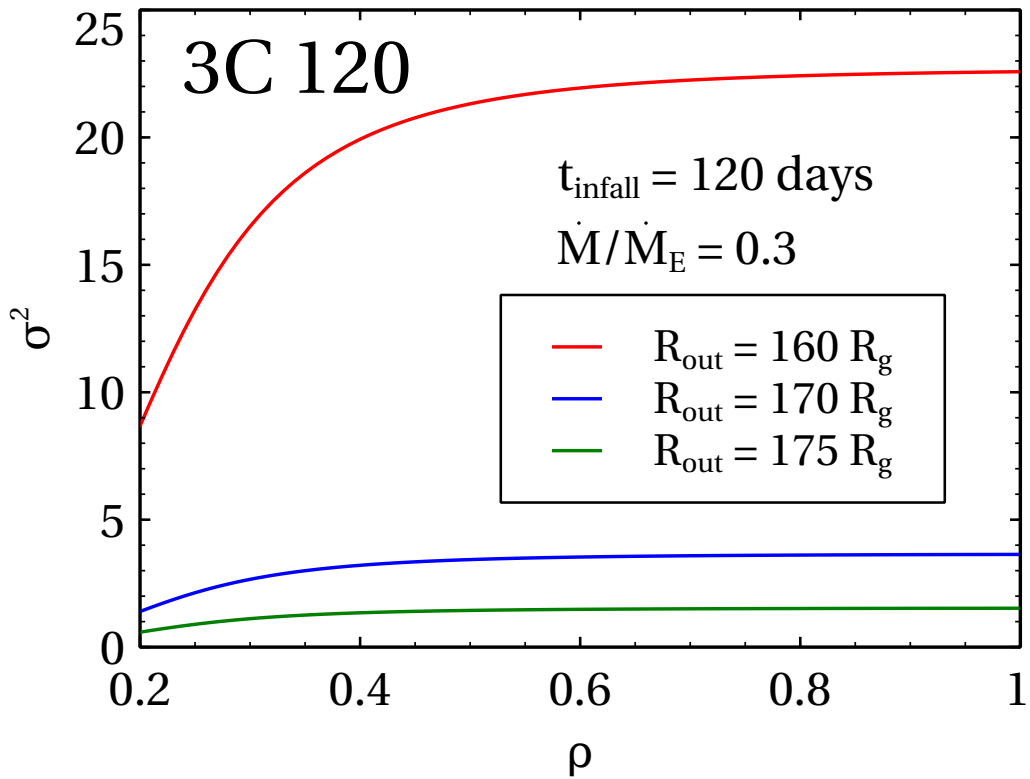


(b)

Figure 3.4: Histograms of the X-ray dip durations observed in (a) 3C 120, and (b) 3C 111

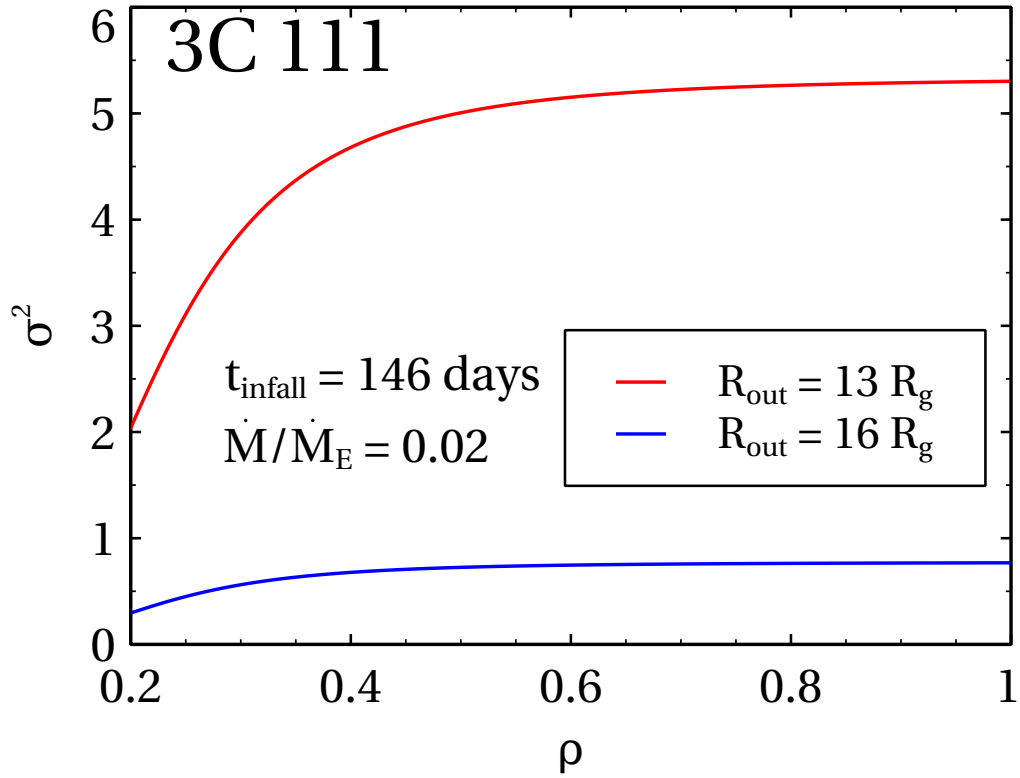


(a)

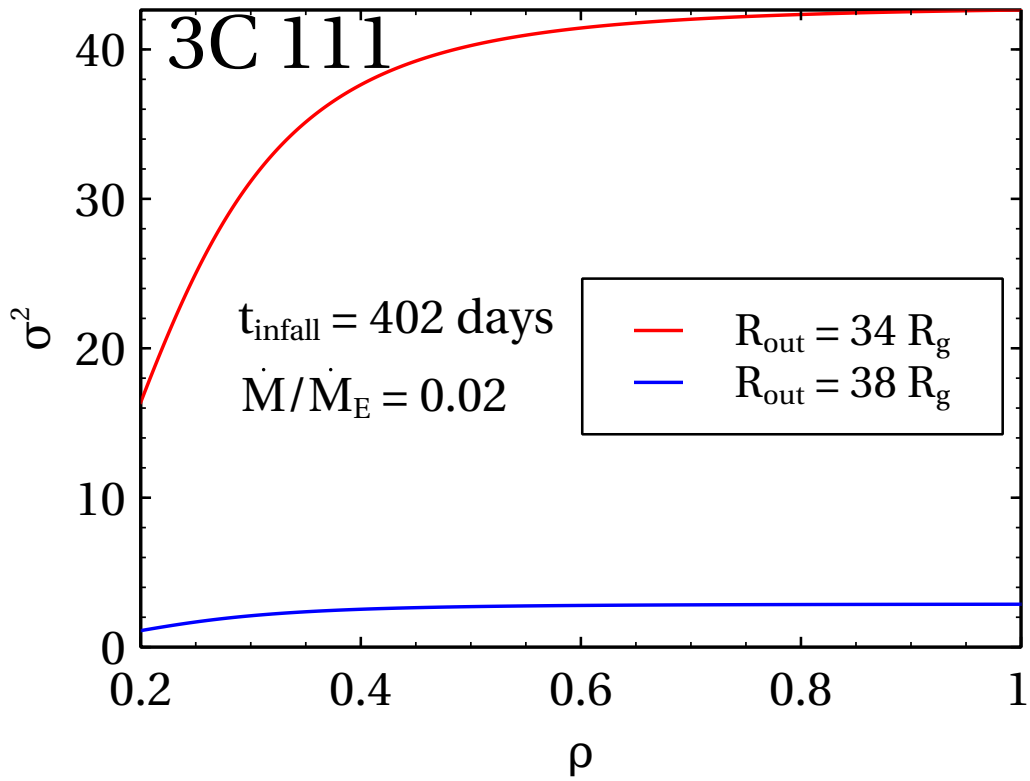


(b)

Figure 3.5: (a) Parameter space corresponding to X-ray dip of 5 days in 3C 120, (b) Parameter space corresponding to X-ray dip of 120 days in 3C 120

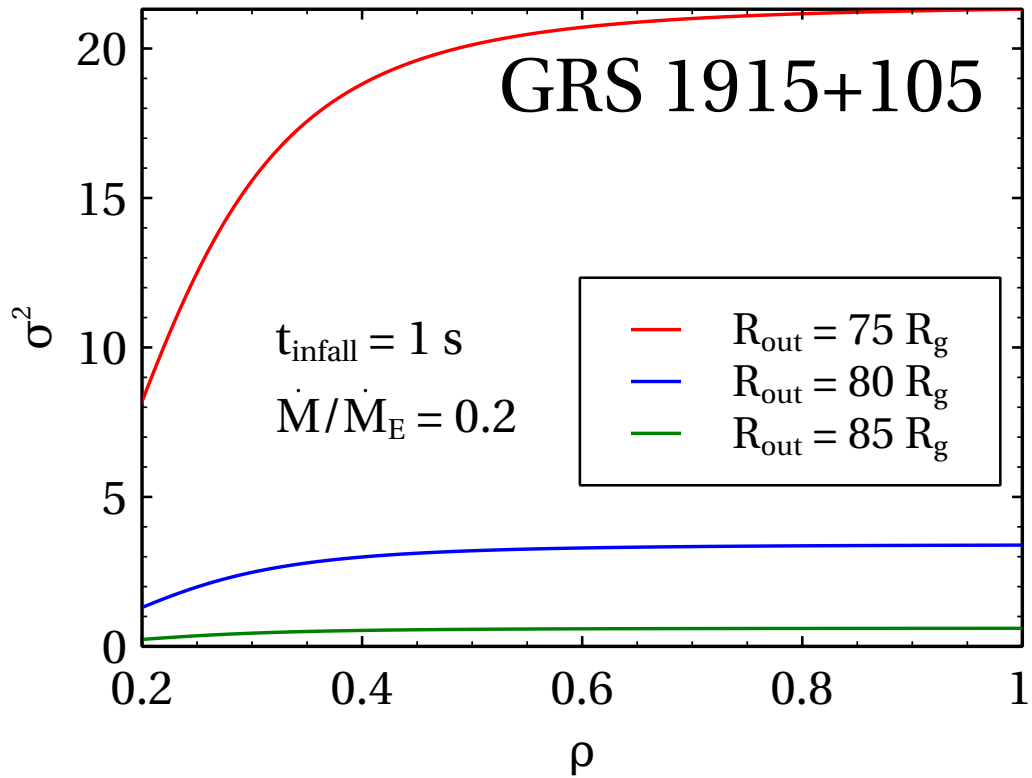


(a)

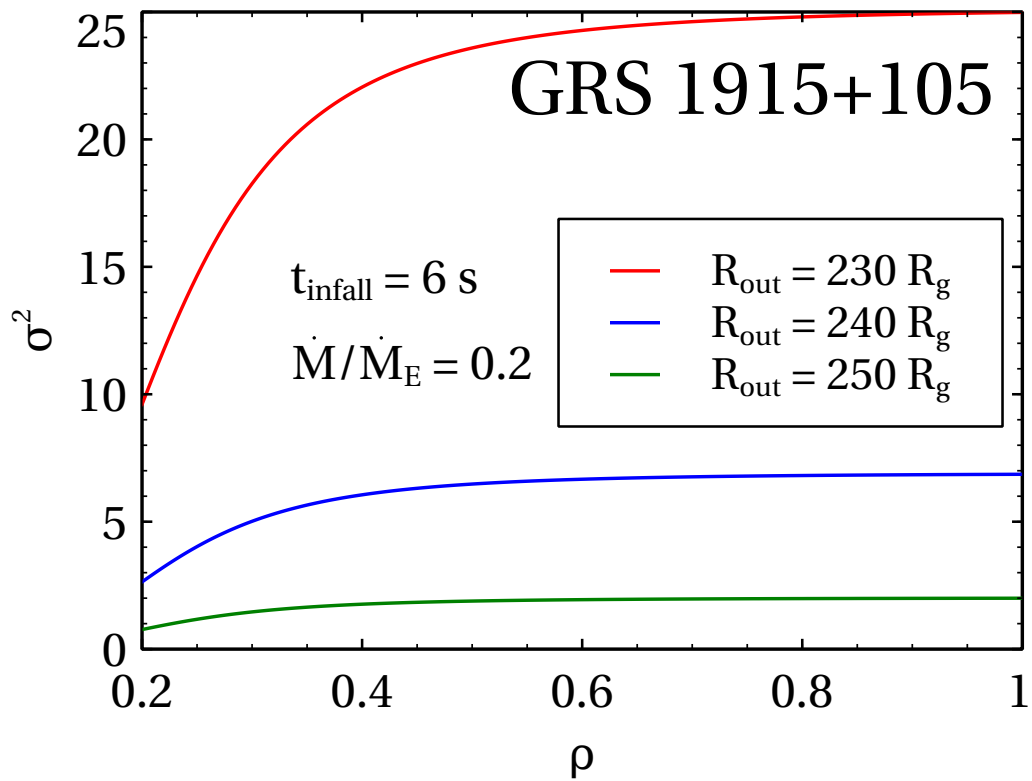


(b)

Figure 3.6: (a) Parameter space corresponding to X-ray dip of 146 days in 3C 111, (b) Parameter space corresponding to X-ray dip of 402 days in 3C 111

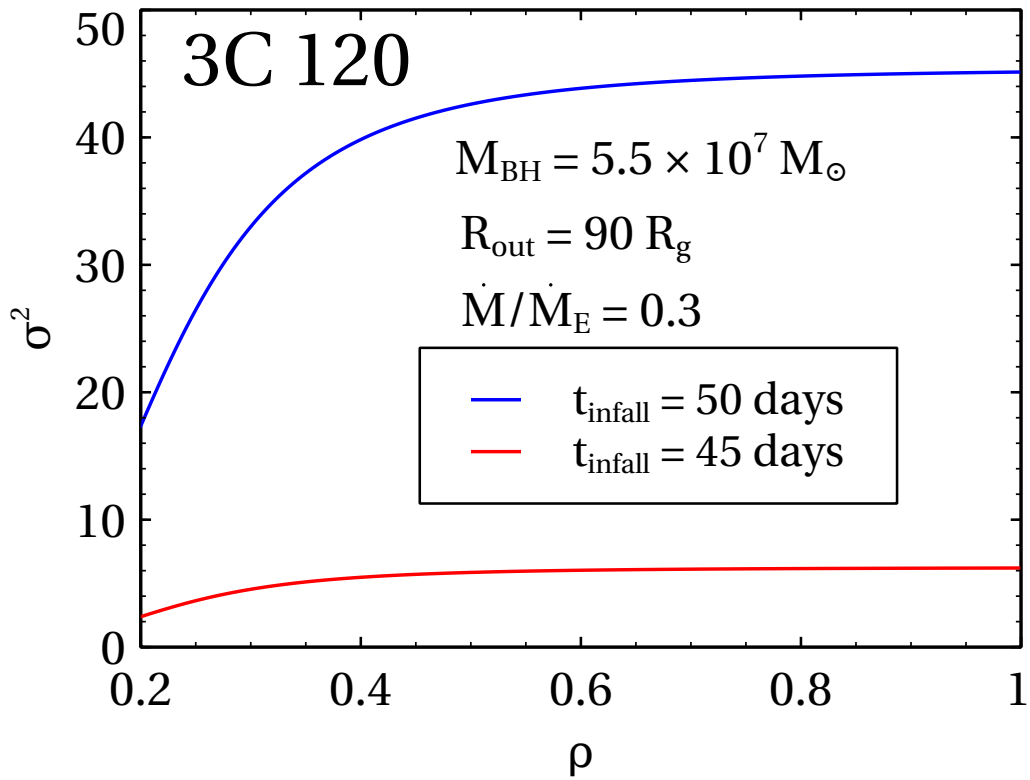


(a)

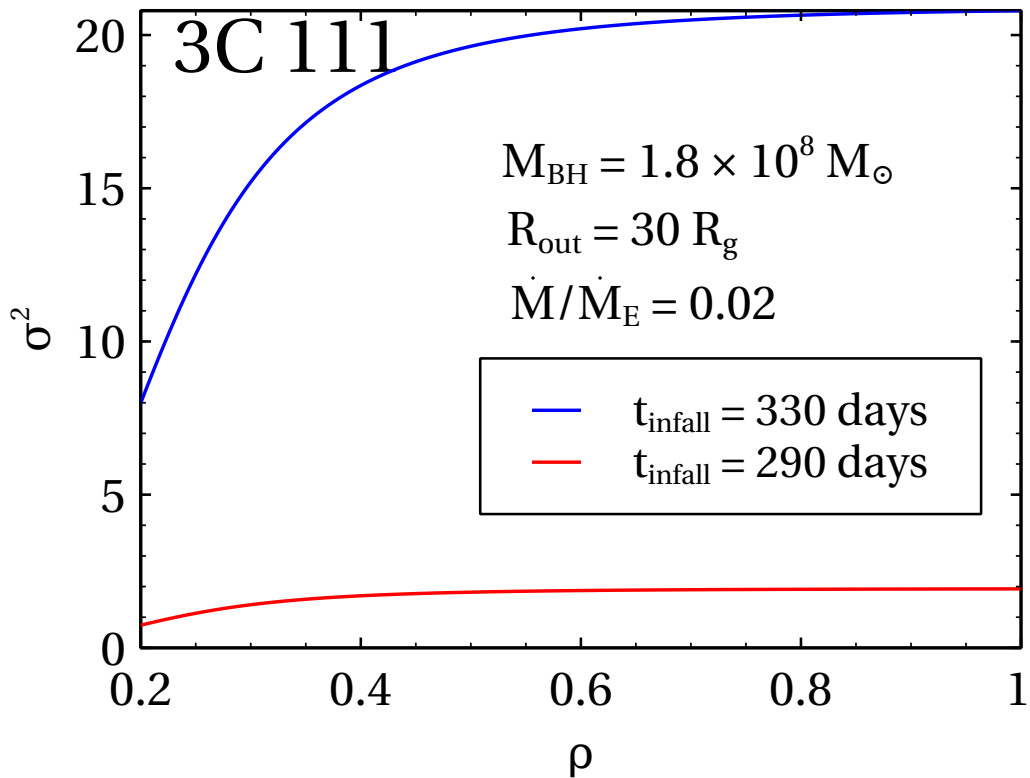


(b)

Figure 3.7: (a) Parameter space corresponding to X-ray dip of 1 s in GRS 1915+105,  
 (b) Parameter space corresponding to X-ray dip of 6 s in GRS 1915+105



(a)



(b)

Figure 3.8: (a) Parameter space corresponding to X-ray dip in the range 45–50 days in 3C 120, (b) Parameter space corresponding to X-ray dip in the range 290–330 days in 3C 111

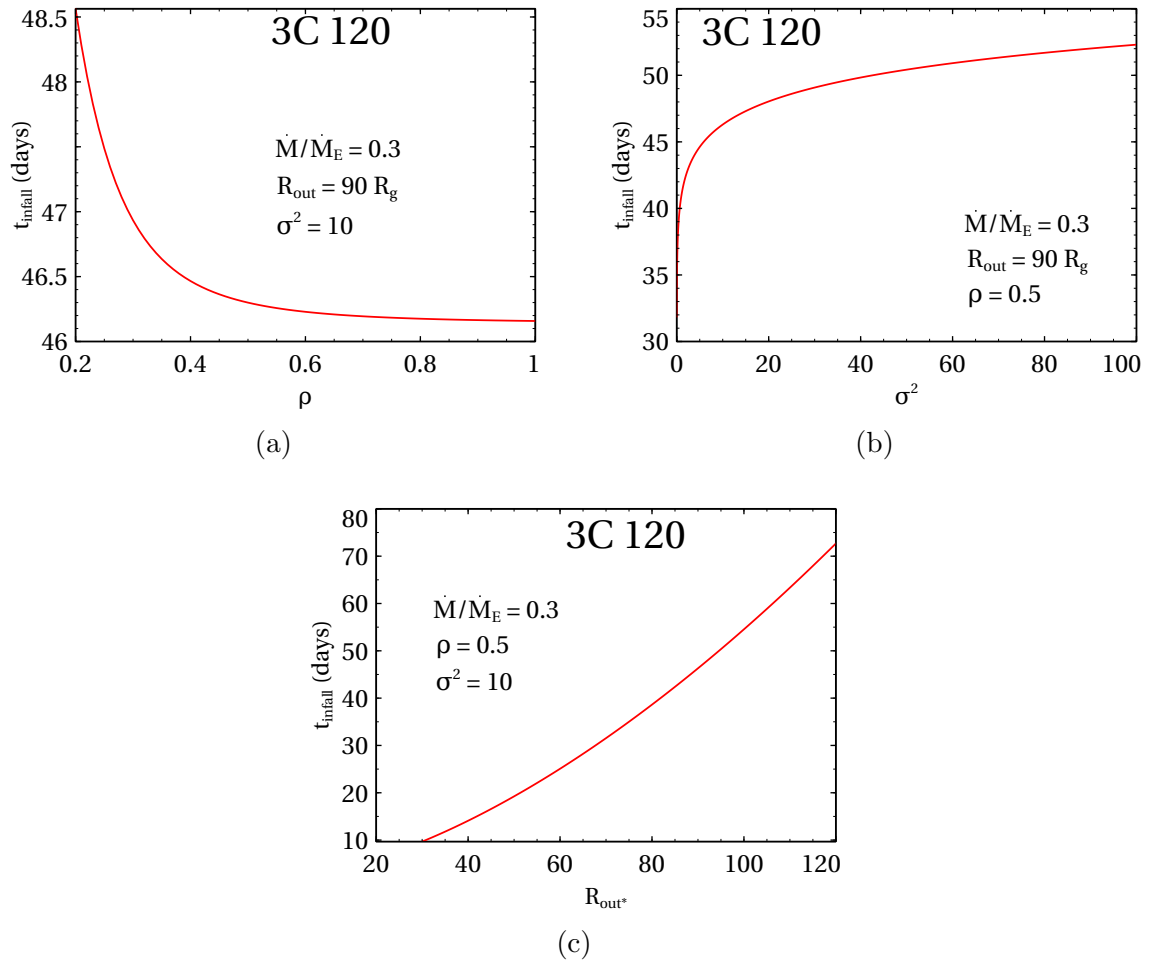


Figure 3.9: A depiction of how  $t_{\text{infall}}$  varies in response to changes in  $\rho$ ,  $\sigma^2$ , and  $R_{\text{out}}$



# Chapter 4

## Relativistic Particle-Dominated Winds From Advection-Dominated Accretion Flows

### 4.1 Introduction

#### 4.1.1 Advection-dominated accretion flows and outflows

The accretion flow becomes advection-dominated when the accreting gas is unable to cool efficiently. The viscous dissipation of energy in the flow is stored as entropy rather than being radiated. This happens when the gas is fed to the central black hole at very low accretion rates (significantly sub-Eddington). As a result, the gas becomes tenuous and optically thin for the Coulomb collisions to occur, and enters into two-temperature regime, with proton temperatures in excess of  $10^{11}$  K, and electron temperatures  $\approx 10^9$  K. Because of the low density in the flow, the efficiency of the emission processes is low, and this limits the luminosity of the flow. Hence, the emission from underluminous black hole candidates can be explained by the models of advection-dominated accretion flows (ADAF) (Ichimaru, 1977; Narayan and Yi, 1994, 1995a,b). The self-similar solutions of ADAF given by Narayan and Yi (1994, 1995a,b) have some inconsistencies, because the gas in ADAF has a positive Bernoulli parameter, and hence, the flow appears to be gravitationally unbound and allows outflows. The explicit treatment of the outflows (wind) is not included in their work self-consistently. The advection-dominated inflow-outflow solutions (ADIOS) modeled by Blandford and Begelman (1999) tried to address this issue by incorporating self-consistently the possibility of winds that carry away mass, energy and angular momentum in such a manner that the Bernoulli parameter

of the gas in the disk is negative, allowing it to accrete. But the ADIOS model uses Newtonian gravitational potential which deviates from the actual potential very close to the black hole. Furthermore, the winds in the ADIOS model are non-relativistic, as opposed to the relativistic winds/jets as observed from AGN. [Becker, Subramanian, and Kazanas \(2001\)](#) (BSK01 from now onwards) proposed a modification to ADIOS, namely relativistic, advection-dominated inflow-outflow solutions (RADIUS), where they incorporated the effects of general relativity by using the pseudo-Newtonian prescription for the gravitational potential ([Paczyński and Wiita, 1980](#)). The results of the RADIUS model show that the winds are relativistic, and originate predominantly from the inner regions of the disk, close to the radius of marginal stability. This is because of the steep gradient in the pseudo-Newtonian potential. Since we are dealing with relativistic winds from the hot accretion flow in this chapter, we will make use of the RADIUS model in order to explain the launching of winds.

#### 4.1.2 Relativistic outflows in the framework of particle acceleration mechanisms in the hot accretion flow

The treatments discussed in § 4.1.1 employ the fluid description of the advection-dominated inflow-outflows. To launch the relativistic outflows successfully from the disk, we have to invoke acceleration mechanism operative in the disk that preferentially accelerates high-energy particles. The result of such a process would be that the particle distribution consists of a thermal component, which is bound to the disk, and a non-thermal component, which is gravitationally unbound and ready to escape in the form of a wind. Some MHD simulations study the production of non-thermal particles, and their stochastic acceleration in the hot accretion flow as a result of magnetic reconnection triggered by the MRI (magnetorotational instability) generated turbulence ([Kimura et al., 2019](#); [Sun and Bai, 2021](#)). On the other hand, [Subramanian, Becker, and Kazanas \(1999\)](#) (SBK99 from now onwards) present a scenario where relativistic outflows are powered by the second-order Fermi-acceleration mechanism governed by the shearing magnetic fields in the accretion disk coroneae. SBK99 show that the monoenergetic injection of protons from the disk results in a power-law distribution of protons in the corona, which eventually escape to form a pressure-driven wind. Such a wind passes through the critical (sonic) point and subsequently transforms into a relativistic jet at large distances from the black hole.

The two descriptions of the relativistic outflows mentioned above, namely, a) the fluid description, and b) particle acceleration mechanism description, have mostly been dealt separately in the literature, and very few make a connection between the

outflow, and the underlying accretion disk. In this work, we try to bridge this gap and connect the two descriptions so as to explain relativistic jets from black hole sources. Following the treatment of SBK99, we derive the distribution function of protons in the hot, advection-dominated flow as a solution to the transport equation in energy space. We then connect it with the RADIOS model given by BSK01, and see how the high-energy tail of the distribution function of protons is ejected in the form of a wind. A pictorial representation of this is shown in the figure (4.1), in which a proton distribution function consists of a thermal part (non-shaded portion of the distribution function), which eventually remains in the disk, and a non-thermal tail (a shaded portion starting from the energy  $E_c$ ), which escapes from the disk to form a wind. We also investigate the behavior of the high-energy tail with the equatorial distance from the black hole.

Our work explicitly deals with “heavy” relativistic winds (electron-proton winds) rather than just Poynting flux (Blandford and Znajek, 1977; Lovelace et al., 1987) or electron-positron winds (Blandford and Payne, 1982; Ustyugova et al., 1999). Gamma-ray flaring observations of blazars at TeV energies require the presence of hadrons in the jet (Sahu et al., 2019; Hoerbe et al., 2020; Gutiérrez et al., 2021). There is ample evidence in which the theoretical treatments of the jet address the origin of hadrons in the jet (e.g., Contopoulos and Kazanas, 1995; SBK99; Le and Becker, 2004, 2005).

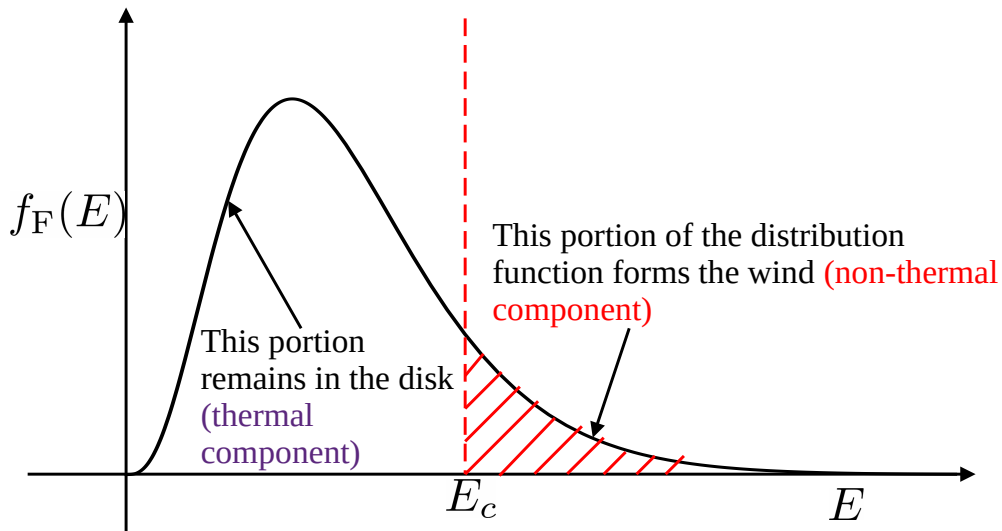


Figure 4.1: Schematic representation of proton distribution function in a hot, advective disk

## 4.2 Model for relativistic outflows

### 4.2.1 Second-order Fermi acceleration in accretion flows

Subramanian, Becker, and Kafatos (1996) showed that magnetic field irregularities embedded in the accretion flow can act as scattering centers for collisions with protons. Since the magnetic fields are tied to the disk via flux freezing, the magnetic scattering centers, or “kinks” in the magnetic fields can be treated as cold (no stochastic motion), with relative shear velocity in accordance with a Keplerian flow ( $\Delta v \sim \Delta v_\phi$ ). With each collision, a proton can either gain or lose energy, depending on whether the collision is approaching one or overtaking one. Hence, to first order in  $\Delta v$ , there is no mean gain, or loss of energy for the incident proton. However, the approaching collisions occur over a shorter timescale than that of the overtaking collisions, resulting into the net acceleration of a proton, to second order in  $\Delta v$ . Hence, the mean fractional energy gain per scattering for protons in the quasi-Keplerian shear flow can be given by

$$\frac{\Delta E}{E} \sim \left( \frac{\Delta v_\phi}{v_{\text{rms}}} \right)^2 = \left( \frac{\tilde{\lambda}_1}{v_{\text{rms}}} \frac{dv_\phi}{dR} \right)^2 \quad (4.1)$$

where  $E$  is the proton energy,  $v_\phi$  is the Keplerian velocity, and rms velocity of protons is denoted by  $v_{\text{rms}} = (3k_B T_i / m_p)^{1/2}$  (where,  $k_B$ ,  $T_i$ , and  $m_p$  represent Boltzmann’s constant, proton temperature, and proton mass, respectively).  $\tilde{\lambda}_1$  is the mean free path for the protons (also known as magnetic coherence length in the disk) colliding with magnetic scattering centers. On the right-hand side of Eq. (4.1), we have used  $\Delta v_\phi \equiv \tilde{\lambda}_1 dv_\phi / dR$  as the characteristic relative shear velocity between successive scattering centers.

### 4.2.2 Particle distribution in the hot, inner accretion flow

Fermi acceleration is governed by the collisions of thermal protons with the magnetic scattering centers, or “kinks” in the magnetic fields whose motion is driven by the quasi-Keplerian shear flow. Due to these collisions, the energy distribution of protons in the hot accretion flow is governed by the following transport equation (Eq. 3.3 of SBK99) in energy space:

$$\frac{\partial f_G}{\partial t} = \frac{1}{E^2} \frac{\partial}{\partial E} \left( E^2 \mathcal{D} \frac{\partial f_G}{\partial E} \right) + \frac{\dot{N}_1 \delta(E - E_i)}{E_i^2} - \frac{f_G}{t_1} \quad (4.2)$$

Eq. (4.2) represents the time evolution of a Green’s function  $f_G$  in this process, where the first term on the right-hand side represents the diffusion of protons in energy space, and  $\mathcal{D}$  the diffusion coefficient in the energy space. The second term

is the source term, describing the injection of monoenergetic protons with energy  $E_i$  at a rate per unit volume equal to  $\dot{N}_1$  into the acceleration region, which, in this case is the hot accretion disk. The third term in Eq. (4.2) denotes the escape term, wherein  $t_1$  represents the mean time the protons spend in the hot flow, before escaping into the wind.

The specific form of  $\mathcal{D}$  as a function of energy  $E$  depends on the spectrum of turbulence that gives rise to the magnetic irregularities that accelerate the protons. Following the prescription of SBK99, we adopt the form of the diffusion coefficient  $\mathcal{D}$  to have the squared dependence on the energy,

$$\mathcal{D} = D_1 E^2 \quad (4.3)$$

where  $D_1$  is a constant with the units of inverse time.

The mean energization rate due to shear acceleration of protons with energy  $E$  can be written as (SBK99)

$$\langle \dot{E}_{\text{shear}} \rangle = \frac{1}{E^2} \frac{d}{dE} (E^2 \mathcal{D}) = 4ED_1 \quad (4.4)$$

which is typical of a Fermi process. Another expression for the acceleration rate can be obtained from the Eq. (4.1), and written as

$$\frac{\Delta E}{\Delta t} \sim E \left( \frac{\tilde{\lambda}_1}{v_{\text{rms}}} \right) \left( \frac{dv_\phi}{dR} \right) \quad (4.5)$$

where  $\Delta t = \tilde{\lambda}_1/v_{\text{rms}}$  is the mean free time for collisions between protons and magnetic scattering centers. Equating the energization rates given by Eqs. (4.4), and (4.5), we get

$$D_1 \sim \left( \frac{\tilde{\lambda}_1}{v_{\text{rms}}} \right) \left( \frac{dv_\phi}{dR} \right)^2 \quad (\text{s}^{-1}) \quad (4.6)$$

establishing the nature of the diffusion coefficient of Fermi accelerated protons in energy space.

Before solving Eq. (4.2) for the proton energy distribution in the hot accretion disk, it is interesting to calculate the mean energy of protons in the disk based on the nature of operative Fermi acceleration mechanism. For that, consider a proton which is injected into the acceleration region (advective disk, in this case) with energy  $E_i$ , at time  $t = 0$ . Then mean energy of that proton can be obtained by solving the Eq. (4.4), giving

$$\bar{E}(t) = E_i e^{4D_1 t} \quad (4.7)$$

It is clear from the Eq. (4.7) that, in the absence of losses, the proton gains energy without bound until it escapes from the disk. Suppose, on an average, the proton

spends  $t_1$  amount of time in the acceleration region (the disk), and then escapes into the wind, the mean energy of the proton during its residence in the disk can be calculated as

$$\langle E \rangle = \int_0^\infty \bar{E}(t) e^{-t/t_1} \frac{dt}{t_1} \quad (4.8)$$

where  $e^{-t/t_1}$  represents the probability that the proton will remain in the disk until time  $t_1$ , and then escapes subsequently during the interval  $dt$ . Using Eq. (4.7) in Eq. (4.8), the mean proton energy in the disk takes the form

$$\langle E \rangle = \frac{E_i}{1 - 4D_1 t_1} = \frac{E_i}{1 - y} \quad (4.9)$$

where the  $y$ -parameter for the Fermi process is defined as

$$y \equiv 4D_1 t_1 = \frac{\langle \dot{E}_{\text{shear}} \rangle}{E} t_1 \quad (4.10)$$

It can be noticed from the Eq. (4.9) that the mean proton energy diverges as  $y \rightarrow 1$ , and hence  $y$  cannot exceed (or even equal) unity. Thus,  $y$ -parameter is the measure of how efficient the Fermi acceleration mechanism is.

In a steady state situation ( $\partial/\partial t \rightarrow 0$ ), the transport equation (Eq. 4.2) can be written in a form

$$D_1 E^2 \frac{\partial^2 f_G}{\partial E^2} + 4D_1 E \frac{\partial f_G}{\partial E} - \frac{f_G}{t_1} = -\frac{\dot{N}_1 \delta(E - E_i)}{E_i^2} \quad (4.11)$$

The solution of Eq. (4.11) for a Green's function is given by (Eq. 3.13 of SBK99)

$$f_G(E, E_i) = A_0 \begin{cases} (E/E_i)^{\alpha_1}, & E < E_i \\ (E/E_i)^{\alpha_2}, & E > E_i \end{cases} \quad (4.12)$$

where the exponents  $\alpha_1$ , and  $\alpha_2$  are related to  $D_1$  and  $t_1$  via

$$\alpha_1 \equiv -\frac{3}{2} + \left( \frac{9}{4} + \frac{4}{y} \right)^{1/2}, \quad \alpha_2 \equiv -\frac{3}{2} - \left( \frac{9}{4} + \frac{4}{y} \right)^{1/2}, \quad (4.13)$$

and the normalization parameter  $A_0$  has the value

$$A_0 = \frac{\dot{N}_1}{2D_1 E_i^3} \left( \frac{9}{4} + \frac{4}{y} \right)^{-1/2} \quad (4.14)$$

The Green's function  $f_G$  describes the response to the injection of  $\dot{N}_1$  protons per unit volume per unit time with energy  $E_i$ , and therefore it is easy to show based on the linearity of the transport equation (Eq. 4.11) that the particular solution for

a general source term  $j$  is obtained via the convolution

$$f(E) = \frac{\sqrt{2}m_p^{3/2}}{\dot{N}_1} \int_0^\infty E_i^{1/2} j(E_i) f_G(E, E_i) dE_i \quad (4.15)$$

where  $m_p(2m_p E_i)^{1/2} j(E_i) dE_i$  gives the number of protons injected per unit volume per unit time, in the energy range between  $E_i$  and  $E_i + dE_i$ .

For the physical application of interest here, the injected protons are supplied by the high-energy ( $E_i > E_c$ ) portion of the Maxwellian distribution in the hot disk. Hence the source term  $j(E_i)$  is given by

$$j(E_i) = \begin{cases} \frac{4\pi N_0 t_1^{-1}}{(2\pi m_p k_B T_i)^{3/2}} e^{-E_i/(k_B T_i)}, & E_i \geq E_c \\ 0, & E_i < E_c \end{cases} \quad (4.16)$$

where  $N_0$  and  $T_i$  are the proton number density, and the proton temperature in the hot accretion flow, respectively.  $E_c$  is the critical energy of the protons above which the protons escape into the wind.

The lower bound for the integration over  $E_i$  in Eq. (4.15) is set equal to  $E_c$  since the source  $j(E_i)$  vanishes for  $E_i < E_c$  according to Eq. (4.16). The result obtained for the non-thermal proton distribution is therefore given by [Subramanian and Becker \(2004\)](#) (SB04 from now onwards)

$$f(E) = f(\zeta) = \frac{8N_0 \{ \zeta^{\alpha_1} \Gamma(-\frac{3}{2} - \alpha_1, \zeta) - \zeta^{\alpha_2} [\Gamma(-\frac{3}{2} - \alpha_2, \zeta) - \Gamma(-\frac{3}{2} - \alpha_2, \zeta_c)] \}}{\sqrt{\pi} (k_B T_i)^3 (\alpha_1 - \alpha_2) y} \quad (4.17)$$

where we have introduced the dimensionless proton energy  $\zeta$  and the dimensionless critical energy  $\zeta_c$ , defined by

$$\zeta = \frac{E}{k_B T_i}, \quad \zeta_c = \frac{E_c}{k_B T_i} \quad (4.18)$$

The number and energy densities associated with the particular solution  $f$  above the critical energy  $E_c$  can be computed using

$$N_*(\text{cm}^{-3}) \equiv \int_{E_c}^\infty E^2 f(E) dE = (k_B T_i)^3 \int_{\zeta_c}^\infty \zeta^2 f(\zeta) d\zeta \quad (4.19)$$

$$U_*(\text{erg cm}^{-3}) \equiv \int_{E_c}^\infty E^3 f(E) dE = (k_B T_i)^4 \int_{\zeta_c}^\infty \zeta^3 f(\zeta) d\zeta \quad (4.20)$$

By combining Eqs. (4.17), (4.19) and (4.20), we find that the exact solutions for

$N_*$  and  $U_*$  are given by (SB04)

$$\frac{N_*}{N_0} = \frac{8\zeta_c^{3+\alpha_1}\Gamma(-\frac{3}{2} - \alpha_1, \zeta_c)}{\sqrt{\pi}(3 + \alpha_1)(\alpha_2 - \alpha_1)y} + e^{-\zeta_c} \left(\frac{\zeta_c}{\pi}\right)^{1/2} + \text{Erfc}(\zeta_c^{1/2}) \equiv \mathcal{N}(\zeta_c, y) \quad (4.21)$$

$$\frac{U_*}{N_0 k_B T_i} = \frac{8\zeta_c^{4+\alpha_1}\Gamma(-\frac{3}{2} - \alpha_1, \zeta_c)}{\sqrt{\pi}(4 + \alpha_1)(\alpha_2 - \alpha_1)y} + \frac{2\sqrt{\pi\zeta_c}(3 + 2\zeta_c)e^{-\zeta_c} + 3\pi\text{Erfc}(\zeta_c^{1/2})}{2\pi(1 - y)} \equiv \mathcal{E}(\zeta_c, y) \quad (4.22)$$

### 4.2.3 RADIOS model – the fluid description of inflow-outflow

BSK01 proposed the relativistic model for advection-dominated inflow-outflow solutions by incorporating the pseudo-Newtonian gravitational potential given by Paczyński and Wiita (1980) to include the approximate effects of general relativity in the inner regions of the disk. The self-similar inflow-outflow solutions of their model describe the structure of the disk outside the radius of marginal stability. The RADIOS model focuses on the gasdynamical winds which exert no torque on the underlying disk.

The pseudo-Newtonian potential is given by

$$\Phi = -\frac{GM}{R - 2R_g} \quad (4.23)$$

where  $R$  is the radius in the equatorial plane, and  $R_g = GM/c^2$  is the gravitational radius. This potential introduces a lengthscale in  $(R - 2R_g)$ , and all the self-similar scalings are done with respect to this lengthscale. The suitable expression for Keplerian angular velocity in this case is

$$\Omega_K = \sqrt{GM} \frac{R^{-1/2}}{R - 2R_g} \quad (4.24)$$

Assuming self-similarity, the variation of angular velocity  $\Omega$  in the quasi-Keplerian accretion flow is given by

$$\Omega(R) = \Omega_0 \Omega_K = \Omega_0 \sqrt{GM} \frac{R^{-1/2}}{R - 2R_g} \quad (4.25)$$

where  $\Omega_0$  is a measure of how sub-Keplerian the flow is. It is a positive constant having the value in the range  $0 < \Omega_0 < 1$ . Thus  $\Omega$  scales as  $\Omega_K$  throughout the disk.

Some part of the gravitational potential energy lost by the matter spiralling inward is presumably converted into heat by the viscous dissipation, with the rest powering the wind. Such an outwardly directed energy transport rate  $F_E$  (the energy



transported per unit time) in the disk scales as the rate of gravitational energy loss due to the inflow  $\dot{M}(R)$ , and given by

$$F_E(R) = \epsilon \frac{GM\dot{M}(R)}{R - 2R_g} \quad (4.26)$$

where  $\epsilon$  is a positive constant between zero and unity, and decides how much energy is being transported outwards from the disk as a fraction of gravitational energy transport rate.  $\dot{M}(R)$  denotes the mass accretion rate in the disk.

Similarly, the inwardly directed angular momentum transport rate  $I$  (angular momentum transported per unit time) in the disk scales as Keplerian angular momentum transport rate, and given by

$$I(R) = \frac{\lambda}{\Omega_0} R^2 \Omega \dot{M}(R) = \lambda \sqrt{GM} \dot{M}(R) \frac{R^{3/2}}{R - 2R_g} \quad (4.27)$$

where  $0 < \lambda < 1$ , and denotes the fraction of angular momentum transported inwards as compared to Keplerian angular momentum transport.

It is also assumed that the internal energy per unit mass scales as gravitational potential, implying that

$$a^2(R) = \frac{P}{\rho} = a_0^2 \frac{GM}{R - 2R_g} \quad (4.28)$$

where  $a$  is the isothermal sound speed,  $P$  and  $\rho$  are gas pressure, and mass density in the disk, respectively, and  $a_0$  is a positive constant between zero and unity.

Employing vertical hydrostatic equilibrium in the disk, and using scaling relations  $dP/dz \sim -P/z$ , and  $z \ll R$ , we can write

$$\frac{P}{z} \approx -\frac{\rho GM}{(R - 2R_g)^2} \frac{z}{R} \quad (4.29)$$

Using  $z \sim H$ , the half-thickness of the disk (or disk height), we get

$$\left(\frac{H}{R}\right)^2 = a_0^2 \left(\frac{R - 2R_g}{R}\right) \quad (4.30)$$

The scaling of radial infall velocity is assumed to have a relation

$$v(R) = v_0 \left(\frac{GM}{R - 2R_g}\right)^{1/2} \quad (4.31)$$

where  $v_0$  is a positive constant. Eq. (4.31) implies that the radial infall velocity is proportional to the local free-fall velocity  $v_{\text{ff}} = [2GM/(R - 2R_g)]^{1/2}$ . Note that we require  $v_0^2 < 2$ , in order to avoid inflow faster than free-fall.

Having defined the self-similar scalings of some important quantities in the disk

(Eqs. 4.25–4.31), we reckon the set of parameters used in the RADIOS model consists of  $\Omega_0$ ,  $\epsilon$ ,  $\lambda$ ,  $v_0$ , and  $a_0$ . As given in the Eqs. (2.28), (3.6), and (3.12) of BSK01, they are related by expressions

$$\lambda = \frac{\Omega_0}{2}, \quad a_0^2 = 2\Omega_0^2 - 2\epsilon, \quad v_0^2 = 8\epsilon - 10\Omega_0^2 + 2 \quad (4.32)$$

Additionally, the Shakura-Sunyaev  $\alpha$  parameter in the RADIOS model behaves as follows with respect to cylindrical radius  $R$

$$\alpha = \alpha_0 \left( \frac{R}{R - 2R_g} \right)^{1/2} \quad (4.33)$$

where  $\alpha_0$  is a positive constant given in terms of  $\Omega_0$  and  $\epsilon$  as

$$\alpha_0 = \frac{\Omega_0(8\epsilon - 10\Omega_0^2 + 2)^{1/2}}{4(\Omega_0^2 - \epsilon)} \quad (4.34)$$

The energy dissipated via viscosity per unit volume per unit time is expressed as

$$\dot{U}_{\text{viscous}} = \rho\nu R^2 \left( \frac{d\Omega}{dR} \right)^2 \quad (4.35)$$

Some part of this energy goes into heating of the gas in the disk, and the remainder is expelled into the wind. This can be represented by making use of the heating efficiency factor  $g(R)$ , and defined by

$$g(R)\rho\nu R^2 \left( \frac{d\Omega}{dR} \right)^2 \equiv \rho\nu R^2 \left( \frac{d\Omega}{dR} \right)^2 - \dot{U}_{\text{wind}} \quad (4.36)$$

Note that  $1 - g$  is the fraction of the viscous dissipated energy that goes into the wind. After some algebra (the details are given in BSK01),  $g(R)$  can be represented in terms of  $\Omega_0$ , and  $\epsilon$  as

$$g(R) = 4 \left( \frac{\Omega_0^2 - \epsilon}{\Omega_0^2} \right) \left( \frac{R - 2R_g}{3R - 2R_g} \right) \quad (4.37)$$

Looking at Eqs. (4.32), (4.34), and (4.37), we notice that the parameter space is two-dimensional, with  $\Omega_0$  and  $\epsilon$  as two independent parameters. All the other parameters can be expressed in terms of  $\Omega_0$  and  $\epsilon$ .

To find the allowable  $(\Omega_0 - \epsilon)$  parameter space, we make use of the constraints, such as  $0 < a_0^2 < 1$ ,  $0 < v_0^2 < 2$ ,  $0 < \Omega_0^2 < 1$ ,  $0 < g(R) < 1$ , and  $0 < \alpha_0 < 1$ , which results into the allowed parameter space

$$\max\left(\frac{\Omega_0^2}{4}, \frac{5\Omega_0^2 - 1}{4}\right) < \epsilon < \frac{\Omega_0}{4} [5\Omega_0 - (2 - \Omega_0^2)^{1/2}], \quad 0 < \Omega_0^2 < 1 \quad (4.38)$$

Now, the Bernoulli parameter of the flow can be defined as the specific energy of the protons in the flow. In the RADIOS model, the Bernoulli parameters of the disk, and the wind, are calculated. We use the wind Bernoulli parameter since we are trying to explain the launching of the outflows. Hence, we use Eq. (4.17) of BSK01 as a prescription for the Bernoulli parameter of the wind

$$b(R) = \frac{\epsilon GM(R + 6R_g)}{(R - 6R_g)(R - 2R_g)} \quad (4.39)$$

Note that  $b$  is always positive, since the wind is not gravitationally bound to the disk. Also,  $b(R)$  increases as we go towards smaller radii.

#### 4.2.4 Making a connection between fluid description and particle description

##### Relation between Fermi $y$ -parameter and allowed $(\Omega_0 - \epsilon)$ space of RADIOS

Having laid out the details of both particle, as well as fluid descriptions of the outflow explicitly, we are now ready to make connections between the two. An important quantity in the second-order Fermi acceleration mechanism is the Fermi  $y$ -parameter which is defined as  $y \equiv 4D_1 t_1$ .

The diffusion coefficient of protons in the energy space is given by Eq. (4.6) as

$$D_1 = \left( \frac{\tilde{\lambda}_1}{v_{\text{rms}}} \right) \left( \frac{dv_\phi}{dR} \right)^2, \quad (s^{-1}) \quad (4.40)$$

where  $\tilde{\lambda}_1$  is the magnetic coherence length in the disk, and  $v_\phi$  is the azimuthal velocity of an accretion flow given by

$$v_\phi = R\Omega = \Omega_0 \sqrt{GM} \frac{R^{1/2}}{R - 2R_g} \quad (4.41)$$

Here, we made use of the expression for angular velocity in quasi-Keplerian shear flow (Eq. 4.25). To reiterate,  $\Omega_0$  is a measure of how sub-Keplerian the flow is. The magnetic coherence length  $\tilde{\lambda}_1$  depends on the spectrum of turbulence that gives rise to irregularities in the magnetic field in the disk. [Shende, Chauhan, and Subramanian \(2021\)](#) incorporate this in their model of the hot, inner accretion disk by giving the prescription for  $\tilde{\lambda}_1$  as

$$\tilde{\lambda}_1 = D_c H \quad (4.42)$$

where  $D_c$  depends on the parameters of turbulence in the disk, and  $H$  is the disk

height given by Eq. (4.30) as

$$\left(\frac{H}{R}\right)^2 = a_0^2 \left(\frac{R - 2R_g}{R}\right) \quad (4.43)$$

with the help of which, Eq. (4.42) can be reduced to

$$\tilde{\lambda}_1 = a_0 D_c R^{1/2} (R - 2R_g)^{1/2} \quad (4.44)$$

Using Eqs. (4.41), and (4.44), Eq. (4.40) reduces to give the energy diffusion coefficient of protons in the disk as a function of parameters in the RADIOS model

$$D_1 = \frac{1}{4} a_0 D_c \Omega_0^2 GM \left(\frac{m_p}{3k_B T_i}\right)^{1/2} \frac{(R + 2R_g)^2}{R^{1/2} (R - 2R_g)^{7/2}} \quad (4.45)$$

The timescale  $t_1$  for which protons stay in the acceleration region can be represented as

$$t_1 = \frac{H}{v_1} \quad (4.46)$$

where  $v_1$  is the diffusion velocity of protons escaping from the disk, and is given as  $v_1 = v_{\text{rms}} \tilde{\lambda}_1 / H = v_{\text{rms}} D_c$ , where we have used Eq. (4.42). Using Eq. (4.43), and the expression for  $v_1$ , we get the following expression for  $t_1$

$$t_1 = \frac{a_0}{D_c} \left(\frac{m_p}{3k_B T_i}\right)^{1/2} R^{1/2} (R - 2R_g)^{1/2} \quad (4.47)$$

where  $a_0$  relates to the isothermal sound speed, and is the measure of how internal energy per unit mass scales as gravitational potential.  $a_0$  is related to  $\Omega_0$  and  $\epsilon$  via Eq. (4.32).

Now that we have represented  $D_1$  and  $t_1$  in terms of parameters of the RADIOS model, we are now in a position to express the Fermi  $y$ -parameter using Eqs. (4.45), and (4.47) as

$$y = \frac{a_0^2 \Omega_0^2}{3} \left(\frac{m_p c^2}{k_B T_i}\right) \frac{(r + 2)^2}{(r - 2)^3} \quad (4.48)$$

where  $r = R/R_g$  is the cylindrical radius represented in terms of gravitational radius  $R_g \equiv GM/c^2$ .

### Connecting specific energies of both descriptions

To reiterate, the Bernoulli parameter of the outflow is defined as the specific energy of the proton population escaping into the wind, given by Eq. (4.39) as

$$b(r) = \frac{\epsilon c^2 (r + 6)}{(r - 6)(r - 2)} \quad (4.49)$$

If  $\Gamma_\infty$  is the asymptotic Lorentz factor of the outflow, then its kinetic energy is given by  $(\Gamma_\infty - 1)m_p c^2$ . Since the Bernoulli parameter is the same as terminal kinetic energy per unit mass, we have the following relation

$$b(r) = (\Gamma_\infty - 1)c^2, \quad i.e., \quad \Gamma_\infty = \frac{b(r)}{c^2} + 1 \quad (4.50)$$

On the other hand, we can compute the specific energy of the escaping population by making use of the distribution function of  $f(\zeta)$  of protons in the disk (Eq. 4.17). If we consider  $E_c$  as the critical energy over which the protons escape to form a wind, then using Eqs. (4.21), and (4.22), the specific energy of the wind can be written as

$$\frac{U_*}{N_* m_p} = \frac{k_B T_i}{m_p} \frac{\mathcal{E}(\zeta_c, y)}{\mathcal{N}(\zeta_c, y)} \quad (4.51)$$

where  $y$  in the expressions of  $\mathcal{E}$  and  $\mathcal{N}$  has a value given by Eq. (4.48).

Now, we make a connection between the fluid description of the outflow given by RADIOS (BSK01), and the particle description given by SBK99, by equating Eqs. (4.49), and (4.51), leading to

$$\epsilon = \left( \frac{k_B T_i}{m_p c^2} \right) \frac{\mathcal{E}(r-6)(r-2)}{\mathcal{N}(r+6)} \quad (4.52)$$

The main motive of our work is to examine the behavior of the escaping energy  $\zeta_c$  with radius, which is possible by solving Eq. (4.52). A point in the permissible parameter space specified by the equation (4.38) fixes the value of  $\epsilon$  in Eq. (4.52), and we can solve for the escaping energy  $\zeta_c$  as a function of the radius  $r$ .

### Wind mass loss rate

It would be interesting to calculate the rate at which the mass is lost in the wind from the disk. The differential wind mass loss rate from the annulus of thickness  $dR$  can be written as

$$d\dot{m} = 2\pi R m_p N_* 2H \frac{dR}{t_1} \quad (4.53)$$

where  $N_*$  is the number density of the protons escaping into the wind (Eq. 4.21). Using the expressions for disk height  $H$  (Eq. 4.43), mean escaping timescale  $t_1$  (Eq. 4.47), along with Eq. (4.21) for the number density of escaping proton population, we can calculate how the wind mass loss rate behaves with radius

$$\frac{d\dot{m}}{dR} = W \mathcal{N} R \quad (4.54)$$

where the quantity  $W$  is defined as

$$W \equiv 4\pi D_c (3m_p k_B T_i)^{1/2} N_0 = 4\pi D_c m_p v_{\text{rms}} N_0 \quad (4.55)$$

$N_0$  being the proton number density in the disk.

### 4.3 Results

Having discussed the details of our model for relativistic outflows from advection-dominated disks, our main objective is to find out how the non-thermal, high-energy tail of the proton distribution function (the shaded portion of the distribution function shown in figures 4.1 and 4.4) escapes in the form of a wind. For that, we solve the equation connecting the fluid description, and the particle acceleration description of the outflow, i.e., we solve Eq. (4.52) for the critical energy  $\zeta_c$  required for the escape of protons in the form of a wind. Note that the free parameters are same as those of the RADIOS model, which are  $\Omega_0$  (which tells us how sub-Keplerian the disk is), and  $\epsilon$  (which decides how much fraction of energy is being transported outwards from the disk as compared to the gravitational energy transport rate). Eq. (4.38) specifies the allowed parameter space, a plot of which is shown in figure (4.2). The upper and lower bounds for  $\epsilon$  given in Eq. (4.38) are shown as three curves in figure (4.2). The shaded closed area between these curves is the permissible parameter space. We run a grid of models with various combinations of the free parameters  $\Omega_0$  and  $\epsilon$  within the allowable parameter space (figure 4.2). For concreteness, we have shown our results (figures 4.3, 4.5–4.7) for three points in the allowable parameter space, which are  $(\Omega_0, \epsilon) \equiv (0.4, 0.05)$ ,  $(0.5, 0.12)$ , and  $(0.6, 0.24)$ , without loss of generality. The value of the proton temperature is assumed to be  $T_i = 10^{11}$  K.

Figure (4.3) represents the variation of  $\zeta_c$  with respect to the cylindrical radius  $r = R/R_g$ , where  $R_g = GM/c^2$  is the gravitational radius. Different linestyles represent different points in the permissible parameter space. Green line corresponds to  $\Omega_0 = 0.4$  and  $\epsilon = 0.05$ , blue line represents  $\Omega_0 = 0.5$  and  $\epsilon = 0.12$ , whereas the point corresponding to  $\Omega_0 = 0.6$  and  $\epsilon = 0.24$  is represented by the red line. We notice that  $\zeta_c$  increases for smaller radii, implying the powerful outflows from the inner regions of the disk. To understand this pictorially, the non-thermal tail of the proton distribution function is getting snipped at higher energies for smaller radii as shown in figure (4.4). Bernoulli parameter  $b(r)$ , and consequently asymptotic Lorentz factor ( $\Gamma_\infty$ ) of the outflow are depicted in the figure (4.5). Linestyles are similar to those used in the figure (4.3). Notice that, only the flow originated closer to the marginally stable radius is relativistic, otherwise it is non-relativistic, which is expected, since the average energy of the escaping proton population increases for the

protons starting with smaller cylindrical radii; this is evident from the figure (4.4). This is a consequence of a steep gradient in the pseudo-Newtonian potential closer to the black hole. Figure (4.6) depicts the number density, and the energy density of escaping proton population into the wind. The lower values of number density, and energy density closer to the black hole imply that the gas is very tenuous at smaller radii. This can be explained again with the help of figure (4.4) that, although the average energy of the protons escaping into the wind increases as we go to smaller radii, the number of protons in the escaping population decreases. We also calculated the rate at which mass is lost into the wind (Eq. 4.54). The quantity  $d\dot{m}/dR$  is plotted in the figure (4.7a) in units of  $4\pi m_p v_{\text{rms}} R_g D_c N_0$ , and as a function of the cylindrical radius  $r$ . Notice that the wind mass loss rate decreases for smaller radii for the reasons just discussed, in accordance with figure (4.6a). It is also useful to plot the wind mass loss rate  $d\dot{m}/dR$  superimposed on the plot of asymptotic Lorentz factor  $\Gamma_\infty$ . Figure (4.7b) shows such overlap. We see that the plots for  $\Gamma_\infty$  and  $d\dot{m}/dR$  show opposite trends with radius.  $\Gamma_\infty$  is monotonically decreasing function of the radius  $r$ , whereas  $d\dot{m}/dR$  shows monotonous increase with  $r$ .

We also checked how the results are affected by the variation of a single parameter, keeping the other parameters fixed. Such an effect is described in the figures (4.8) and (4.9). Figure (4.8) represents the profiles of  $\zeta_c$ , wind Bernoulli parameter  $b(r)$ , wind asymptotic Lorentz factor ( $\Gamma_\infty$ ), number density and energy density of the escaping proton population, and wind mass loss rate  $d\dot{m}/dR$  in units of  $4\pi m_p v_{\text{rms}} R_g D_c N_0$ , keeping  $\Omega_0 = 0.5$ , and varying the values of  $\epsilon$ . Different linestyles represent different values of  $\epsilon$  and are indicated in the insets of every plot. In the figure (4.8), we notice that, at a particular radius, the quantities  $\zeta_c$ ,  $b(r)$ , and  $\Gamma_\infty$  increase for the increasing values of  $\epsilon$ , whereas number density ( $N_*$ ) and energy density ( $U_*$ ) of protons in the wind, and  $d\dot{m}/dR$  decrease for the increasing values of  $\epsilon$ . Figure (4.9) depicts the profiles of the same quantities as that of figure (4.8), but keeping  $\epsilon$  fixed to the value  $\epsilon = 0.1$ , and varying the value of  $\Omega_0$ , with different linestyles representing the different values of  $\Omega_0$ . We see in the figure (4.9) that  $\zeta_c$  decreases with increase in  $\Omega_0$ , whereas number density ( $N_*$ ) and energy density ( $U_*$ ) of wind protons, and  $d\dot{m}/dR$  increase for the increasing values of  $\Omega_0$ . As expected from the equation (4.49), the Bernoulli parameter, and hence the asymptotic Lorentz factor of the outflow is independent of  $\Omega_0$ , which is evident in figures (4.9b) and (4.9c).

## 4.4 Discussion and conclusions

To summarize, the relativistic outflows from advection-dominated accretion flows have been mostly dealt by employing the fluid description, without paying elabo-

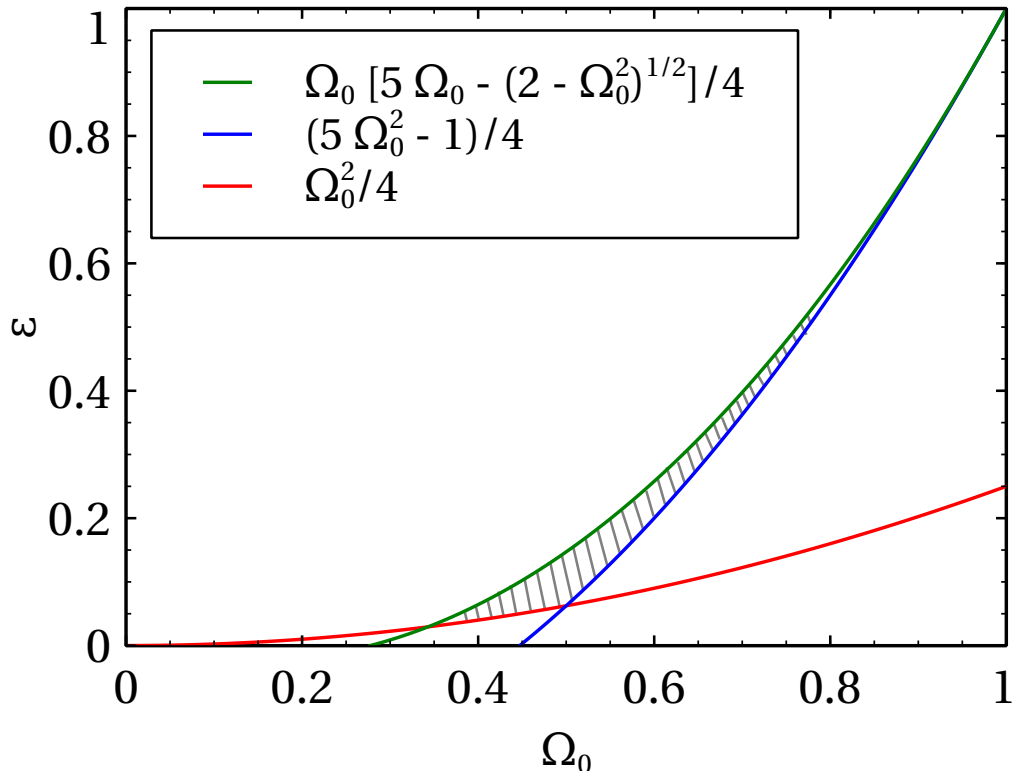


Figure 4.2: The  $(\Omega_0-\epsilon)$  parameter space of RADIOS (BSK01) (shaded closed area between three curves)

rate attention to the acceleration mechanisms operative in the disk that produce these outflows. On the other hand, there is another body of literature which deals with the energetics of particles in accretion flows which employ microphysical acceleration mechanisms to launch particle-dominated winds from the disk (SBK99; Blackman, 1999; Gruzinov and Quataert, 1999). In this work, we have tried to tie these two descriptions together in order to establish a concrete disk-wind connection. BSK01 proposed self-similar solutions for the disk/wind structure by incorporating the pseudo-Newtonian prescription for the gravitational potential (Paczynski and Wiita, 1980) in order to include the effects of general relativity. The outflows in their model are relativistic, and originate mainly from the inner parts of the advection-dominated accretion disk, close to the radius of marginal stability. On the other hand, SBK99 studied the launching of relativistic outflows by way of invoking the second-order Fermi acceleration mechanism in shearing accretion disk coronae to power a pressure driven wind. In this work, we have connected the fluid description of the RADIOS model (BSK01), and the particle description of SBK99. We derive the distribution function of protons in the hot, advection-dominated flow, and derive the wind Bernoulli parameter (Eq. 4.51) using the distribution function. We then connect it with the RADIOS model by equating the Bernoulli parameters of both the descriptions (Eq 4.52). To conclude,



- We have tried to explain heavy, particle dominated, relativistic winds from advection-dominated accretion disks and connected the particle distribution function level description to the fluid description of outflows.
- By solving Eq. (4.52) for the critical energy  $\zeta_c$  (energy above which the protons escape into the wind), we have successfully shown how the high energy, non-thermal tail of the proton distribution function (the shaded region of the distribution function in figures 4.1 and 4.4) is being ejected in the form of a relativistic wind. We have noticed in the figure (4.3) that the critical energy  $\zeta_c$  increases as we move closer to the black hole. What this means in terms of the distribution function is that the tail is getting smaller for smaller radii, with increasing average energy in the tail. Hence, only the protons having very high energies near the radius of marginal stability are allowed to escape. In conclusion, the relativistic wind is increasingly non-thermal at smaller radii. This is apparent from figures (4.3) and (4.4).
- This translates into the behavior of the wind Bernoulli parameter  $b(r)$  (specific energy per unit mass of the wind), and the asymptotic Lorentz factor ( $\Gamma_\infty = b(r)/c^2 + 1$ ). They show the similar behavior as that of  $\zeta_c$  with radius. This can be explained using the simple scaling argument of the energy of protons. Note that  $\Gamma_\infty \sim E/m_p c^2$ , where  $E$  is the energy of protons. From Eqs. (4.19), and (4.20), we can approximately write mass density  $\rho_m \propto E^2$ , and energy density  $U_* \propto E^3$ , so that  $\Gamma_\infty \sim U_*/\rho_m \propto E$ . In other words,  $\Gamma_\infty \propto \zeta_c$ , which implies that as  $\zeta_c$  increases, the asymptotic Lorentz factor increases with it, and that happens when we go to smaller radii towards the black hole. Figure (4.5) depicts this scenario.
- We observed from the figure (4.8) that outflows are more energetic for the larger values of  $\epsilon$ , since  $\epsilon$  is associated with the amount of outward energy transfer from the disk. Larger the value of  $\epsilon$ , more energetic will be the outflow.
- We found that the number density, and the energy density of the escaping proton population go on decreasing for the decreasing value of the radius (figure 4.6). This is again a consequence of the fact that the wind is increasingly non-thermal at smaller radii, and the number of protons escaping into the wind decreases for smaller radii. This translates into smaller wind mass loss rates closer to the black hole (figure 4.7).

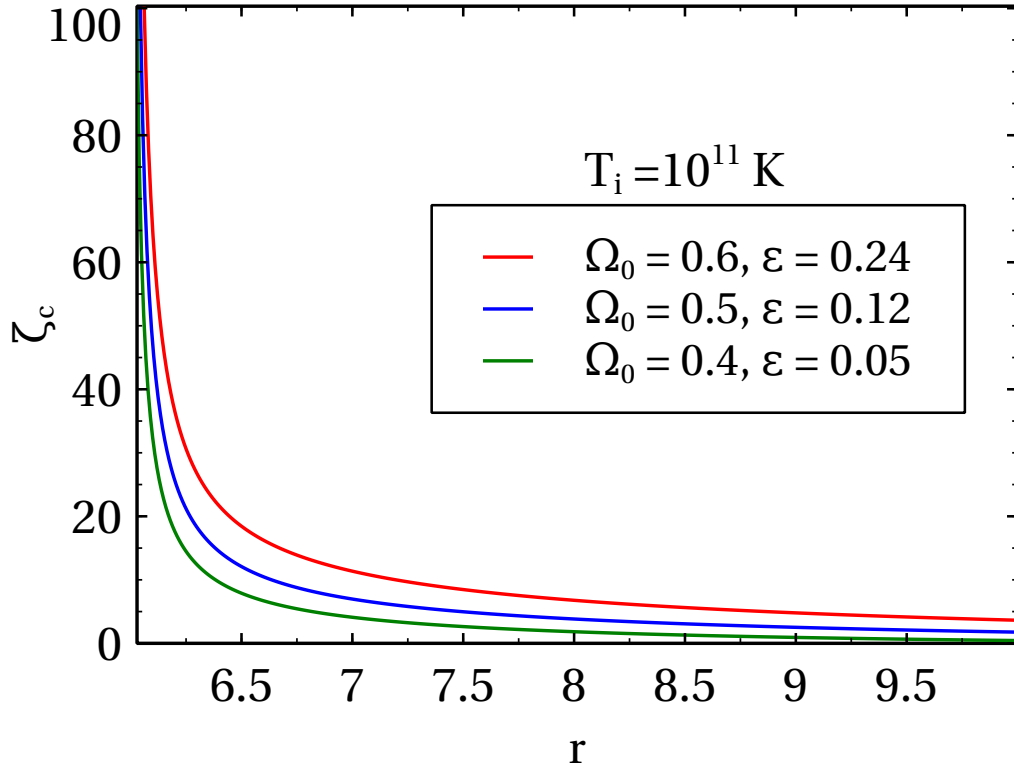


Figure 4.3:  $\zeta_c$  as a function of radius ( $r = R/R_g$ ) in the equatorial plane

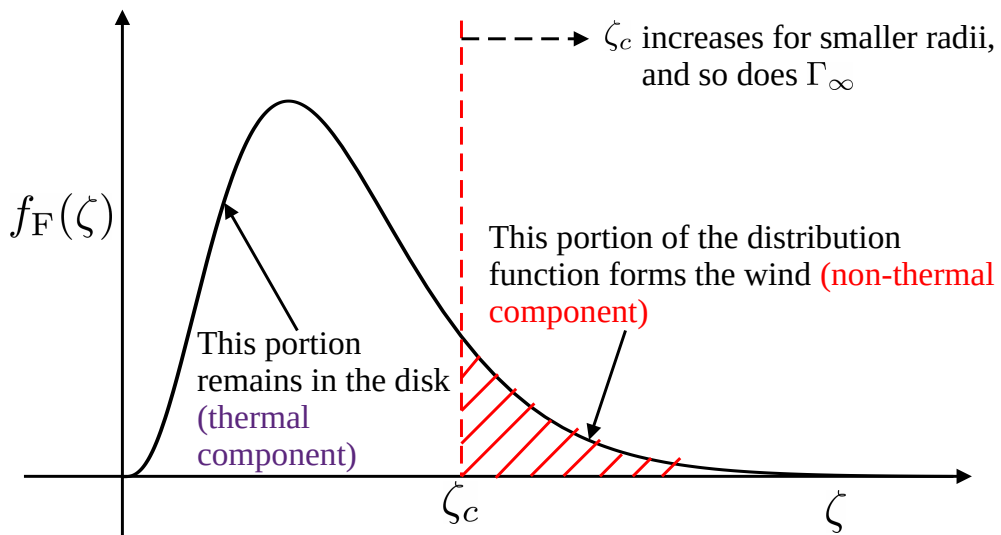
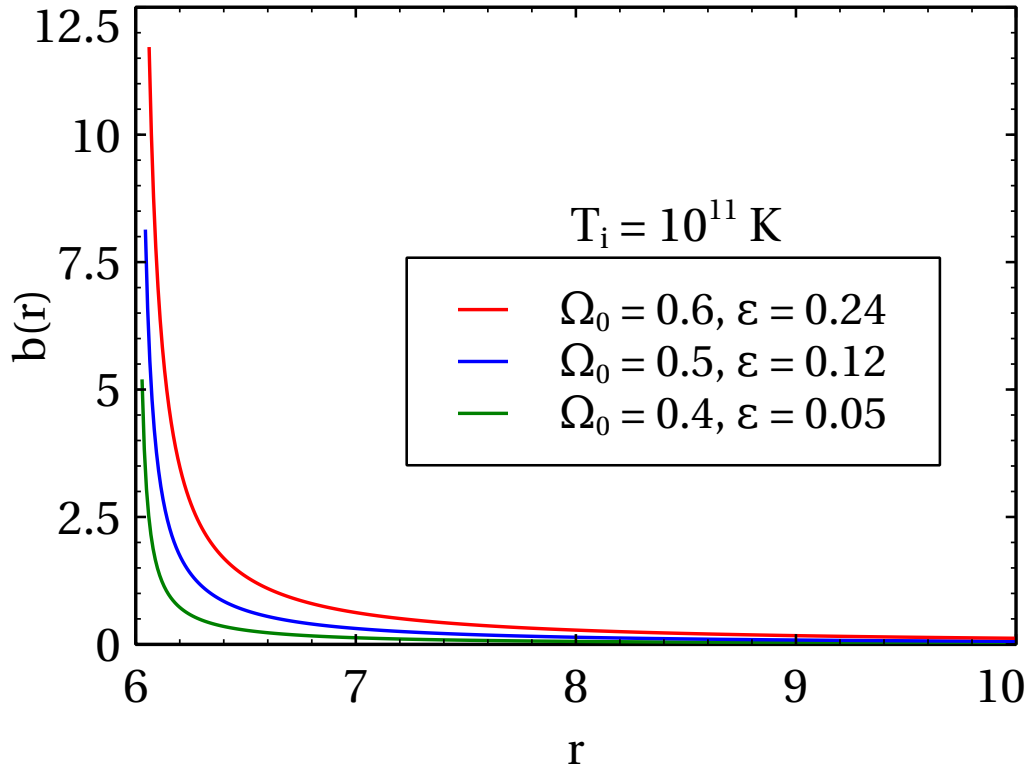
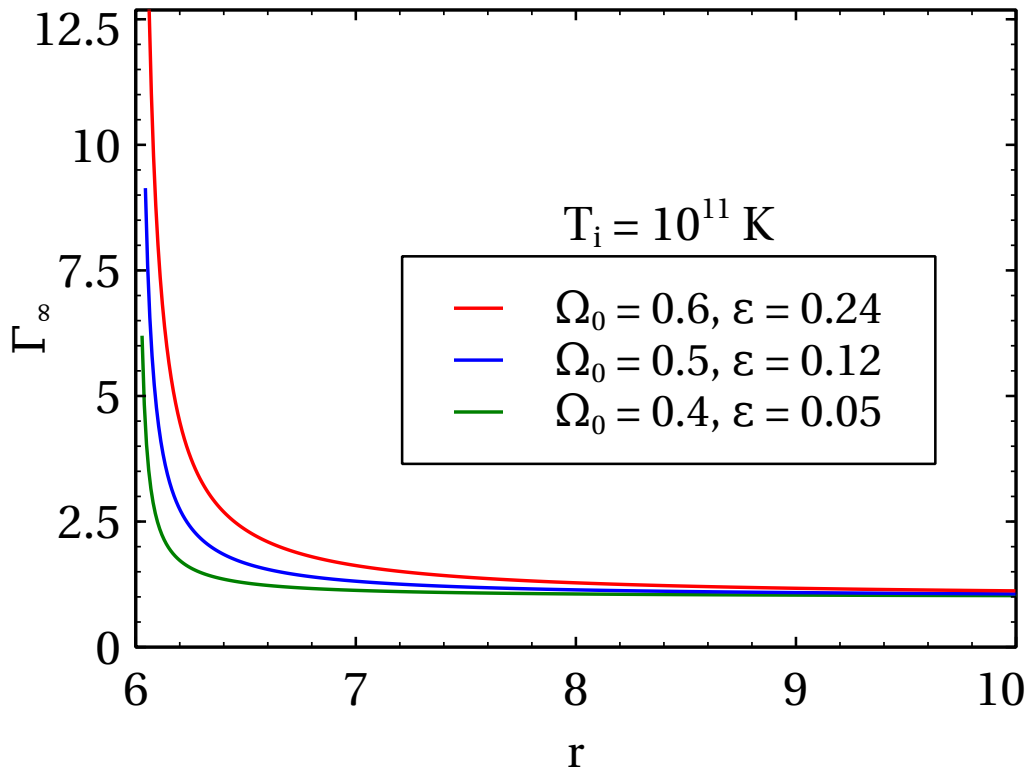


Figure 4.4: Schematic representation of proton distribution function in a hot, advective disk

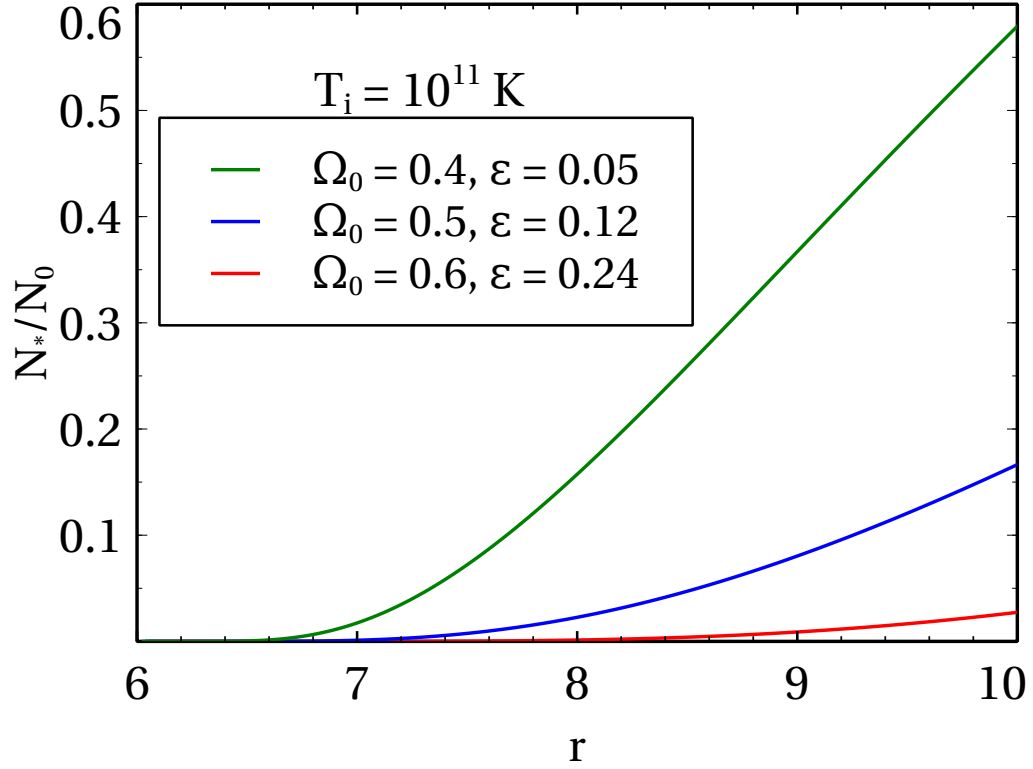


(a)

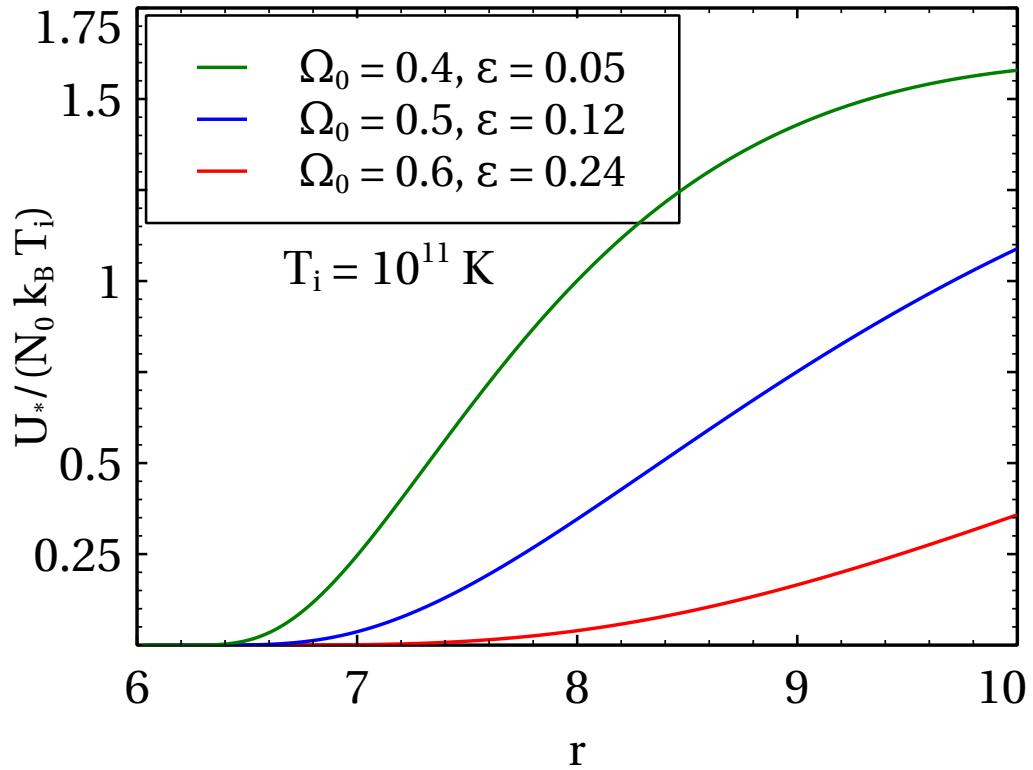


(b)

Figure 4.5: Profiles of (a) wind Bernoulli parameter  $b(r)$  (in units of  $c^2$ ), and (b) asymptotic Lorentz factor ( $\Gamma_\infty$ ), as functions of cylindrical radius

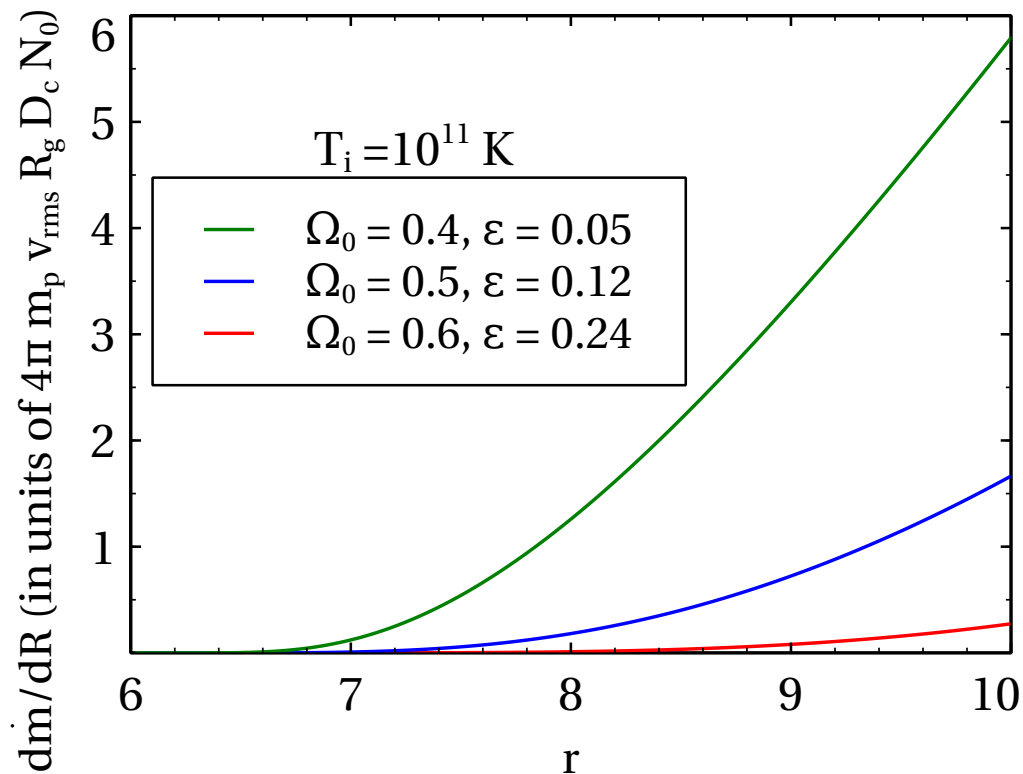


(a)

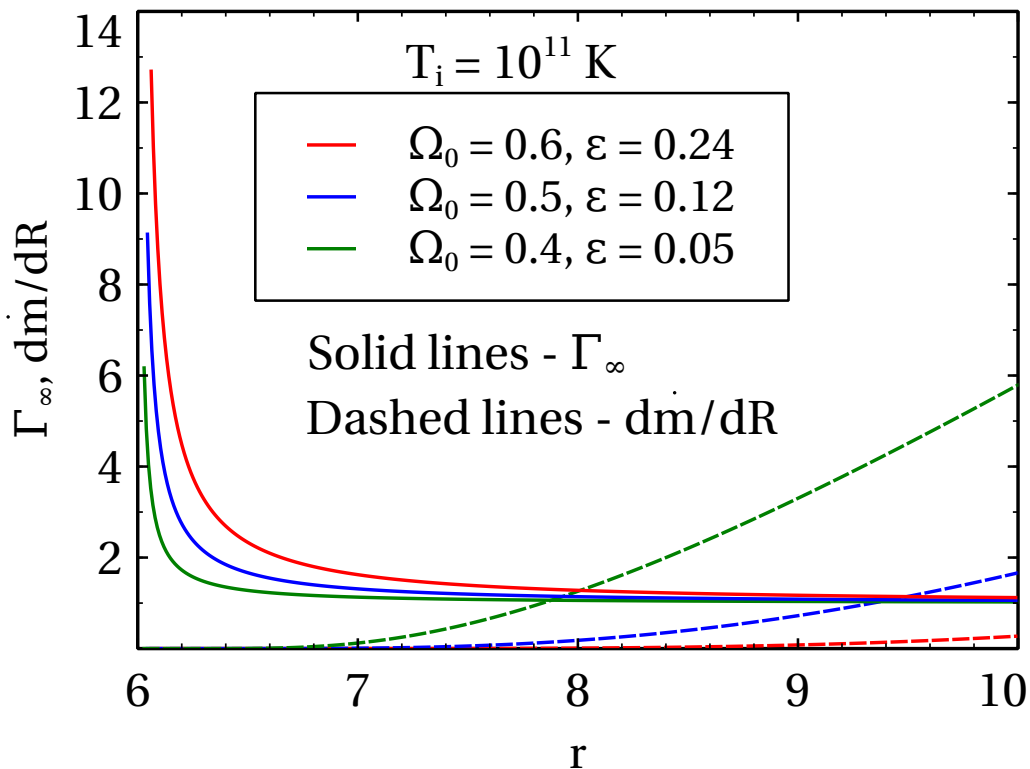


(b)

Figure 4.6: Profiles of (a) number density, and (b) energy density of proton population escaping into the wind as a function of cylindrical radius



(a)



(b)

Figure 4.7: (a) Profile of wind mass loss rate  $dm/dR$  in units of  $4\pi m_p v_{\text{rms}} R_g D_c N_0$ , and (b) Superimposing the plots of  $\Gamma_\infty$  (fig. 4.5b), and  $dm/dR$  (with same units as that of fig. 4.7a). The color codes of both solid, and dashed lines are shown in the box

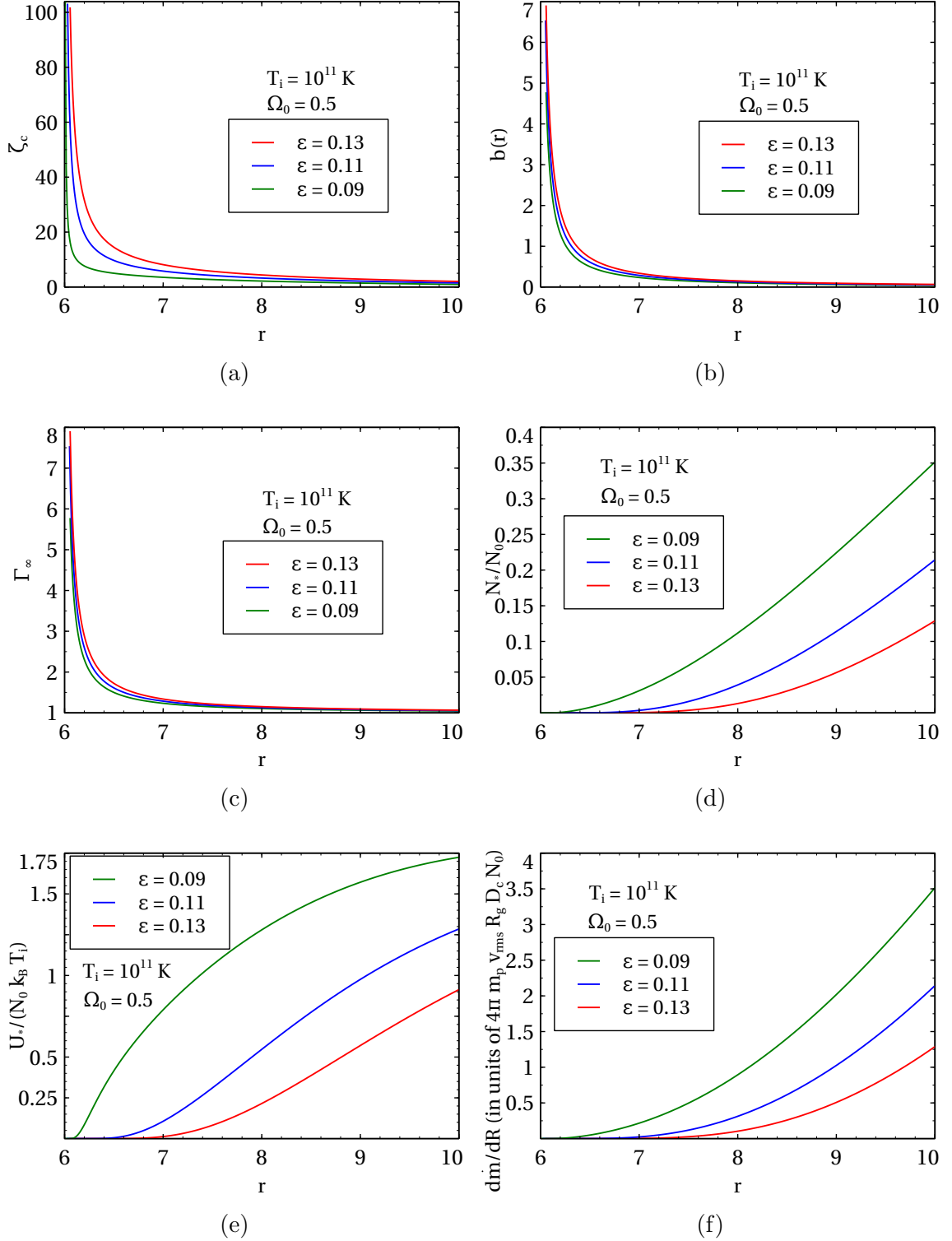


Figure 4.8: Profiles of (a)  $\zeta_c$ , (b) wind Bernoulli parameter  $b(r)$  (in units of  $c^2$ ), (c) asymptotic Lorentz factor ( $\Gamma_\infty$ ) for the wind, (d) number density of escaping proton population, (e) energy density of escaping proton population, (f) wind mass loss rate  $dm/dR$ , as functions of radius ( $r = R/R_g$ ) in the equatorial plane. These are plotted with  $\Omega_0 = 0.5$ , and for different values of  $\epsilon$ .

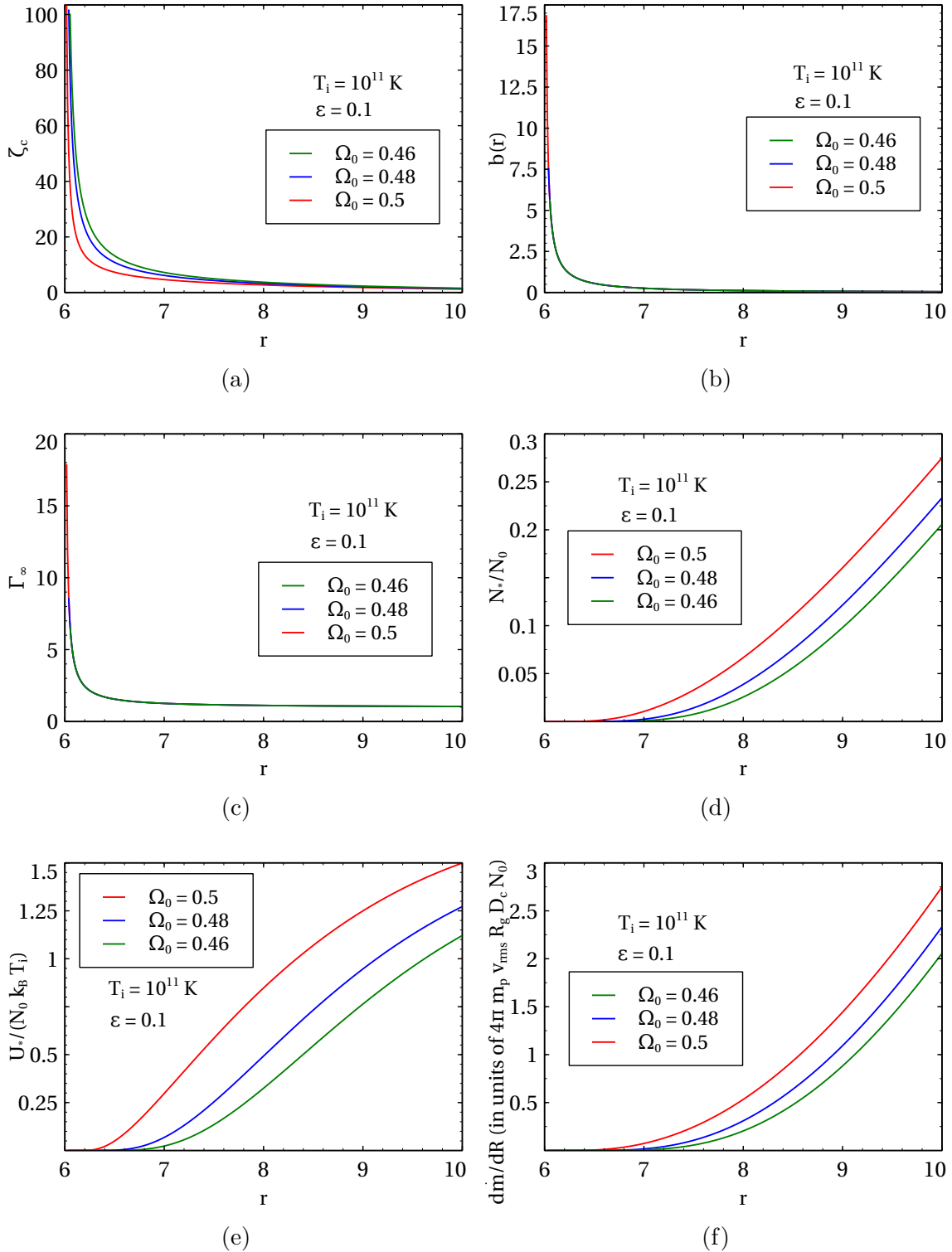


Figure 4.9: Profiles of (a)  $\zeta_c$ , (b) wind Bernoulli parameter  $b(r)$  (in units of  $c^2$ ), (c) asymptotic Lorentz factor ( $\Gamma_\infty$ ) for the wind, (d) number density of escaping proton population, (e) energy density of escaping proton population, (f) wind mass loss rate  $dm/dR$ , as functions of radius ( $r = R/R_g$ ) in the equatorial plane. These are plotted with  $\epsilon = 0.1$ , and for different values of  $\Omega_0$ .





# Chapter 5

## Summary and Future Work

### 5.1 Summary

The focus of this thesis is on the accretion disk-jet connection in black hole sources. Relativistic outflows coming out of AGN and some galactic black hole sources are believed to be powered by the accretion of matter around the central black hole. Several AGN and microquasars exhibit interesting observational behavior in which significant dips in the X-ray light curve are followed by ejections of plasmoids at radio frequency that move at relativistic speeds. Since the X-ray emission from these sources is believed to be emanating from the inner parts of an accretion disk, and the radio emission from the jet, these observations imply that there is a specific connection between the events happening in the jet and the underlying accretion disk.

In Chapter 2, we investigated the eruption mechanism of episodic blobs from the inner, hot accretion disk/corona. We explained the launching of such blobs by drawing analogies with the triggering of coronal mass ejections from the solar corona. We treated the plasmoids as pre-existing current carrying magnetic flux ropes that were initially anchored in the accretion disk-corona. The forces acting on the blob are 1) the Lorentz self-force or hoop force which tends to expand it outwards, 2) the Lorentz force due to the external poloidal field which tries to hold the blob down and 3) the gravitational attraction due to the black hole. If the Lorentz force due to the external field decreases fast enough with distance from disk midplane, the flux rope is subject to an MHD instability, called the “toroidal instability (TI)”, which causes it to erupt outwards. The TI, which was originally explored in the context of laboratory tokamak plasmas, has been very successful in explaining coronal mass ejections from the Sun. We found that our detailed model predictions compare favorably with a representative set of multi-epoch observations of radio emitting knots from the radio galaxy 3C 120.

On the other hand, the temporal behaviour of X-rays is thought to arise from the rapid collapse of the hot, inner parts of their accretion disks. The collapse can occur over the radial infall time-scale of the inner accretion disk. However, estimates of this time-scale are hindered by a lack of knowledge of the operative viscosity in the collisionless plasma comprising the inner disk. In Chapter 3, we used published simulation results for cosmic ray diffusion through turbulent magnetic fields to arrive at a viscosity prescription appropriate to hot accretion disks, instead of parametrizing the viscosity in terms of Shakura-Sunyaev  $\alpha$  parameter. We constructed simplified disk models using this viscosity prescription and estimated disk collapse time scales for AGN 3C 120 and 3C 111, and a galactic microquasar GRS 1915+105. We found that our inner disk collapse time-scale estimates agree well with those of the observed X-ray dips. We also noticed that the collapse time-scale is most sensitive to the outer radius of the hot accretion disk. We found that the values of the Shakura-Sunyaev  $\alpha$  parameter arising from our viscosity prescription range from 0.02 to 0.08. The combined work of Chapters 2, and 3 outlines a plausible scenario for episodes of (inner) disc collapse accompanied by plasmoid ejection.

In addition to studying episodic mass ejections, we also worked on details of the origin of (matter dominated) steady winds from advection-dominated hot accretion disks. In Chapter 4, we built upon previous published work outlining self-consistent inflow-outflow solutions. While these solutions employ fluid equations to demonstrate the plausibility of (steady) relativistic winds, there have not been many attempts to link it to particle acceleration mechanisms in the hot, inner disk which presumably causes such outflows to form. We have tried to tie these two descriptions together in order to establish a concrete disk-wind connection. Bridging the fluid description of RADIOS model (Becker, Subramanian, and Kazanas, 2001), and the particle description of Subramanian, Becker, and Kazanas (1999), we successfully showed how the high energy tail of the proton distribution function escapes in the form of a relativistic wind.

## 5.2 Future Work

### 5.2.1 Confinement of energetic electrons in a blob, and effect of blobs on large-scale jet structure

In Chapter 2, we calculated the mass loss rate due to episodic blob ejections from an accretion disk, based on the assumption that the highly relativistic electrons are responsible for the observed radio emission from the blob, by way of emitting synchrotron radiation. We had also assumed that these electrons are confined within the blob by tangled magnetic fields, without paying attention to the confinement

mechanisms operative in the blob. Our understanding of cosmic ray confinement in the galaxy suggests that energetic electrons cannot stream down the large scale magnetic fields because of the pitch angle anisotropy generated due to synchrotron radiation. This anisotropy leads to the resonant Alfvén instability, which causes electrons to shed a turbulent spectrum of hydromagnetic waves that can scatter the electrons and tend to restore isotropy (Kulsrud and Pearce, 1969; Wentzel, 1969). Such pitch angle scattering of electrons off the turbulent wave spectrum could cause them to be (self) confined in the blob. Future studies could focus on a better understanding of such self-confinement mechanisms, in analogy with the cosmic ray confinement in galactic magnetic fields.

Subramanian et al. (2012) investigated the possibility of firehose instability as a cause of TeV blazar variability, in which they point out that the bulk streaming of the jet plasma renders the pressure in the jet anisotropic, with the parallel pressure ( $P_{\parallel}$  : pressure along the jet) exceeding the perpendicular pressure ( $P_{\perp}$ ). Such a configuration is susceptible to non-resonant, fluid instability called the firehose instability, which can lead to disruptions in a large-scale jet structure and cause variability in the emission. Future studies could try to figure out the parallel pressure that would be exerted by a series of successive blobs, and how it affects the large scale structure of the jet by linking it to the possible development of the firehose instability.

### 5.2.2 Energy dissipation in winds, and alternate acceleration mechanisms

In chapter 4, we proposed a disk-wind model where the relativistic winds are launched from the advection-dominated accretion disk powered by a second-order Fermi-acceleration mechanism. We assumed the presence of tangled magnetic fields embedded in the accretion flow, which act as scattering centers. The Fermi acceleration is governed by the collisions of protons with magnetic scattering centers, which leads to the formation of a non-thermal tail of the proton distribution function. We assumed that the jet expands adiabatically and all the internal energy is converted into kinetic energy of the jet at infinity. Energy losses in the form of dissipation and radiation drag were not taken into account. Future work could examine the dissipation of tangled magnetic fields by finding a prescription for magnetic dissipation such as that of Heinz and Begelman (2000). This could help us understand the trade-offs between the energy conversion from magnetic energy to bulk kinetic energy, random particle energy, and radiation. We would also like to study the effect of radiation drag on the dynamics of the jet.

For our work on relativistic winds, we have taken into account one specific ac-

celeration mechanism for powering the winds, i.e., second-order Fermi acceleration in advection-dominated flows. It would be interesting to investigate the presence of other acceleration mechanisms as well. For example, the possibility of jet launching by way of accelerating the protons at a standing, centrifugally supported shock in the underlying accretion disk via the first-order Fermi mechanism has been investigated (Le and Becker, 2004, 2005). Future studies could incorporate both the first and second order acceleration mechanisms to study the origin of relativistic particle dominated outflows.

Additionally, it would be good to better constrain the particle content of the jet. We have considered hadronic jets in our models, i.e., electron-proton plasmas. It would also be interesting to see how the dynamics would change if the plasma were dominantly comprised of electrons and positrons.

### 5.2.3 Time-dependent disk model, and quasi-periodic oscillations (QPOs)

In chapter 3, we used a prescription for the microphysical viscosity operative in the hot, inner accretion disk. However, our work uses a simplified steady-state disk model. To have a better understanding of the disk dynamics, we need to study the time evolution of the disk. There is previous work concerning the disk dynamics by prescribing time-dependent accretion in  $\alpha$  disk models (Lipunova and Shakura, 2001; Lipunova, 2015). Future work could investigate time-dependent disk models using the viscosity mechanism we have studied in this thesis.

A wide class of black hole X-ray binaries (BHXRBS) show quasi-periodic oscillations (QPOs) in their X-ray flux. Various explanations for the occurrence of QPOs exist, one of which advocates that the QPOs occur due to the oscillations of the shock at centrifugal barrier in the accretion flow (Aktar et al., 2018; Das et al., 2021). We would like to investigate how our disk model is able to explain the QPOs; specifically, how QPOs are affected by our viscosity prescription.

# Appendix A

## Two-Temperature Accretion Disk, Comptonized Model

Considering an accretion disk with a cylindrical symmetry, and no vertical structure, the relevant component of the stress arising from the hybrid viscosity is given by (SBK96)

$$\alpha_{\text{hyb}}P \equiv -\eta_{\text{hyb}}R \frac{d\Omega_{\text{kepl}}}{dR} \quad (\text{A.1})$$

For a two-temperature, hot accretion disk, we use the disk structure equations as those used by [Eilek and Kafatos \(1983\)](#) which neglect the radiation pressure, and are given by

$$P = \frac{GMm_{\text{p}}N_iH^2f_1}{R^3} \quad (\text{Vertical hydrostatic equilibrium}) \quad (\text{A.2})$$

$$\alpha P = \frac{(GMR)^{1/2}\dot{M}f_2}{4\pi R^2H} \quad (\text{Radial momentum transport}) \quad (\text{A.3})$$

$$\frac{3}{8\pi} \frac{GM\dot{M}}{R^3H} f_3 = 3.75 \times 10^{21} m_{\text{p}} \ln \Lambda N_i^2 k_{\text{B}} \frac{(T_i - T_e)}{T_e^{3/2}} \quad (\text{Energy equation}) \quad (\text{A.4})$$

$$P = N_i k_{\text{B}} (T_i + T_e) \quad (\text{Equation of state}) \quad (\text{A.5})$$

$$T_e = \frac{m_e c^2 y}{4k_{\text{B}}} \frac{1}{\tau_{\text{es}} g(\tau_{\text{es}})} \quad (\text{Comptonized electrons}) \quad (\text{A.6})$$

$$\tau_{\text{es}} = N_i \sigma_{\text{T}} H \quad (\text{Definition of optical depth}) \quad (\text{A.7})$$

where  $y$  is the Compton  $y$ -parameter,  $\sigma_{\text{T}}$  is a Thomson scattering cross section,  $\tau_{\text{es}}$  is the electron scattering optical depth and the function  $g(\tau_{\text{es}}) \equiv 1 + \tau_{\text{es}}$ . We have

taken the value of Coulomb logarithm  $\ln \Lambda$  to be 15 in our calculations. In deriving these equations, we have assumed the steady state conditions. Also, we assume that the disk is quasi-Keplerian, so that the azimuthal velocity  $v_\phi$  is essentially the Keplerian velocity  $= \sqrt{GM/R}$ , and the radial drift velocity  $v_R \ll v_\phi$ . Since there is no vertical structure by assumption, we can adopt the scaling relations  $\partial P/\partial z \sim -P/H$ , and  $z \sim H$ . Eq. (A.2) denotes the vertical hydrostatic equilibrium, whereas Eq. (A.3) represents the angular momentum transport. Ion thermal balance is given by Eq. (A.4), whereas unsaturated Compton cooling is given by Eq. (A.6). The system of equations is completed with the equation of state, Eq. (A.5), and the optical depth definition, Eq. (A.7). The factors  $f_1$ ,  $f_2$  and  $f_3$  are the relativistic correction factors for the metric under consideration (Novikov and Thorne, 1973; Page and Thorne, 1974). For our calculations, we have used the values of  $f_1$ ,  $f_2$  and  $f_3$  for a Schwarzschild black hole ( $a_* = a/M = 0$ ).

Assuming  $T_i \gg T_e$  and making the definitions  $M_8 \equiv M/10^8 M_\odot$ , and  $R_* \equiv R/(GM/c^2)$ , equations (A.2)–(A.7) yield the following analytical solutions:

$$T_i = 1.08 \times 10^{13} \frac{\dot{M}}{\dot{M}_E} f_2 \tau_{\text{es}}^{-1} \alpha^{-1} R_*^{-3/2} \quad (\text{A.8})$$

$$T_e = 1.48 \times 10^9 y \tau_{\text{es}}^{-1} [g(\tau_{\text{es}})]^{-1} \quad (\text{A.9})$$

$$N_i = 1.02 \times 10^{11} \left( \frac{\dot{M}}{\dot{M}_E} \right)^{-1/2} M_8^{-1} f_1^{1/2} f_2^{-1/2} \alpha^{1/2} \tau_{\text{es}}^{3/2} R_*^{-3/4} \quad (\text{A.10})$$

where  $\dot{M}/\dot{M}_E$  represents the accretion rate in units of Eddington rate ( $\dot{M}_E \equiv L_E/c^2$ , where  $L_E \equiv 4\pi GMm_p c/\sigma_T$  is the Eddington luminosity and  $\sigma_T$  is the Thomson electron scattering cross section). It may be emphasized that  $\alpha$  is a free parameter in the above solutions.

# Bibliography

- R. Aktar, S. Das, A. Nandi, and H. Sreehari. Advective accretion flow properties around rotating black holes - application to GRO J1655-40. *Journal of Astrophysics and Astronomy*, 39(1):17, Feb. 2018. doi: 10.1007/s12036-017-9507-0.
- S. A. Balbus and J. F. Hawley. A Powerful Local Shear Instability in Weakly Magnetized Disks. I. Linear Analysis. *ApJ*, 376:214, July 1991. doi: 10.1086/170270.
- S. A. Balbus and J. F. Hawley. Instability, turbulence, and enhanced transport in accretion disks. *Reviews of Modern Physics*, 70(1):1–53, Jan 1998. doi: 10.1103/RevModPhys.70.1.
- G. Bateman. *MHD instabilities*. 1978.
- P. A. Becker, P. Subramanian, and D. Kazanas. Relativistic Outflows from Advection-dominated Accretion Disks around Black Holes. *ApJ*, 552(1):209–220, May 2001. doi: 10.1086/320433.
- M. C. Begelman. Instability of Toroidal Magnetic Field in Jets and Plerions. *ApJ*, 493(1):291–300, Jan. 1998. doi: 10.1086/305119.
- T. Belloni. Inner Disk Oscillations. *Astrophysics and Space Science Supplement*, 276:145–152, 2001.
- T. Belloni, M. Méndez, A. R. King, M. van der Klis, and J. van Paradijs. An Unstable Central Disk in the Superluminal Black Hole X-Ray Binary GRS 1915+105. *ApJ*, 479:L145–L148, Apr. 1997. doi: 10.1086/310595.
- E. G. Blackman. On particle energization in accretion flows. *MNRAS*, 302(4):723–730, Feb. 1999. doi: 10.1046/j.1365-8711.1999.02139.x.
- R. D. Blandford and M. C. Begelman. On the fate of gas accreting at a low rate on to a black hole. *MNRAS*, 303(1):L1–L5, Feb. 1999. doi: 10.1046/j.1365-8711.1999.02358.x.

- R. D. Blandford and D. G. Payne. Hydromagnetic flows from accretion discs and the production of radio jets. *MNRAS*, 199:883–903, June 1982. doi: 10.1093/mnras/199.4.883.
- R. D. Blandford and R. L. Znajek. Electromagnetic extraction of energy from Kerr black holes. *MNRAS*, 179:433–456, May 1977. doi: 10.1093/mnras/179.3.433.
- R. D. Blandford, H. Netzer, and L. Woltjer. Active Galactic Nuclei. In *Active Galactic Nuclei*, Jan. 1990.
- J. L. Blum, J. M. Miller, A. C. Fabian, M. C. Miller, J. Homan, M. van der Klis, E. M. Cackett, and R. C. Reis. Measuring the Spin of GRS 1915+105 with Relativistic Disk Reflection. *ApJ*, 706(1):60–66, Nov. 2009. doi: 10.1088/0004-637X/706/1/60.
- E. Bosman, V. Bothmer, G. Nisticò, A. Vourlidas, R. A. Howard, and J. A. Davies. Three-Dimensional Properties of Coronal Mass Ejections from STEREO/SECCHI Observations. *Sol. Phys.*, 281:167–185, Nov. 2012. doi: 10.1007/s11207-012-0123-5.
- A. Brandenburg, A. Nordlund, R. F. Stein, and U. Torkelsson. Dynamo-generated Turbulence and Large-Scale Magnetic Fields in a Keplerian Shear Flow. *ApJ*, 446:741, June 1995. doi: 10.1086/175831.
- J. Candia and E. Roulet. Diffusion and drift of cosmic rays in highly turbulent magnetic fields. *J. Cosmology Astropart. Phys.*, 10:007, Oct. 2004. doi: 10.1088/1475-7516/2004/10/007.
- C. Casadio, J. L. Gómez, P. Grandi, S. G. Jorstad, A. P. Marscher, M. L. Lister, Y. Y. Kovalev, T. Savolainen, and A. B. Pushkarev. The Connection between the Radio Jet and the Gamma-ray Emission in the Radio Galaxy 3C 120. *ApJ*, 808:162, Aug. 2015a. doi: 10.1088/0004-637X/808/2/162.
- C. Casadio, J. L. Gómez, P. Grandi, S. G. Jorstad, A. P. Marscher, M. L. Lister, Y. Y. Kovalev, T. Savolainen, and A. B. Pushkarev. The Connection between the Radio Jet and the Gamma-ray Emission in the Radio Galaxy 3C 120. *arXiv e-prints*, Aug. 2015b.
- F. Casse, M. Lemoine, and G. Pelletier. Transport of cosmic rays in chaotic magnetic fields. *Phys. Rev. D*, 65(2):023002, Jan 2002. doi: 10.1103/PhysRevD.65.023002.
- A. J. Castro-Tirado, S. Brandt, and N. Lund. GRS 1915+105. *IAU Circ.*, 5590:2, Aug. 1992.



- S. Chakrabarti and L. G. Titarchuk. Spectral Properties of Accretion Disks around Galactic and Extragalactic Black Holes. *ApJ*, 455:623, Dec 1995. doi: 10.1086/176610.
- S. K. Chakrabarti, P. Goldoni, P. J. Wiita, A. Nandi, and S. Das. On the Ejection Mechanism of Bullets in SS 433. *ApJ*, 576:L45–L48, Sept. 2002. doi: 10.1086/343104.
- R. Chatterjee, A. P. Marscher, S. G. Jorstad, A. R. Olmstead, I. M. McHardy, M. F. Aller, H. D. Aller, A. Lähteenmäki, M. Tornikoski, T. Hovatta, K. Marshall, H. R. Miller, W. T. Ryle, B. Chicka, A. J. Benker, M. C. Bottorff, D. Brokofsky, J. S. Campbell, T. S. Chonis, C. M. Gaskell, E. R. Gaynullina, K. N. Grankin, C. H. Hedrick, M. A. Ibrahimov, E. S. Klimek, A. K. Kruse, S. Masatoshi, T. R. Miller, H.-J. Pan, E. A. Petersen, B. W. Peterson, Z. Shen, D. V. Strel'nikov, J. Tao, A. E. Watkins, and K. Wheeler. Disk-Jet Connection in the Radio Galaxy 3C 120. *ApJ*, 704:1689–1703, Oct. 2009. doi: 10.1088/0004-637X/704/2/1689.
- R. Chatterjee, A. P. Marscher, S. G. Jorstad, A. Markowitz, E. Rivers, R. E. Rothschild, I. M. McHardy, M. F. Aller, H. D. Aller, A. Lähteenmäki, M. Tornikoski, B. Harrison, I. Agudo, J. L. Gómez, B. W. Taylor, and M. Gurwell. Connection Between the Accretion Disk and Jet in the Radio Galaxy 3C 111. *ApJ*, 734(1): 43, Jun 2011. doi: 10.1088/0004-637X/734/1/43.
- J. Chen. Theory of prominence eruption and propagation: Interplanetary consequences. *J. Geophys. Res.*, 101:27499–27520, Dec. 1996. doi: 10.1029/96JA02644.
- X. Cheng, Y. Guo, and M. Ding. Origin and Structures of Solar Eruptions I: Magnetic Flux Rope. *Science in China Earth Sciences*, 60:1383–1407, Aug. 2017. doi: 10.1007/s11430-017-9074-6.
- I. Contopoulos and D. Kazanas. A Cosmic Battery. *ApJ*, 508(2):859–863, Dec. 1998. doi: 10.1086/306426.
- I. Contopoulos, A. Nathanail, and M. Katsanikas. The Cosmic Battery in Astrophysical Accretion Disks. *ApJ*, 805:105, June 2015. doi: 10.1088/0004-637X/805/2/105.
- I. Contopoulos, A. Nathanail, A. Sądowski, D. Kazanas, and R. Narayan. Numerical simulations of the Cosmic Battery in accretion flows around astrophysical black holes. *MNRAS*, 473:721–727, Jan. 2018. doi: 10.1093/mnras/stx2249.
- J. Contopoulos and D. Kazanas. Relativistic hadrons and the origin of relativistic outflows in active galactic nuclei. *ApJ*, 441:521–532, Mar. 1995. doi: 10.1086/175379.

- L. Costamante. Blazars - an updated review. In *Multifrequency Behaviour of High Energy Cosmic Sources - XIII. 3-8 June 2019. Palermo*, page 35, Dec. 2020.
- H. D. Curtis. *Pub. Lick Obs.*, 13:31, 1918.
- A. Dar and A. Laor. Hadronic Production of TeV Gamma-Ray Flares from Blazars. *ApJ*, 478(1):L5–L8, Mar. 1997. doi: 10.1086/310544.
- S. Das, A. Nandi, V. K. Agrawal, I. K. Dihingia, and S. Majumder. Relativistic viscous accretion flow model for ULX sources: a case study for IC 342 X-1. *MNRAS*, 507(2):2777–2781, Oct. 2021. doi: 10.1093/mnras/stab2307.
- P. Démoulin and G. Aulanier. Criteria for Flux Rope Eruption: Non-equilibrium Versus Torus Instability. *ApJ*, 718:1388–1399, Aug. 2010. doi: 10.1088/0004-637X/718/2/1388.
- J. A. Earl, J. R. Jokipii, and G. Morfill. Cosmic-Ray Viscosity. *ApJ*, 331:L91, Aug. 1988. doi: 10.1086/185242.
- J. A. Eilek and M. Kafatos. The high-energy spectrum of hot accretion disks. *ApJ*, 271:804–819, Aug. 1983. doi: 10.1086/161246.
- R. Fender and T. Belloni. GRS 1915+105 and the Disc-Jet Coupling in Accreting Black Hole Systems. *ARA&A*, 42:317–364, Sept. 2004. doi: 10.1146/annurev.astro.42.053102.134031.
- R. P. Fender, S. T. Garrington, D. J. McKay, T. W. B. Muxlow, G. G. Pooley, R. E. Spencer, A. M. Stirling, and E. B. Waltman. MERLIN observations of relativistic ejections from GRS 1915+105. *MNRAS*, 304:865–876, Apr. 1999. doi: 10.1046/j.1365-8711.1999.02364.x.
- J. Frank, A. King, and D. J. Raine. *Accretion Power in Astrophysics: Third Edition*. 2002.
- A. A. Galeev, R. Rosner, and G. S. Vaiana. Structured coronae of accretion disks. *ApJ*, 229:318–326, Apr. 1979. doi: 10.1086/156957.
- S. K. Garain, D. S. Balsara, S. K. Chakrabarti, and J. Kim. Effects of Magnetic Field Loops on the Dynamics of Advective Accretion Flows and Jets around a Schwarzschild Black Hole. *ApJ*, 888(2):59, Jan. 2020. doi: 10.3847/1538-4357/ab5d3c.
- J. Giacalone and J. R. Jokipii. The Transport of Cosmic Rays across a Turbulent Magnetic Field. *ApJ*, 520(1):204–214, Jul 1999. doi: 10.1086/307452.

- D. Giannios, D. A. Uzdensky, and M. C. Begelman. Fast TeV variability in blazars: jets in a jet. *MNRAS*, 395:L29–L33, May 2009. doi: 10.1111/j.1745-3933.2009.00635.x.
- J.-L. Gómez, A. P. Marscher, A. Alberdi, S. G. Jorstad, and C. García-Miró. Flashing Superluminal Components in the Jet of the Radio Galaxy 3C120. *Science*, 289:2317–2320, Sept. 2000. doi: 10.1126/science.289.5488.2317.
- N. Gopalswamy. STEREO and SOHO contributions to coronal mass ejection studies: Some recent results. In *Astronomical Society of India Conference Series*, volume 10 of *Astronomical Society of India Conference Series*, 2013.
- J. T. Gosling, E. Hildner, R. M. MacQueen, R. H. Munro, A. I. Poland, and C. L. Ross. Mass ejections from the sun - A view from SKYLAB. *J. Geophys. Res.*, 79:4581–4587, Nov. 1974. doi: 10.1029/JA079i031p04581.
- T. Gou, R. Liu, B. Kliem, Y. Wang, and A. M. Veronig. The Birth of A Coronal Mass Ejection. *arXiv e-prints*, Nov. 2018.
- A. Gruzinov and E. Quataert. The Proton Distribution Function in Weakly Magnetized Turbulent Plasmas. *ApJ*, 520(2):849–852, Aug. 1999. doi: 10.1086/307472.
- E. M. Gutiérrez, F. L. Vieyro, and G. E. Romero. Nonthermal processes in hot accretion flows onto supermassive black holes: An inhomogeneous model. *A&A*, 649:A87, May 2021. doi: 10.1051/0004-6361/202039671.
- P. J. Hargrave and M. Ryle. Observations of Cygnus A with the 5-km radio telescope. *MNRAS*, 166:305–327, Feb. 1974. doi: 10.1093/mnras/166.2.305.
- J. F. Hawley and S. A. Balbus. A Powerful Local Shear Instability in Weakly Magnetized Disks. II. Nonlinear Evolution. *ApJ*, 376:223, July 1991. doi: 10.1086/170271.
- S. Heinz and M. C. Begelman. Jet Acceleration by Tangled Magnetic Fields. *ApJ*, 535(1):104–117, May 2000. doi: 10.1086/308820.
- M. R. Hoerbe, P. J. Morris, G. Cotter, and J. Becker Tjus. On the relative importance of hadronic emission processes along the jet axis of active galactic nuclei. *MNRAS*, 496(3):2885–2901, Aug. 2020. doi: 10.1093/mnras/staa1650.
- T. Hovatta and E. Lindfors. Relativistic Jets of Blazars. *New A Rev.*, 87:101541, Dec. 2019. doi: 10.1016/j.newar.2020.101541.

- A. J. Hundhausen, C. B. Sawyer, L. House, R. M. E. Illing, and W. J. Wagner. Coronal mass ejections observed during the solar maximum mission - Latitude distribution and rate of occurrence. *J. Geophys. Res.*, 89:2639–2646, May 1984. doi: 10.1029/JA089iA05p02639.
- S. Ichimaru. Bimodal behavior of accretion disks: theory and application to Cygnus X-1 transitions. *ApJ*, 214:840–855, June 1977. doi: 10.1086/155314.
- P. A. Isenberg and T. G. Forbes. A Three-dimensional Line-tied Magnetic Field Model for Solar Eruptions. *ApJ*, 670:1453–1466, Dec. 2007. doi: 10.1086/522025.
- J. R. Jokipii. Cosmic-Ray Propagation. I. Charged Particles in a Random Magnetic Field. *ApJ*, 146:480, Nov 1966. doi: 10.1086/148912.
- R. K. Joshi, I. Chattopadhyay, and L. Yadav. Radiatively driven, time dependent bipolar outflows. *MNRAS*, 509(1):85–99, Jan. 2022. doi: 10.1093/mnras/stab2841.
- M. Kafatos. Alpha disks. *Advances in Space Research*, 8(2-3):105–112, Jan 1988. doi: 10.1016/0273-1177(88)90392-4.
- S. S. Kimura, K. Tomida, and K. Murase. Acceleration and escape processes of high-energy particles in turbulence inside hot accretion flows. *MNRAS*, 485(1): 163–178, May 2019. doi: 10.1093/mnras/stz329.
- B. Kliem and T. Török. Torus Instability. *Physical Review Letters*, 96(25):255002, June 2006. doi: 10.1103/PhysRevLett.96.255002.
- B. Kliem, J. Lin, T. G. Forbes, E. R. Priest, and T. Török. Catastrophe versus Instability for the Eruption of a Toroidal Solar Magnetic Flux Rope. *ApJ*, 789: 46, July 2014. doi: 10.1088/0004-637X/789/1/46.
- J. A. Klimchuk. Theory of Coronal Mass Ejections. *Washington DC American Geophysical Union Geophysical Monograph Series*, 125, 2001. doi: 10.1029/GM125p0143.
- R. Kulsrud and W. P. Pearce. The Effect of Wave-Particle Interactions on the Propagation of Cosmic Rays. *ApJ*, 156:445, May 1969. doi: 10.1086/149981.
- L. D. Landau, E. M. Lifshitz, and L. P. Pitaevskii. *Electrodynamics of continuous media; 2nd ed.* Course of theoretical physics. Butterworth, Oxford, 1984. URL <https://cds.cern.ch/record/712712>.

- T. Le and P. A. Becker. A Self-consistent Model for the Formation of Relativistic Outflows in Advection-dominated Accretion Disks with Shocks. *ApJ*, 617:L25–L28, Dec. 2004. doi: 10.1086/427075.
- T. Le and P. A. Becker. Particle Acceleration and the Production of Relativistic Outflows in Advection-dominated Accretion Disks with Shocks. *ApJ*, 632:476–498, Oct. 2005. doi: 10.1086/432927.
- J. Lin and T. G. Forbes. Effects of reconnection on the coronal mass ejection process. *J. Geophys. Res.*, 105:2375–2392, Feb. 2000. doi: 10.1029/1999JA900477.
- G. V. Lipunova. Evolution of Finite Viscous Disks with Time-independent Viscosity. *ApJ*, 804(2):87, May 2015. doi: 10.1088/0004-637X/804/2/87.
- G. V. Lipunova and N. I. Shakura. Time-dependent accretion  $\alpha$ -disks in binary systems. In A. Gimenez, V. Reglero, and C. Winkler, editors, *Exploring the Gamma-Ray Universe*, volume 459 of *ESA Special Publication*, pages 317–320, Sept. 2001.
- J. Y. Liu, E. L. Qiao, and B. F. Liu. Revisiting the Structure and Spectrum of the Magnetic-reconnection-heated Corona in Luminous AGNs. *ApJ*, 833:35, Dec. 2016a. doi: 10.3847/1538-4357/833/1/35.
- R. Liu, B. Kliem, V. S. Titov, J. Chen, Y. Wang, H. Wang, C. Liu, Y. Xu, and T. Wiegmann. Structure, Stability, and Evolution of Magnetic Flux Ropes from the Perspective of Magnetic Twist. *ApJ*, 818:148, Feb. 2016b. doi: 10.3847/0004-637X/818/2/148.
- R. V. E. Lovelace, J. C. L. Wang, and M. E. Sulkanen. Self-collimated electromagnetic jets from magnetized accretion disks. *ApJ*, 315:504–535, Apr. 1987. doi: 10.1086/165156.
- M. Lyutikov. Magnetocentrifugal launching of jets from discs around Kerr black holes. *MNRAS*, 396(3):1545–1552, July 2009. doi: 10.1111/j.1365-2966.2009.14811.x.
- K. Mannheim. The proton blazar. *A&A*, 269:67–76, Mar. 1993.
- B. Margon, H. C. Ford, S. A. Grandi, and R. P. S. Stone. Enormous periodic Doppler shifts in SS 433. *ApJ*, 233:L63–L68, Oct. 1979a. doi: 10.1086/183077.
- B. Margon, H. C. Ford, J. I. Katz, K. B. Kwitter, R. K. Ulrich, R. P. S. Stone, and A. Klemola. The bizarre spectrum of SS 433. *ApJ*, 230:L41–L45, May 1979b. doi: 10.1086/182958.

- A. P. Marscher and S. G. Jorstad. *3C 120 and the Disk-Jet Connection*, volume 360 of *Astronomical Society of the Pacific Conference Series*, page 153. 2006.
- A. P. Marscher, S. G. Jorstad, J.-L. Gómez, M. F. Aller, H. Teräsranta, M. L. Lister, and A. M. Stirling. Observational evidence for the accretion-disk origin for a radio jet in an active galaxy. *Nature*, 417:625–627, June 2002. doi: 10.1038/nature00772.
- R. Matsumoto and T. Tajima. Magnetic Viscosity by Localized Shear Flow Instability in Magnetized Accretion Disks. *ApJ*, 445:767, Jun 1995. doi: 10.1086/175739.
- J. C. McKinney, A. Tchekhovskoy, and R. D. Blandford. General relativistic magnetohydrodynamic simulations of magnetically choked accretion flows around black holes. *MNRAS*, 423:3083–3117, July 2012. doi: 10.1111/j.1365-2966.2012.21074.x.
- D. Mihalas and B. W. Mihalas. *Foundations of radiation hydrodynamics*. 1984.
- J. M. Miller, M. L. Parker, F. Fuerst, M. Bachetti, F. A. Harrison, D. Barret, S. E. Boggs, D. Chakrabarty, F. E. Christensen, W. W. Craig, A. C. Fabian, B. W. Grefenstette, C. J. Hailey, A. L. King, D. K. Stern, J. A. Tomsick, D. J. Walton, and W. W. Zhang. NuSTAR Spectroscopy of GRS 1915+105: Disk Reflection, Spin, and Connections to Jets. *ApJ*, 775(2):L45, Oct. 2013. doi: 10.1088/2041-8205/775/2/L45.
- K. A. Miller and J. M. Stone. The Formation and Structure of a Strongly Magnetized Corona above a Weakly Magnetized Accretion Disk. *ApJ*, 534:398–419, May 2000. doi: 10.1086/308736.
- I. F. Mirabel and L. F. Rodríguez. A superluminal source in the Galaxy. *Nature*, 371:46–48, Sept. 1994. doi: 10.1038/371046a0.
- K. Miyamoto. *Plasma physics for nuclear fusion*. 1980.
- A. Mizuta, T. Ebisuzaki, T. Tajima, and S. Nagataki. Production of intense episodic Alfvén pulses: GRMHD simulation of black hole accretion discs. *MNRAS*, 479: 2534–2546, Sept. 2018. doi: 10.1093/mnras/sty1453.
- T. Mondal and B. Mukhopadhyay. Magnetized advective accretion flows: formation of magnetic barriers in magnetically arrested discs. *MNRAS*, 476:2396–2409, May 2018. doi: 10.1093/mnras/sty332.
- T. C. Mouschovias and A. I. Poland. Expansion and broadening of coronal loop transients - A theoretical explanation. *ApJ*, 220:675–682, Mar. 1978. doi: 10.1086/155951.

- S. Naik, P. C. Agrawal, A. R. Rao, B. Paul, S. Seetha, and K. Kasturirangan. Detection of a Series of X-Ray Dips Associated with a Radio Flare in GRS 1915+105. *ApJ*, 546:1075–1085, Jan. 2001. doi: 10.1086/318280.
- A. Nandi, S. K. Chakrabarti, S. V. Vadawale, and A. R. Rao. Ejection of the inner accretion disk in GRS 1915+105: The magnetic rubber-band effect. *A&A*, 380: 245–250, Dec 2001. doi: 10.1051/0004-6361:20011444.
- R. Narayan and I. Yi. Advection-dominated Accretion: A Self-similar Solution. *ApJ*, 428:L13, June 1994. doi: 10.1086/187381.
- R. Narayan and I. Yi. Advection-dominated Accretion: Self-Similarity and Bipolar Outflows. *ApJ*, 444:231, May 1995a. doi: 10.1086/175599.
- R. Narayan and I. Yi. Advection-dominated Accretion: Underfed Black Holes and Neutron Stars. *ApJ*, 452:710, Oct. 1995b. doi: 10.1086/176343.
- H. Netzer. Revisiting the Unified Model of Active Galactic Nuclei. *ARA&A*, 53: 365–408, Aug. 2015. doi: 10.1146/annurev-astro-082214-122302.
- I. D. Novikov and K. S. Thorne. Astrophysics of black holes. In *Black Holes (Les Astres Occlus)*, pages 343–450, Jan 1973.
- B. Paczyński and P. J. Wiita. Thick accretion disks and supercritical luminosities. *A&A*, 88:23–31, Aug. 1980.
- P. Padovani, D. M. Alexander, R. J. Assef, B. De Marco, P. Giommi, R. C. Hickox, G. T. Richards, V. Smolčić, E. Hatziminaoglou, V. Mainieri, and M. Salvato. Active galactic nuclei: what’s in a name? *A&A Rev.*, 25(1):2, Aug. 2017. doi: 10.1007/s00159-017-0102-9.
- D. N. Page and K. S. Thorne. Disk-Accretion onto a Black Hole. Time-Averaged Structure of Accretion Disk. *ApJ*, 191:499–506, Jul 1974. doi: 10.1086/152990.
- E. N. Parker. The passage of energetic charged particles through interplanetary space. *Planet. Space Sci.*, 13(1):9–49, Jan 1965. doi: 10.1016/0032-0633(65)90131-5.
- B. M. Peterson. *An Introduction to Active Galactic Nuclei*. 1997.
- B. M. Peterson, L. Ferrarese, K. M. Gilbert, S. Kaspi, M. A. Malkan, D. Maoz, D. Merritt, H. Netzer, C. A. Onken, R. W. Pogge, M. Vestergaard, and A. Wandel. Central Masses and Broad-Line Region Sizes of Active Galactic Nuclei. II. A Homogeneous Analysis of a Large Reverberation-Mapping Database. *ApJ*, 613: 682–699, Oct. 2004. doi: 10.1086/423269.

- B. Punsly. Discrete and Continuous Ejection Models of the Radio Source Associated with GW170817. *arXiv e-prints*, Jan. 2019.
- E. Quataert, W. Dorland, and G. W. Hammett. The Magnetorotational Instability in a Collisionless Plasma. *ApJ*, 577(1):524–533, Sep 2002. doi: 10.1086/342174.
- M. J. Reid, J. E. McClintock, J. F. Steiner, D. Steeghs, R. A. Remillard, V. Dhawan, and R. Narayan. A Parallax Distance to the Microquasar GRS 1915+105 and a Revised Estimate of its Black Hole Mass. *ApJ*, 796(1):2, Nov. 2014. doi: 10.1088/0004-637X/796/1/2.
- R. C. Reis and J. M. Miller. On the Size and Location of the X-Ray Emitting Coronae around Black Holes. *ApJ*, 769(1):L7, May 2013. doi: 10.1088/2041-8205/769/1/L7.
- F. M. Rieger and K. Mannheim. Particle acceleration by rotating magnetospheres in active galactic nuclei. *A&A*, 353:473–478, Jan. 2000.
- M. M. Romanova, G. V. Ustyugova, A. V. Koldoba, V. M. Chechetkin, and R. V. E. Lovelace. Dynamics of Magnetic Loops in the Coronae of Accretion Disks. *ApJ*, 500:703–713, June 1998. doi: 10.1086/305760.
- A. Rózańska, J. Malzac, R. Belmont, B. Czerny, and P.-O. Petrucci. Warm and optically thick dissipative coronae above accretion disks. *A&A*, 580:A77, Aug. 2015. doi: 10.1051/0004-6361/201526288.
- N. Sachdeva, P. Subramanian, A. Vourlidas, and V. Bothmer. CME Dynamics Using STEREO and LASCO Observations: The Relative Importance of Lorentz Forces and Solar Wind Drag. *Sol. Phys.*, 292:118, Sept. 2017. doi: 10.1007/s11207-017-1137-9.
- S. Sahu, C. E. López Fortín, and S. Nagataki. Multi-TeV Flaring from High-energy Blazars: An Evidence of the Photohadronic Process. *ApJ*, 884(1):L17, Oct. 2019. doi: 10.3847/2041-8213/ab43c7.
- D. A. Schwartz. The High-energy emission of jetted AGN. *arXiv e-prints*, Jan. 2019.
- N. I. Shakura and R. A. Sunyaev. Black Holes in Binary Systems: Observational Appearances. In H. Bradt and R. Giacconi, editors, *X- and Gamma-Ray Astronomy*, volume 55 of *IAU Symposium*, page 155, Jan 1973.
- S. L. Shapiro, A. P. Lightman, and D. M. Eardley. A two-temperature accretion disk model for Cygnus X-1: structure and spectrum. *ApJ*, 204:187–199, Feb 1976. doi: 10.1086/154162.



- P. Sharma, G. W. Hammett, and E. Quataert. Transition from Collisionless to Collisional Magnetorotational Instability. *ApJ*, 596(2):1121–1130, Oct 2003. doi: 10.1086/378234.
- M. B. Shende, P. Subramanian, and N. Sachdeva. Episodic Jets from Black Hole Accretion Disks. *ApJ*, 877(2):130, June 2019. doi: 10.3847/1538-4357/ab1cb6.
- M. B. Shende, P. Chauhan, and P. Subramanian. X-ray dips in AGNs and microquasars - collapse time-scales of inner accretion disc. *MNRAS*, 501(3):3741–3749, Mar. 2021. doi: 10.1093/mnras/staa3838.
- A. P. Snodin, A. Shukurov, G. R. Sarson, P. J. Bushby, and L. F. S. Rodrigues. Global diffusion of cosmic rays in random magnetic fields. *MNRAS*, 457:3975–3987, Apr. 2016. doi: 10.1093/mnras/stw217.
- L. Spitzer. *Physics of Fully Ionized Gases*. 1962.
- D. Stepanovs, C. Fendt, and S. Sheikhnezami. Modeling MHD Accretion-Ejection: Episodic Ejections of Jets Triggered by a Mean-field Disk Dynamo. *ApJ*, 796:29, Nov. 2014. doi: 10.1088/0004-637X/796/1/29.
- P. Subramanian and P. A. Becker. Noise-Storm Continua: Power Estimates for Electron Acceleration. *Sol. Phys.*, 225(1):91–103, Nov. 2004. doi: 10.1007/s11207-004-3256-3.
- P. Subramanian, P. A. Becker, and M. Kafatos. Ion Viscosity Mediated by Tangled Magnetic Fields: an Application to Black Hole Accretion Disks. *ApJ*, 469:784, Oct. 1996. doi: 10.1086/177826.
- P. Subramanian, P. A. Becker, and D. Kazanas. Formation of Relativistic Outflows in Shearing Black Hole Accretion Coronae. *ApJ*, 523:203–222, Sept. 1999. doi: 10.1086/307703.
- P. Subramanian, P. A. Becker, and M. Kafatos. Using transport coefficients of cosmic rays in turbulent magnetic fields to determine hybrid viscosity in hot accretion disks around AGN. In *29th International Cosmic Ray Conference (ICRC29)*, Volume 4, volume 4 of *International Cosmic Ray Conference*, page 359, Jan 2005.
- P. Subramanian, A. Shukla, and P. A. Becker. TeV blazar variability: the firehose instability? *MNRAS*, 423(2):1707–1710, June 2012. doi: 10.1111/j.1365-2966.2012.20991.x.
- X. Sun and X.-N. Bai. Particle diffusion and acceleration in magnetorotational instability turbulence. *MNRAS*, 506(1):1128–1147, Sept. 2021. doi: 10.1093/mnras/stab1643.

- A. Tchekhovskoy, R. Narayan, and J. C. McKinney. Black Hole Spin and The Radio Loud/Quiet Dichotomy of Active Galactic Nuclei. *ApJ*, 711(1):50–63, Mar. 2010. doi: 10.1088/0004-637X/711/1/50.
- A. Tchekhovskoy, R. Narayan, and J. C. McKinney. Efficient generation of jets from magnetically arrested accretion on a rapidly spinning black hole. *MNRAS*, 418(1):L79–L83, Nov. 2011. doi: 10.1111/j.1745-3933.2011.01147.x.
- K. Toma and F. Takahara. Baryon Loading of Active Galactic Nucleus Jets Mediated by Neutrons. *ApJ*, 754(2):148, Aug. 2012. doi: 10.1088/0004-637X/754/2/148.
- T. Török and B. Kliem. The Kink Instability in Solar Eruptions. In R. W. Walsh, J. Ireland, D. Danesy, and B. Fleck, editors, *SOHO 15 Coronal Heating*, volume 575 of *ESA Special Publication*, page 56, Dec. 2004.
- T. Török and B. Kliem. Numerical simulations of fast and slow coronal mass ejections. *Astronomische Nachrichten*, 328:743, Oct. 2007. doi: 10.1002/asna.200710795.
- G. V. Ustyugova, A. V. Koldoba, M. M. Romanova, V. M. Chechetkin, and R. V. E. Lovelace. Magnetocentrifugally Driven Winds: Comparison of MHD Simulations with Theory. *ApJ*, 516:221–235, May 1999. doi: 10.1086/307093.
- D. A. Uzdensky and J. Goodman. Statistical Description of a Magnetized Corona above a Turbulent Accretion Disk. *ApJ*, 682:608–629, July 2008. doi: 10.1086/588812.
- S. V. Vadawale, A. R. Rao, A. Nandi, and S. K. Chakrabarti. Observational evidence for mass ejection during soft X-ray dips in GRS 1915+105. *A&A*, 370:L17–L21, Apr 2001. doi: 10.1051/0004-6361:20010318.
- S. V. Vadawale, A. R. Rao, S. Naik, J. S. Yadav, C. H. Ishwara-Chandra, A. Pramesh Rao, and G. G. Pooley. On the Origin of the Types of Radio Emission in GRS 1915+105. *ApJ*, 597(2):1023–1035, Nov 2003. doi: 10.1086/378672.
- M. K. Vyas and I. Chattopadhyay. Radiatively-driven general relativistic jets. *Journal of Astrophysics and Astronomy*, 39(1):12, Feb. 2018. doi: 10.1007/s12036-017-9494-1.
- M. K. Vyas, R. Kumar, S. Mandal, and I. Chattopadhyay. Radiatively driven relativistic jets with variable adiabatic index equation of state. *MNRAS*, 453(3): 2992–3014, Nov. 2015. doi: 10.1093/mnras/stv1811.
- D. G. Wentzel. The Propagation and Anisotropy of Cosmic Rays. II. Electrons. *ApJ*, 157:545, Aug. 1969. doi: 10.1086/150094.

- J. S. Yadav, A. R. Rao, P. C. Agrawal, B. Paul, S. Seetha, and K. Kasturirangan. Different Types of X-Ray Bursts from GRS 1915+105 and Their Origin. *ApJ*, 517(2):935–950, June 1999. doi: 10.1086/307225.
- F. Yuan, J. Lin, K. Wu, and L. C. Ho. A magnetohydrodynamical model for the formation of episodic jets. *MNRAS*, 395:2183–2188, June 2009. doi: 10.1111/j.1365-2966.2009.14673.x.
- A. A. Zdziarski, A. Segreto, and G. G. Pooley. The radio/X-ray correlation in Cyg X-3 and the nature of its hard spectral state. *MNRAS*, 456(1):775–789, Feb. 2016. doi: 10.1093/mnras/stv2647.
- M. Zhang and B. C. Low. The Hydromagnetic Nature of Solar Coronal Mass Ejections. *ARA&A*, 43:103–137, Sept. 2005. doi: 10.1146/annurev.astro.43.072103.150602.
- F. P. Zuccarello, G. Aulanier, and S. A. Gilchrist. Critical Decay Index at the Onset of Solar Eruptions. *ApJ*, 814:126, Dec. 2015. doi: 10.1088/0004-637X/814/2/126.